The Dissertation Committee for Jue Wang certifies that this is the approved version of the following dissertation:

High-Temperature Deformation of Al_2O_3/Y-TZP Particulate Composites and Particulate Laminates

Committee:

Desiderio Kovar, Supervisor

Eric M. Taleff

David L. Bourell

Arumugam Manthiram

Kenneth M. Liechti

High-Temperature Deformation of Al_2O_3/Y-TZP Particulate Composites and Particulate Laminates

by

Jue Wang, B. S. and M. S.

Dissertation

Presented to the Faculty of the Graduate School of
The University of Texas at Austin
in Partial Fulfillment
of the Requirements
for the Degree of

Doctor of Philosophy

The University of Texas at Austin
August, 2003

Dedication

This dissertation is dedicated to my parents, Yinkui Wang and Sendi Guo.

Acknowledgements

I am deeply indebted to my research supervisor, Dr. Desiderio Kovar, for his encouragement, advice, mentoring, and research support throughout my doctoral study. Special thanks go to Dr. Eric M. Taleff for his continuous assistance and gudiance. I also wish to thank Dr. David L. Bourell, Dr. Arumugam Manthiram, and Dr. Kenneth M. Liechti for serving on my committee and providing valuable advices.

I also would like to take this opportunity to thank the members of Dr. Kovar's group for the exchange of ideas and friendship. It has been a pleasure working with and learning from them.

Finally, it is impossible to have my research career without my parents and husband's love and support.

This work is funded by the Texas Advanced Research Program under project #003658-0426-1999 and NSF under grant DMR-9974476.

High-Temperature Deformation of Al_2O_3/Y-TZP Particulate Composites and Particulate Laminates

Publication No._____________

Jue Wang, Ph. D.
The University of Texas at Austin, 2003

Supervisor: Desiderio Kovar

Al_2O_3/Y-TZP particulate composites consisting of 20 - 80 vol% Al_2O_3 and Al_2O_3/Y-TZP particulate laminates with varying composition and ratios of layer thickness were fabricated, respectively, by tapecasting, lamination, and sintering. The resulting particulate composites and particulate laminates were tested in compression and tension at 1300 - 1450°C over strain rates from 1.00×10^{-5} to 3.16×10^{-4} s^{-1}. The high temperature behaviors of Al_2O_3/Y-TZP particulate composites and particulate laminates were characterized under conditions in which changes to the microstructure during testing were deliberately minimized. Results show that stress exponents are approximately two for both particulate composites and particulate laminates when tested in compression and tension, consistent with a grain-boundary sliding mechanism. Particulate laminates are stronger than particulate composites with the same overall composition due to the constraint imposed by the hard layer on the soft layer during the deformation. This hard layer dominates the resistance to deformation of the particulate laminates. A limited number of elongation-to-failure tests were also conducted at 1350°C at a true strain rate of 1.00×10^{-4} s^{-1}. Although grain growth and cavitaton occurred during the elongation-to-failure tests, superplasticity was observed for Al_2O_3/Y-TZP particulate composites and particulate laminates. In addition, models of composite creep behavior were compared to the experimental data. A constrained isostrain model was found to provide a good prediction for the high-temperature deformation of Al_2O_3/Y-TZP particulate composites and particulate laminates.

Table of Contents

List of Tables

List of Figures

Chapter 1

Introduction

Ceramics have high machining costs. One method for reducing the cost of fabricating ceramic components with a complex geometry is by superplastically forming them. In the last two decades, some ceramics and ceramic composites have been found to be superplastic, meaning they can be deformed in tension to very large strain. Among them, fine-grained 3Y-TZP (3 mol% Y_2O_3-stabilized tetragonal ZrO_2 polycrystal) exhibits an extraordinary elongation-to-failure at elevated temperatures. However, the ultra-fine Y-TZP powder adds considerable expense to the cost of a component. Furthermore, these fine microstructures are inherently unstable at high temperatures.

To solve these problems, particulate composites combining a superplastic phase with a less costly, non-superplastic phase have been introduced as promising candidates in structural applications. This type of microstructure is stable against grain growth during sintering and deformation. Al_2O_3/Y-TZP is a typical particulate composite. Low cost Al_2O_3 can be substituted for Y-TZP. Al_2O_3/Y-TZP particulate composites have improved fracture toughness and modulus. The high-temperature mechanical behaviors of Al_2O_3/Y-TZP particulate composites have been extensively investigated. However, experimentally determined deformation parameters, which have been used to evaluate deformation mechanisms of Al_2O_3/Y-TZP particulate composites, often varied with different research groups due to instability in the microstructure (*e.g.* grain growth and cavitation) during testing. These inconsistencies prevented a conclusive understanding of deformation mechanisms. Therefore, one of the aims of this dissertation is to study the mechanical behaviors of Al_2O_3/Y-TZP particulate composites at high temperatures under conditions that promote a stable microstructure so that reliable deformation parameters can be measured.

In addition, a novel layer architecture, *i.e.* particulate laminates, consisting of two alternating particulate composites layers with different composition, was studied. Particulate laminates have improved fracture toughness. Another objective of this dissertation is to study the high-temperature deformation behavior of Al_2O_3/Y-TZP particulate laminates. Since particulate composites are used within each lamina, a fine microstructure can be maintained during the high-temperature deformation of particulate laminates.

In our work, Al_2O_3/Y-TZP particulate composites with varying volume fractions of Al_2O_3 from 20 to 80 vol% and Al_2O_3/Y-TZP particulate laminates with varying layer thickness ratios and compositions were fabricated by tapecasting, lamination, and sintering. Compression strain-rate-change tests and tensile strain-rate-change tests were conducted to systematically evaluate the high-temperature mechanical behaviors of Al_2O_3/Y-TZP particulate composites and particulate laminates. Comparisons were made between the behaviors in compression and tension. In addition, elongation-to-failure tests were performed to study the superplastic behaviors of Al_2O_3/Y-TZP particulate composites and particulate laminates. The microstructures of the specimens were characterized before and after testing. Lastly, the existing models were evaluated and modified to predict the high-temperature behaviors of Al_2O_3/Y-TZP particulate composites and particulate laminates.

The dissertation is organized as follows. It begins with a review of the prior state of knowledge. Next, Chapter 3 introduces the experimental procedure in detail. Then, Chapter 4 and 5 discuss the high-temperature deformation of Al_2O_3/Y-TZP particulate composites and particulate laminates tested in compression, respectively. Chapter 6 investigates the high-temperature behaviors of selected Al_2O_3/Y-TZP particulate composites and laminates tested in tension. This dissertation closes with a brief conclusion as Chapter 7.

Chapter 2

Prior State of Knowledge

2.1 APPLICATION OF SUPERPLASTICITY ON CERAMICS

Ceramics offer a number of potential benefits over metallic alloys for structural applications, including greater resistance to wear and corrosion, lower density, and higher stiffness [1]. Structural ceramics are being used more frequently for the productions of various components in engineering, such as cutting tools, turbine blades, rotors, nozzles, and rolling element bearings [1]. However, there remain problems with ceramics, such as low fracture toughness that an impediment to the commercialization of structural ceramics in advanced applications. Another issue is the difficulty of fabricating ceramic components with complex shapes at a reasonable cost. Because of high hardness and low ductility, machining costs can represent up to 90% of the total manufacturing cost for a ceramic component [2]. Since the 1950s, extensive efforts have been made to fabricate ceramics at elevated temperatures using conventional metallurgical processes such as extrusion, rolling, and forging [3]. The temperature required for hot forging Al_2O_3 was found to be about 1900^oC, which is extremely high from a practical standpoint [3].

In the 1960s, the concept of superplasticity was proposed. Superplasticity is the ability of a polycrystalline material to exhibit very high tensile elongation prior to failure at elevated temperature [4]. The enormous ductility of superplasticity makes it possible to fabricate large and complex components in one piece with little or no machining. Superplasticity enhances the workability of difficult-to-work materials, such as metal-matrix composites, intermetallic compounds, and ceramics. Superplastic forming has been one of the major manufacturing technologies for cost saving and weight reduction in aerospace industries [5].

In 1986, Wakai *et al.* first reported a large elongation-to-failure of over 120% in 3 mol% Y_2O_3-stabilized tetragonal ZrO_2 polycrystal (3Y-TZP) [6]. Since then, superplasticity has been reported in a wide range of fine-grained ceramics [7-16]. These include Y_2O_3-stabilized tetragonal ZrO_2 polycrystal (Y-TZP) [6,7,13,17], Y_2O_3-doped Al_2O_3 [18], hydroxyapatite ($Ca_{10}(PO_4)_6(OH)_2$) [14], *b*-spodumene ($Li_2O \cdot Al_2O_3 \cdot 4SiO_2$) glass ceramics [19], Al_2O_3-reinforced Y-TZP (Al_2O_3/Y-TZP) [9,11,20-23], and SiC-reinforced Si_3N_4 (SiC/Si_3N_4) [15,24]. A maximum tensile elongation of 1038% has been recorded in a 2.5 mol% Y_2O_3-stabilized tetragonal zirconia containing 5 wt% SiO_2 at 1400^oC [25].

The development of superplasticity greatly enhances the formability of ceramics. For example, Kellett and Lange successfully hot-forged a fine-grained Al_2O_3/20 vol% ZrO_2 to 80% reduction in thickness at 1500^oC [26,27]. Carry and

Mocellin conducted bar bending and inverse extrusion of fine-grained Al_2O_3 at 1300 - 1600°C [28]. Wu and Chen demonstrated that a Y-TZP containing 0.3 mol% CuO could be biaxially stretched into hemispheric dome shapes at temperatures as low as 1150°C [29]. These superplastically formed parts have a smooth surface finish with excellent dimensional accuracy required for aerospace applications. In addition, the reduction in forming temperature represents a major technological breakthrough for ceramic forming, because it reduces the operation requirements for furnaces and tools [30]. All these potential benefits of superplastically forming ceramics provide the impetus to an extensive investigation of superplasticity in ceramics.

2.2 SUPERPLASTIC BEHAVIOR OF FINE-GRAINED CERAMICS

There are two-well established types of superplastic behavior in polycrystalline solids: internal stress superplasticity (transformation superplasticity) and fine-grained superplasticity (structural superplasticity) [31]. The former is obtained by temperature cycling a material through a phase change, whereas the latter refers to the attainment of extensive deformation at a constant temperature without a related phase change [32]. In this dissertation, we will focus on fine-grained superplasticity.

2.2.1 Microstructure Characteristics

Superplastic ceramics demonstrate remarkably high strains to failure at strain rate of ~ 10^{-4} s^{-1} at high temperature ($T \geq 0.5T_m$, where T_m is the absolute melting temperature). The major requirements for the fine-grained superplastic ceramics include: (i) a uniform, equiaxed, ultra-fine-grained microstructure (grain size $\leq 1mm$), which must be resistant to grain growth during deformation; (ii) a low stress exponent ($n \leq 3$); (iii) a strong cohesive strength of grain boundaries.

Studies showed that fine-grained microstructures are usually unstable at high temperature; as a result, grain growth, particularly dynamic grain growth, has been observed during deformation [33-37]. For example, considerable grain growth with a significant degree of strain hardening has been reported in a superplastic 3Y-TZP by Nieh *et al.* [35,37]. Schissler *et al.* suggested that the deformation-enhanced concurrent grain growth is a function of the strain, strain rate and temperature [38]. In contrast, Duclos *et al.* did not observe any grain growth in 3Y-TZP [39-41]. Chokshi *et al.* attributed this discrepancy to the difference in materials [33]. The material tested by Duclos *et al.* contained a substantial amount of a glassy intergranular phase, whereas the material tested by Nieh *et al.* did not contain any glassy phase. Raj predicted that deformation-enhanced concurrent grain growth will not occur in materials with glassy grain boundaries [42]. Observations suggested that in most ceramics, grains essentially retain their equiaxed shapes during the superplastic deformation [6,41,43-45] and there is a lack of intragranular dislocation activity [46].

In addition, the presence of a liquid phase has been reported in numerous superplastic ceramics. For example, Wang and Raj demonstrated a tensile elongation up to ~ 400% in a b-spodumene glass ceramic containing 64.6 wt% SiO_2 [19,47]. Hermansson *et al.* examined 3Y-TZP containing 0.092 wt% Al_2O_3 and 0.011 wt % SiO_2 and reported the presence of an intergranular glassy phase, having a thickness of 1 - 2 *nm* [48]. The sintering aids and/or impurities in the starting materials, in combination with various processing steps, are often responsible for the formation of low-melting point, grain-boundary amorphous phases in ceramics [44]. However, Nieh *et al.* showed the absence of glassy phase in superplastic 3Y-TZP containing 0.005 wt% Al_2O_3 and 0.002 wt% SiO_2 and suggested the impurities do not necessarily lead to the formation of an intergranular glass phase at the impurity levels typically associated with superplastic 3Y-TZP [34,44]. Although the presence of a liquid phase is not necessary for superplastic ceramic, it can significantly affect the high-temperature deformation. For example, Hwang and Chen demonstrated that the temperature for superplasticity in 2Y-TZP can be reduced by doping the material with CuO to create a grain-boundary glassy phase [49]. Gust *et al.* showed the glass-containing 3Y-TZP deforms about 10 times faster than the pure 3Y-TZP [50]. Wakai *et al.*

reported that a fine-grained SiC/Si_3N_4 composite exhibits a superplastic behavior with a substantial amount of intergranular phase [15].

2.2.2 Cavitation and Ductility

Limited quantitative studies have been performed on the cavitation behavior of superplastic ceramics during deformation. Despite the fact that superplastic materials exhibit large tensile elongations, the materials after large tensile strains are susceptible to extensive internal cavitation and cracking [33,38,51-55]. The extent of cavitation increases with increasing strain rate at a constant temperature [52,53]. The tensile ductility of superplastic ceramics is limited by cavity interlinkage in a direction perpendicular to the tensile axis during superplastic deformation [38,51]. The cavities develop as a direct consequence of the applied stress so that higher stress levels lead to higher levels of internal cavitation [55]. The tensile ductility thus decreases with increasing flow stress. A similar conclusion has also been proposed by Chen and Xue [56]. They demonstrated that the tensile ductility of superplastic ceramics is limited by grain-boundary decohesion, which is in turn determined by flow stress. Lowering flow stress and increasing the grain-boundary strength thus provide an effective method for improving superplastic formability. In addition, grain size strongly influences the superplastic properties of fine-grained ceramics. Nieh and Wadsworth found that the flow stress of Y-TZP at a constant true strain rate and at a given strain is proportional to the square of the grain size [57]; the flow stress of Al_2O_3/Y-TZP is proportional to the grain size raised to 0.75 power [58]. Because flow stress increases with grain size, a critical grain size exists above which the cohesive strength of grain boundary is exceeded, resulting in cavitation and an eventual crack. Thus, the tensile ductility of ceramics increases with decreasing grain size.

Evidence for superplasticity in ceramic materials has been obtained indirectly from compression tests as well as directly from tension tests. Compression tests are very useful in providing information on the deformation mechanism of flow behavior [12,59-62]. It is important to point out that superplasticity refers to high ductility in tension; therefore, enhanced plasticity data from compression tests cannot necessarily be considered as convincing evidence of superplasticity. Ceramics that are successfully deformable in compression may fail prematurely in tension from grain-boundary separation or other related tensile fracture effects. As mentioned above, tensile ductility at elevated temperature is limited primarily by grain-boundary cavitation, which is initiated by tensile stresses but which is usually suppressed by compressive stresses [31]. Results on a superplastic b-spodumene glass ceramic by Wang and Raj [19] and on zirconia by Wakai *et al*. [63] indicated that a higher stress is needed in compression than in tension, for a given strain rate. The explanation for these observations is not clear yet, although Wang and Raj claimed that friction between test samples and the platen in compression may cause the above difference [19]. There is evidence suggesting the mechanisms may be different in compression and tension [64]. Conversely, Owen and Chokshi reported that there is no significant difference in the stress necessary to deform 20 wt% Al_2O_3/Y-TZP composite at a given strain rate in tension as compared to compression [65]. Nauer and Carry also reported Y-TZP materials typically exhibit similar behavior in both tension and compression [66].

2.2.3 Creep Mechanisms

At high temperature, permanent deformation can occur over a period of time at a stress level well below the material's yield strength. This time-dependent permanent deformation is called creep [67]. Typically, creep occurs at a temperature of $T \geq 0.5T_m$, where T_m is the absolute melting temperature [67]. Generally, the steady-state creep rate of polycrystalline materials at elevated temperature may be expressed using the phenomenological equation [68]:

$$\dot{e} = A\left(\frac{s}{E}\right)^n\left(\frac{b}{d}\right)^p \exp\left(-\frac{Q_c}{RT}\right) \qquad (2.1)$$

where s is the stress, E is the dynamic, unrelaxed Young's modulus, T is the absolute temperature, b is the magnitude of Burgers vector, d is the grain size, n is the stress exponent, p is the inverse grain size exponent, Q_c is the activation energy for creep, R is the gas constant, and A is a material constant. Depending on temperature and applied stress, diffusional-flow, dislocation slip or grain-boundary sliding mechanism may dominate creep deformation. Each creep mechanism has specific values of n, p, and Q. Diffusional creep typically produces a stress exponent of $n = 1$ and the deformation is a result of the transport of matter by diffusion. Diffusional creep can be further divided into Nabarro-Herring creep ($p = 2$) where mass transport occurs by diffusion through the lattice and Coble creep ($p = 3$) where mass transport occurs by diffusion along grain boundaries [67]. Basically, the models for diffusional creep assume that the entire grain boundary surface is a perfect sink or source for matter [69]. If this assumption is not satisfied, the diffusion creep is controlled by the interface reaction and the dislocation-like defects which act as the sink and source for matter lead to a significant modification to the model for diffusion creep [69]. For example, the stress exponent for interface-controlled diffusion creep in materials without glassy phase is larger than 1. Dislocation creep is characterized by a stress exponent of $n =$ 3 - 8 and deformation is controlled by dislocation glide or climb. For a stress exponent of 3, solute-drag creep may be controlling creep rate, as a result of the interaction between gliding dislocations and a solute atmosphere. The creep rates of dislocation slip creep are distinctive in that they are independent of grain size, *i.e.* $p = 0$. Another creep mechanism involves grain boundary sliding, which must be accommodated by other deformation modes, *e.g.* dislocation slip of diffusional flow in order to prevent the formation of internal voids or cracks during deformation. Grain boundary sliding is usually characterized by $n = 2$ [67].

Based on the phenomenological equation (Equation 2.1), the mechanical behavior of superplastic materials can be represented in the form of $\dot{e} = Bs^{n}$, where B is a constant, which incorporates the dependence of flow on temperature and grain size. Typically, superplastic metals exhibit three regimes in a logarithmic plot of s versus $\dot{e}$, as depicted schematically in Figure 2.1 [70]. Region I and III occur at low and high strain rate, respectively, and have a high value of *n*; Region II occurs at intermediate strain rates where the values of n is low [70]. Grain boundary sliding is dominant in the superplastic Region II, but decreases in importance in Region I at low strain rate. Region III corresponds to dislocation creep. For ceramics, the transition from the superplastic regime (Region II) to the dislocation regime (Region III) is rarely seen. This is primarily due to the fact that most ceramics do not have sufficient strength to resist fracture before the high flow stresses required for the transition can be reached. However, in the recent studies, an intragranular-dislocation creep process has also been observed at high stress [71,72].

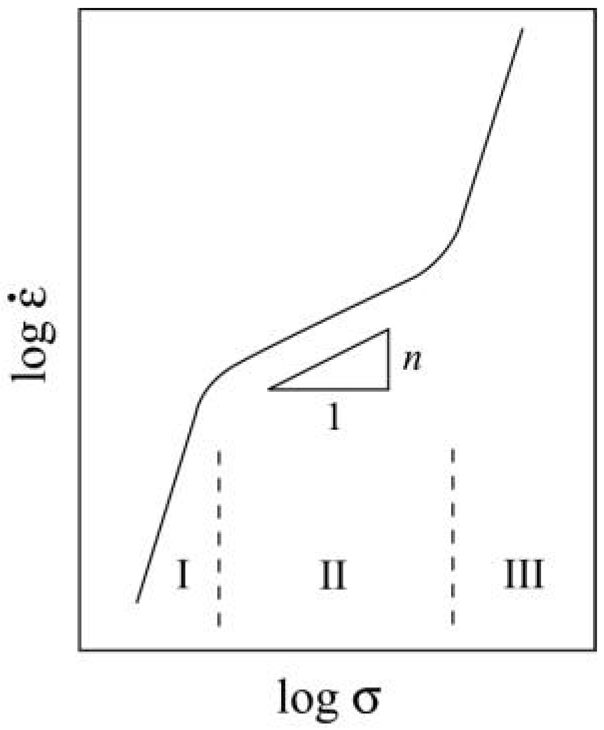

Figure 2.1 A logarithmic plot of strain rate versus stress typically observed for superplastic metals [70].

Grain-boundary sliding plays an important role in superplastic deformation. For metals, it has been concluded that grain-boundary sliding accounts for essentially all the deformation of metals under optimum superplastic conditions. For ceramics, the microstructural observations of dislocation-free grains and equiaxed grain shapes, also suggested the major role of grain-boundary sliding in deformation mechanism. Extensive grain-boundary sliding, accompanied by considerable grain rotation, has been observed on superplastically deformed ceramics. Data reported for polycrystalline Al_2O_3 and Y-TZP indicated that the strain contributed by grain boundary sliding is as great as 70% and 80%, respectively [73,74]. The contribution of grain boundary sliding has also been estimated about 50% to the total strain during the superplastic deformation of the fine-grained Al_2O_3/20 wt% ZrO_2 [75]. Grain-boundary sliding accommodated by dislocation slip or diffusional flow has been considered in explaining superplasticity of fine-grained superplastic materials [46,76]. In 1969, Ball and Hutchison first proposed a model to describe a grain-boundary sliding process accommodated by slip [77]. Since then, various quantitative models have been developed to describe superplastic flow accommodated by dislocation slip and all of them are in agreement with $n = 2$ [30]. A different model based on grain-boundary sliding with diffusional accommodation has also been developed by Ashby and Verall [78]. The Ashby-Verall model predicts that diffusion-controlled and interface-controlled deformation lead to $n = 1$ and $n = 2$, respectively. Since a fine grain size favors interface-reaction control, most fine-grained superplastic materials are observed to exhibit $\dot{\varepsilon} \propto \sigma^{2}/d$ [78]. As proposed originally by Ashby and Verrall, grain shape is preserved during deformation by a "grain-switching" mechanism [78], which is schematically shown in Figure 2.2. A group of four grains moves from the initial state, through the intermediate state to the final state. The grains accommodate strains and translate past each other by sliding at their boundaries [78].

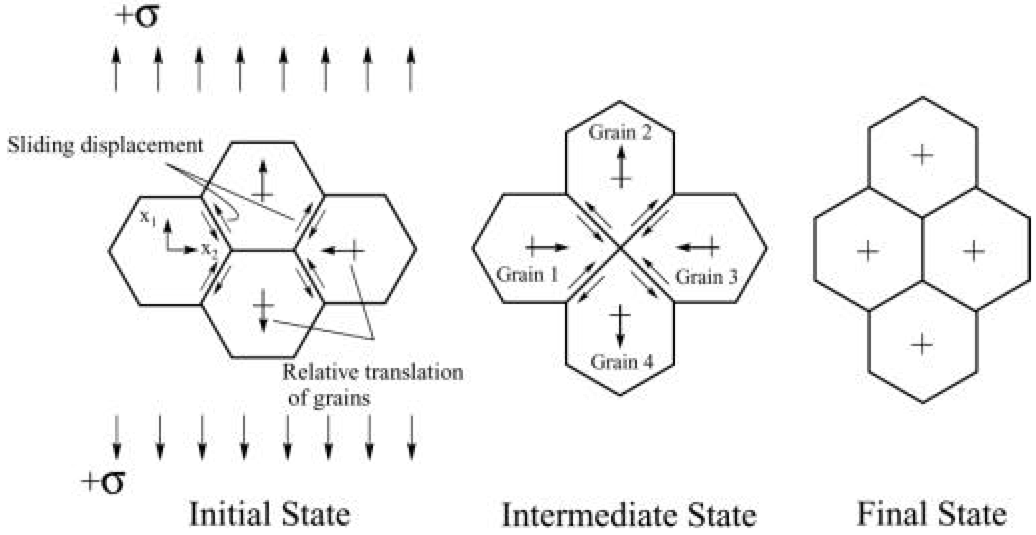

Figure 2.2 The grain-switching mechanism [78].

2.2.4 Superplasticity in 3Y-TZP

Although superplasticity has been reported in numerous monolithic ceramics and ceramic composites, most attention has been devoted to the Y-TZP system. One interesting microstructural feature of Y-TZP is the persistence of Y^{3+} segregation to grain boundaries. Direct evidence for Y^{3+} segregation at grain boundaries of Y-TZP has been provided by Auger Electron Spectroscopy, X-ray Photoelectron

Spectroscopy, and Energy Dispersive Spectrometry of intergranularly fractured specimens [44,79]. The primary attributes of Y-TZP as a fine-grained superplastic ceramic are closely related to the strong segregation of solute cations to the grain boundary, which lowers the grain boundary mobility and the grain-boundary energy [56].

3 mol% Y_2O_3-stabilized zirconia, 3Y-TZP, is the first true polycrystalline ceramic without glassy phase demonstrated to be superplastic and is considered as a model system. Chemical compositions of commercial 3Y-TZP without glassy phase are typically (by weight) 5.2% Y_2O_3, 0.005% Al_2O_3, 0.002% SiO_2, 0.002% Fe_2O_3, 0.003% Na_2O, and balance ZrO_2 [31]. The microstructure of the material exhibits equiaxed grains. Nieh *et al.* demonstrated that 3Y-TZP consists of the tetragonal phase with only a small amount of the monoclinic phase [44]. Following the initial report by Wakai *et al.* [6], there have been extensive studies on the superplastic properties of the 3Y-TZP. Wakai *et al.* showed that the 3Y-TZP with a fine grain size of 0.3 *mm* is superplastic at 1450°C with 170% elongation [6]. Nieh *et al.* further reported a maximum tensile elongation value of 800% for 3Y-TZP at a temperature of 1550°C and a strain rate of 8.3×10^{-5} s^{-1} [13].

2.2.4.1 The rate-controlling parameters (n, p, and Q)

There is a wide range of values reported for *n*, *p*, and *Q* during the deformation of 3Y-TZP. The values of *n* range from about 1 to 3, with typical values around either 2 or 3. The activation energies tend to lie in the range of 350 - 700 kJ/mol, where most of *Q* values cluster around 550 ± 50 kJ/mol. The values of the inverse grain size exponent reported from very few experimental results range from 1.5 - 4 [32,46]. The interpretation of experimental data usually relies on a precise determination of *n*, *p* and *Q*. Among these three rate-controlling parameters, the interpretation of the *Q*-value is probably the most difficult. For example, considering Y-TZP, diffusion of Zr^{4+} cation is the slower diffusing species and should be the controlling one. Unfortunately, no data for cation diffusion in tetragonal zirconia are currently available. Only the activation energy for the diffusion of Zr^{4+} in cubic zirconia has been determined. There poses a serious problem in selecting precise diffusion data and, subsequently, in identifying the deformation mechanism. Furthermore, ceramics usually contain a significant number of defects and impurities, and diffusion processes in ceramics are therefore even more complicated. Thus, it is probably more useful to assess superplastic deformation mechanisms by comparison of the values of *n* and *p* [30].

Markedly different values have been reported for stress exponent, *n*, even under nominally identical testing conditions. In the early studies, Wakai *et al.*

reported a stress exponent of ~ 2 [6]. In contrast, Nieh *et al.* obtained a stress exponent of ~ 3 on nominally identical materials [7]. Nieh *et al.* attributed the difference in stress exponent to variations in the testing atmosphere, grain growth and testing procedure [13,34]. However, a subsequent study demonstrated that identical stress exponent and creep rates are obtained in air and in an inert atmosphere [80]. Also, Ma and Langdon eliminated the testing procedure as possible explanation for the reported differences in stress exponents [53]. In terms of concurrent grain growth, Nieh *et al.* suggested that the value of $n \sim 3$ is influenced by the occurrence of concurrent grain growth during testing and the true stress exponent should be evaluated under conditions of constant microstructure [34]. However, in the strain rate change experiments conducted by Ma and Langdon, a value of $n \sim 3$ was still obtained although there was no instantaneous change in the grain size [53]. In addition, initial grain size can also affect the n value [66,81]. The value of n decreases and tends toward 1 with an increase of initial grain size [81].

Carry first pointed out that the stress exponent, n, depends on the Al_2O_3 impurity content in Y-TZP [45]. Specifically, the values of n were found to be 2 and 3 for materials, which contain high (0.0065%) and low (0.005%) Al_2O_3 contents, respectively. Carry predicted the high Al_2O_3-containing material causes the formation of glassy phases at grain boundary [45]. Langdon showed that the experimental value of n depends essentially inversely on the area fraction of grain boundaries having a glassy phase: for “low” purity material the area fraction of a glassy phase is relatively large and n is low, but for “high” purity material the area fraction is small and n is high [32]. Attempts have also been made to explain this influence of initial grain size by invoking a corresponding increase in the area fraction of a glassy phase with increasing initial grain size. The value of n thus decreases as the initial grain size increases [32]. However, Nieh *et al.* reported no glassy phase was observed in 3Y-TZP [44].

Further, a detailed study by Owen *et al.* on the compression creep behavior of 3Y-TZP revealed a transition from $n \sim 2$ and $p \sim 3$ at high stresses to $n \sim 3$ and $p \sim 1$ at low stresses [82]. They demonstrated that an increase in impurity content should cause a decrease in the apparent transition stress between the $n \sim 2$ and $n \sim 3$ regions. For a material with a given level of residual trace impurities, it is anticipated that there will be an increase in the level of impurities at the grain boundary with a decrease in the total grain boundary area (caused by an increase in the grain size). Thus, the stress at which the transition in stress exponent occurs decreases with an increase in the grain size [82]. The above explanation can rationalize the difference in the stress exponent reported in the earlier studies and also rationalize the observations of a decrease in stress exponent with an increase in grain size and the amount of impurity when experiments are conducted over a limited range of stresses. Jiménez-Melendo *et al.* further showed that stress exponent changes continuously from 2 to higher values (≥ 3), and then towards 1 at lower stress, when the stress decreases. The transition stress from $n \sim 2$ to $n \geq 3$ decreases with increasing grain size and temperature [83]. Recently, Morita *et al.* reported that n takes a value of 2.7 at 15 - 80 *MPa* and 1.6 at stress lower than 10 *MPa*, with a transition of $n > 5$ [72].

2.2.4.2 Possible deformation mechanisms

Grain-boundary sliding has been proposed as one of the most probable mechanisms of superplastic behavior in 3Y-TZP [6,13,79], however, there is currently no consensus concerning the accommodation mechanisms.

Owen and Chokshi suggested that the rate-controlling deformation mechanism is the operation of two sequential processes: grain boundary sliding with $n \sim 2$ in the high stress region and interface-reaction controlled grain boundary sliding with $n \sim 3$ in the low stress region [82,84,85]. This transition from $n \sim 3$ to $n \sim 2$ occurred at lower stress with an increase in impurity content. The sensitivity to impurity content in the low stress region is associated with the effect of the impurities on the segregation of yttrium ions to grain boundaries. An increase in impurity content leads to an increase in the amount of segregation, thereby increasing the interface reaction rate [82].

Alternatively, Jiménez-Melendo and Domínguez-Rodriguze attributed the deformation of 3Y-TZP to grain boundary sliding ($n \sim 2$) controlled by lattice diffusion with a threshold stress ($n \geq 3$) which is inversely proportional to grain size and temperature [86-91]. The presence of yttrium segregated at grain boundaries may provide a plausible explanation for the existence of a threshold stress [87]. Jiménez-Melendo demonstrated that high stress region can be characterized by $n \sim 2$, $p \sim 2$, whereas values for n, p, and Q are not constant in the lower stress region. n and Q increase and p decreases when the stress is decreased [91]. However, analyses of some experimental data yielded a negative threshold stress, raising doubts about the general validity of this approach [82].

Recently, Berbon and Langdon [92,93] suggested that the interface-controlled diffusion creep is the rate controlling process for superplasticity in 3Y-TZP. The interface-controlled diffusion model developed by Arzt *et al.* [69] is essentially the same process envisaged in Coble diffusion creep controlled by the movement of the Zr^{4+} ions along the grain boundaries. However, as a consequence of the small grain size, diffusional creep is interface-controlled, where the grain boundary surface will not act as perfect sink or source for matter. The model predicts an increase from an asymptotic value of $n \sim 1$ and $p \sim 3$ at high stresses to $n \sim 3$ and $p \sim 1$ at low stresses, with $n \sim 2$ only as a transition from $n \sim 1$ to $n \sim 3$. The mechanism involving rapid grain boundary migration and grain growth may mask any grain elongation and result in an equiaxed grain configuration even during diffusionional creep [43,92,94]. Although this interface-controlled model is consistent with experimental results

[71,92,93,95,96], additional models need to be considered to account for the observations of extended regions with $n \sim 2$ as well as the effect of impurity content on flow behavior of 3Y-TZP [71]. Moreover, the lack of appropriate diffusion data severely restricts the validity of conclusions based on a good match between experimental data and theoretical predictions.

In addition, 3Y-TZP with a substantial amount of glassy phase has different deformation mechanisms. As demonstrated by Wang and Raj, the deformation with liquid phase is limited by the diffusion of atoms through the liquid phase [19]. Wakai *et al.* suggested that solution-precipitation creep dominates the high-temperature deformation of the Y-TZP with thin, amorphous grain boundary films [97,98]. As the stress is reduced, interface-reaction creep becomes rate-controlling [99].

2.2.5 Superplasticity in Fine-Grained Al_2O_3

Alumina is probably one of the most widely used structural ceramics, but only limited studies on superplasticity in fine grained Al_2O_3 have been performed. Superplasticity is difficult to obtain in pure alumina, as a result of rapid anisotropic grain growth during high-temperature deformation [100]. A fundamental problem associated with pure alumina is its relatively high grain-boundary energy which causes a relatively low cohesive strength for grain boundaries [56]. Several studies on superplasicity in doped, fine-grained alumina have been conducted. Gruffel *et al.* demonstrated a Y_2O_3-doped Al_2O_3 with a grain size of about 0.66 *mm* exhibits a rupture elongation of 65% at 1450^oC under an applied stress of 20 *MPa* [18]. Xue *et al.* showed that the addition of ZrO_2 can greatly stabilize the grain size of Al_2O_3 during superplastic deformation [100].

Attempts have also been made to introduce a low-melting liquid phase to alumina to lower the sintering and superplastically forming temperatures [56]. However, low ductility was obtained due to a severely degraded grain boundary cohesive strength. As the liquid phase lowers the flow stress of alumina, it also facilitates abnormal grain growth and probably lowers the interfacial strength [56].

2.2.6 Superplasticity in Ceramic Composites

In comparison to monolithic ceramics, composites consisting of two-well mixed phases exhibit higher resistance to grain coarsening during the deformation [101-103]. There are many successful examples of superplastic ceramic composites, including Al_2O_3/ZrO_2 [9,11,20-23], $Al_6Si_2O_{13}/ZrO_2$ [60], SiC/Si_3N_4 [15,24], and ZnS/Diamond [59]. Among them, Al_2O_3/Y-TZP composites are considered as a model material system. There is no intermediate phase existing between alumina and zirconia. Al_2O_3/Y-TZP composites have excellent mechanical behavior at high temperature. Wakai and Kato showed that 20 wt% Al_2O_3/Y-TZP has a maximum tensile elongation of over 200% at 1450^{o}C [8]. Nieh and Wadsworth further recorded a maximum elongation of up to 625%, obtained from testing at 1650^{o}C and a strain rate of 4.0×10^{-4} s^{-1} [21]. Previous studies showed that concurrent grain growth occurs during the superplastic deformation of Al_2O_3/Y-TZP composites [8,11].

2.3 PRESENT INVESTIGATIONS

As mentioned above, the high-temperature deformation behaviors of Al_2O_3/Y-TZP particulate composites have been studied extensively due to their superior mechanical properties at high temperature. Despite that, the rate controlling deformation mechanism has not yet been unambiguously identified. The difficult in identifying the rate controlling mechanism arises from the discrepancy in data (n, p, and Q), which is a consequence of the inability of microstructure (grain growth, cavitaion, *etc.*) during testing at high temperatures. In the present investigation, the high-temperature behaviors of Al_2O_3/Y-TZP particulate composites are systematically studied under stable microstructure. In addition, layers of Al_2O_3/Y-TZP particulate composites with different composition are laminated to form particulate laminates where fine-grained microstructures are maintained within each layer during deformation. The influence of phase assemblage, specimen orientation, stress state, and layer thickness ratios on the high-temperature behaviors of Al_2O_3/Y-TZP particulate laminates are investigated. Studies of particulate laminates provide a significant path for controlling the mechanical properties by adjusting microstructure design. It could be very helpful in developing new structural materials.

Chapter 3

Experimental Procedures

3.1 INTRODUCTION

All of the specimens used in this study were prepared in house. The methods used to fabricate, characterize, and test the Al_2O_3/Y-TZP particulate composites and particulate laminates are detailed in the sections that follow.

3.2 PROCESSING

The processing steps include: slurry preparation, tapecasting, lamination, binder burn-out, and sintering.

3.2.1 Slurry Preparation

High-purity, 3 mol% yttria-stabilized tetragonal zirconia powder (3Y-TZP, Tosoh, Tokyo, Japan) and high-purity alumina powder (AKP-50, 99.99% purity, Sumitomo Chemical Co. Ltd., Tokyo, Japan) were used as raw materials. The ceramic powders were mixed with three solvents in a 1000 *ml* polyethelene container. These three solvents were methyl ethyl ketone (99.5+%, Mallinckrodt

Baker. Inc., Paris, Kentucky), methyl isobutyl ketone (99.8%, Sigma Chemical Co., St. Louis, MO) and cyclohexanone (99.0%, EM Industries, Gibbstown, NJ). This mixture of solvents was chosen to increase the solubility of the polymer binder in the liquid and to modify the evaporation rate so that a nearly constant evaporation rate could be achieved. A consistent evaporation rate reduced internal stresses caused by shrinkage by allowing the stresses to relax without cracking of the tapes. Before adding the ceramic powders, a dispersant (PS3, ICI Americas Inc., Wilmington, DE) was added to enhance the powder dispersion characteristics through steric hindrance. After ball milling the slurries for 24 hours, a plasticizer (butyl benzyl phthalate, Solutia Inc., St. Louis, MO) and a polymer binder (Butvar B76, Monsanto Company, St. Louis, MO) were added to increase flexibility and strength of the tapes. The mixture was then ball-milled again for 24 hours to homogenize the slurry. Slurries were prepared with solids contents of 20, 40, 50, 60, and 80 vol% Al_2O_3, with the balance Y-TZP. The chemical compositions of the slurries are listed in Table 3.1.

Table 3.1 The chemical compositions of the slurries used in this study.

Slurry of 20 vol% Al_2O_3-80 vol% Y-TZP

Ingredient	Density (*g/cm*^{3})	Volume (*cm*^{3})	Mass (*g*)	Volume percent (%)	Mass percent (%)
MEK	0.7504	99.54	74.69	29.8	13.4
MIBK	0.7476	99.55	74.42	29.8	13.3
Cyclohexonane	0.9089	40.12	36.47	12.1	6.5
Hypermer PS3	1.1278	6.65	7.50	2.0	0.7
Ceramic:					
Zirconia	6.05	48	290.40	14.4	52.0
Alumina	3.97	12	47.64	3.6	8.5
Butyl Benzyl Phthalate	1.122	16.63	18.66	5.0	3.3
B76 Butvar	1.1	11.09	12.20	3.3	2.2
Total		333.58	558.53	100.0	100.0

Slurry of 40 vol% Al_2O_3-60 vol% Y-TZP

Ingredient	Density (*g/cm*^{3})	Volume (*cm*^{3})	Mass (*g*)	Volume percent (%)	Mass percent (%)
MEK	0.7504	99.54	74.69	30.0	14.0
MIBK	0.7476	99.55	74.42	30.0	14.0
Cyclohexonane	0.9089	40.12	36.47	12.1	6.8
Hypermer PS3	1.1278	4.512	5.09	1.4	0.7
Ceramic:					
Zirconia	6.05	36	217.80	10.9	40.8
Alumina	3.97	24	95.28	7.2	17.9
Butyl Benzyl Phthalate	1.122	16.63	18.66	5.0	3.5
B76 Butvar	1.1	11.09	12.20	3.3	2.3
Total		331.44	533.27	100.0	100.0

Slurry of 50 vol% Al_2O_3-50 vol% Y-TZP

Ingredient	Density (*g/cm^3*)	Volume (*cm^3*)	Mass (*g*)	Volume percent (%)	Mass percent (%)
MEK	0.7504	99.54	74.69	30.1	14.3
MIBK	0.7476	99.55	74.42	30.1	14.3
Cyclohexonane	0.9089	40.12	36.47	12.1	7.0
Hypermer PS3	1.1278	4.17	4.70	1.3	0.9
Ceramic:					
Zirconia	6.05	30	181.50	9.1	34.8
Alumina	3.97	30	119.10	9.1	22.8
Butyl Benzyl Phthalate	1.122	16.63	18.66	5.0	3.6
B76 Butvar	1.1	11.09	12.20	3.3	2.3
Total		331.10	521.74	100.0	100.0

Slurry of 60 vol% Al_2O_3-40 vol% Y-TZP

Ingredient	Density (*g/cm^3*)	Volume (*cm^3*)	Mass (*g*)	Volume percent (%)	Mass percent (%)
MEK	0.7504	99.54	74.69	30.1	14.7
MIBK	0.7476	99.55	74.42	30.1	14.6
Cyclohexonane	0.9089	40.12	36.47	12.1	7.2
Hypermer PS3	1.1278	3.89	4.38	1.2	0.7
Ceramic:					
Zirconia	6.05	24	145.20	7.3	28.6
Alumina	3.97	36	142.92	10.9	28.1
Butyl Benzyl Phthalete	1.122	16.63	18.66	5.0	3.7
B76 Butvar	1.1	11.09	12.20	3.4	2.4
Total		330.81	508.31	100.0	100.0

Slurry of 80 vol% Al_2O_3-20 vol% Y-TZP					
Ingredient	Density (g/cm^3)	Volume (cm^3)	Mass (g)	Volume percent (%)	Mass percent (%)
MEK	0.7504	99.54	74.69	30.1	15.5
MIBK	0.7476	99.55	74.42	30.1	15.4
Cyclohexonane	0.9089	40.12	36.47	12.1	7.5
Hypermer PS3	1.1278	3.32	3.75	1.0	0.8
Ceramic:					
Zirconia	6.05	12	72.60	3.6	15.0
Alumina	3.97	48	190.56	14.5	39.4
Butyl Benzyl Phthalate	1.122	16.63	18.66	5.0	3.9
B76 Butvar	1.1	11.09	12.20	3.4	2.5
Total		330.25	483.35	100.0	100.0

3.2.2 Tapecasting

The slurries were aerated by unscrewing the lid and lightly tapping the bottom of the container under a fume hood. After removing any bubbles that may have been created during ball milling, slurries were individually coated onto a glass substrate using a doctor blade, as shown in Figure 3.1. A doctor blade with a gap height of 600 *mm* was used for the fabrication of all the samples, except for the tensile sample, where a doctor blade with a gap height of 350 *mm* was used. After tapecasting, the tapes were thoroughly dried until all the solvents evaporated.

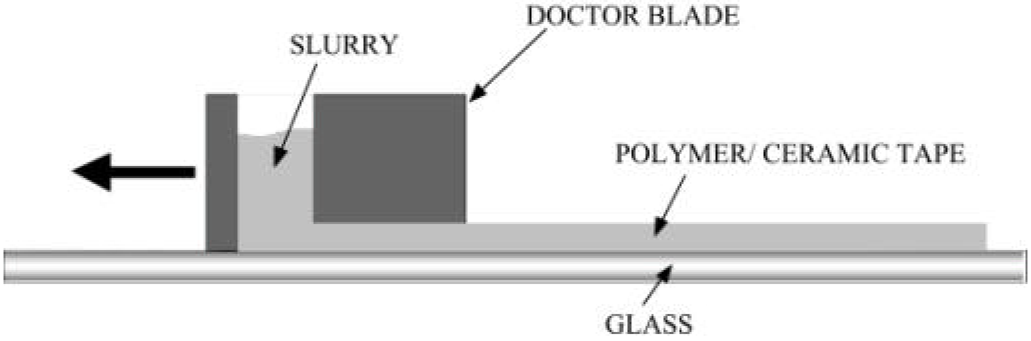

Figure 3.1 A schematic of tapecasting.

3.2.3 Lamination

The dried tapes were stripped from the glass and punched into rectangular sheets. The rectangular sheets were then stacked within a metallic die and pressed at 120^{o}C under a pressure of 40 *MPa* for 15 minutes to bond the tapes, as shown in Figure 3.2.

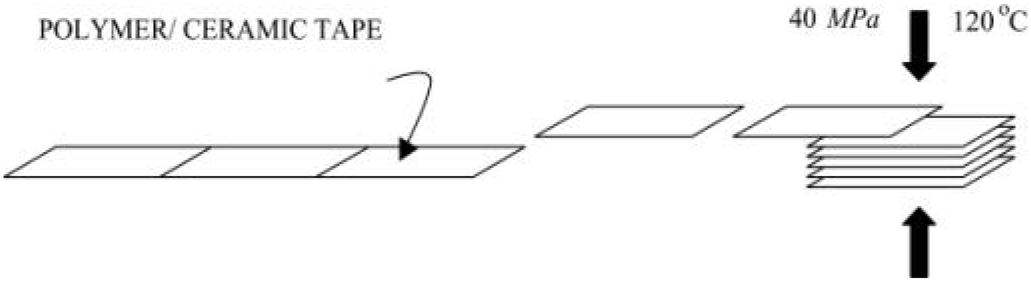

Figure 3.2 A schematic of lamination.

3.2.3.1 Lamination of particulate composites for compression testing

The dried coatings were punched into 23 *mm* × 47 *mm* rectangular sheets, with a thickness of 90 *mm*. The rectangular sheets with the same composition were then laminated. The total thickness of the samples was about 8 *mm*.

3.2.3.2 Lamination of particulate laminates for compression testing

Tapes of 23 *mm* × 47 *mm* × 90 *mm* were stacked sequentially to form symmetric particulate laminates where each alternating layer consisted of a particulate composite. The layer containing more Y-TZP was designated by the "soft layer"; the layer containing more Al_2O_3 was designated by the "hard layer". The ratios of layer thickness varied from 1:4 to 4:1. For 1:1, both layers were 450 *mm* thick; for 1:2 (or 2:1) and 1:4 (or 4:1) the thinner layer was 450 *mm* thick and thicker layer was 900 *mm* thick and 1800 *mm*, respectively, prior to sintering. The total thickness of each billet was about 8 *mm*.

3.2.3.3 Lamination of particulate composites and laminates for tensile testing

Tapes with a length of 76 *mm*, a width of 38 *mm*, and a thickness of 40 *mm* were laminated to form a billet. For the laminates, the ratios of layer thickness varied from 1:1 to 1:4. For 1:1, each layer was one-tape thick; for 1:2 (or 2:1) and 1:4 the thinner layer was one-tape thick and thicker layer were two-tapes and four-tapes thick, respectively. The total thickness of each billet was about 2 *mm* (= 50 tapes × 40 *mm*).

3.2.4 Binder Burn-Out

The green billets were placed on an alumina powder bed inside of high-purity alumina crucible. The binder was removed by pyrolysis in a low-temperature furnace with a flowing air atmosphere. Table 3.2 shows the burnout schedule. Slow heating rates were used in order to prevent cracking, bloating or bubble formation.

Table 3.2 Burn-out schedule.

Temperature Range	Heating Rate	Total Time Elapsed
25^oC - 100^oC	60^oC/hr	1.25 hrs
100^oC - 135^oC	4^oC/hr	8.75 hrs
135^oC - 275^oC	2^oC/hr	67.5 hrs
275^oC - 400^oC	5^oC/hr	25 hrs
400^oC - 600^oC	60^oC/hr	3.33 hrs

3.2.5 Sintering

Following binder-burnout, the billets were covered loosely with another crucible and pressureless sintered in air at 1450°C for 1 hour using a high temperature furnace. The heating rate and cooling rate were 5°C/min and 15°C/min, respectively. After sintering, the shrinkage of the sample thickness was about 22%.

3.2.6 Designations

The particulate composites in this study were designated by the volume fraction of Al_2O_3; for example, 20A contained 20 vol% Al_2O_3 and 80 vol% Y-TZP. The particulate laminates were designated by their constituent layers and ratios of layer thickness, *e.g.* 20A/40A (1:1) consisted of 20A and 40A layers, where the ratio of layer thickness, 20A to 40A, was 1:1. A summary of all the particulate composites and laminates fabricated in this study is listed in Table 3.3. Individual specimens were cut from these billets and ground to final shape for different tests using a diamond wafering blade and a diamond grinding wheel. Some compositions, indicated with an asterisk in Table 3.3, were fabricated but cracked during processing due to differential sintering rates and thermal expansion mismatch between layers [104] and therefore were not tested (see Figure 3.3).

Table 3.3 Composition of particulate composites and particulate laminates used in this study. Asterisk indicates compositions that fractured during processing.

Samples for compression strain-rate change testing					
Particulate Composites	20A	40A	50A	60A	80A
Particulate Laminates	1 : 1	1 : 2	2 : 1	1 : 4	4 : 1
	20A/40A	20A/40A	20A/40A		
	20A/50A	20A/50A	20A/50A		
	20A/60A	20A/60A	20A/60A	20A/60A	20A/60A
	20A/80A	20A/80A	*	*	*
	40A/80A	40A/80A	40A/80A		
	50A/80A	50A/80A	50A/80A		
	60A/80A	60A/80A	60A/80A		
	40A/60A	40A/60A			
Samples for tensile strain-rate-change testing					
Particulate Composites	20A	60A			
Particulate Laminates	1 : 1	1 : 2	2 : 1	1 : 4	
	20A/60A	20A/60A	20A/60A	20A/60A	
Samples for elongation-to-failure testing					
Particulate Composites	20A				
Particulate Laminates	1 : 1	1 : 2			
	20A/60A	20A/60A			

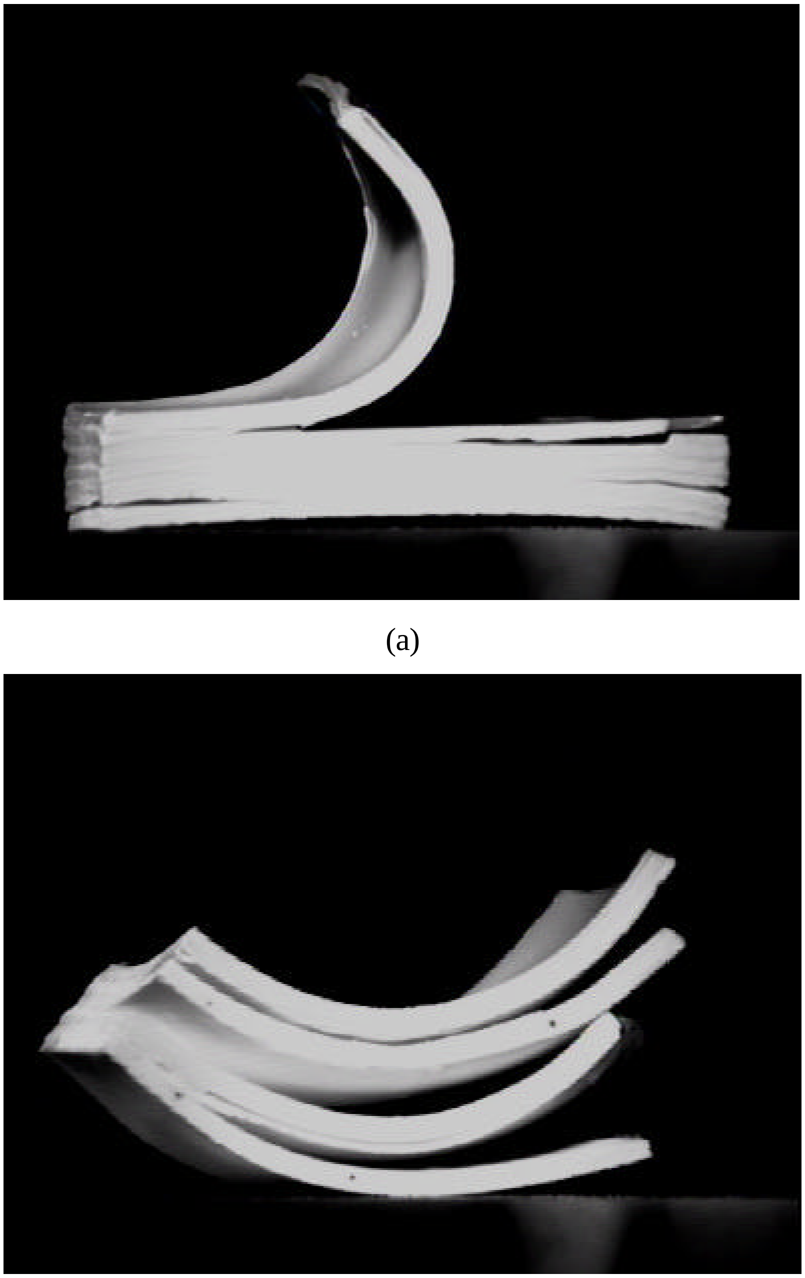
(a)

(b)

Figure 3.3 The cracked samples after sintering, (a) 20A/80A (2:1); (b) 20A/80A (4:1).

3.3 MICROSTRUCTURE ANALYSIS

3.3.1 Density Measurement

The density of each billet was measured at room temperature based on the Archimedes principle with distilled water as the immersion medium, using a Mettler Toledo ME-33360 density determination kit. The bulk density, r, was calculated from

$$r = \frac{D}{(M - S)} \cdot r_{water} \tag{3.1}$$

where D is the dry mass, M is the mass of the specimen saturated with water, S is the mass of the specimen suspended in water, and r_{water} is the density of the water at the measurement temperature. The dry mass, D, of the specimens was first determined. Then, the specimens were placed in distilled water and boiled for 2 hours to remove adsorbed air from the surface and fill in surface features with water. After cooling down to room temperature, the suspended mass, S, and the saturated mass, M, were measured. The balance had a precision of 0.0001 *g*.

3.3.2 Scanning Electron Microscopy

Specimens were prepared for analysis in a Scanning Electron Microscope (SEM) by grinding and polishing with diamond discs, pastes, and suspensions with a final grit size of 1 *mm*, using a Sturers RotoPol-11 auto-polishing machine. Table

3.4 lists the polishing schedule. After polishing, the specimens were thermally etched at 1370^{o}C for 20 minutes to reveal grain structure. Samples were sputter-coated using an Au-Pt target to prevent surface charging. SEM images were taken in digital format using a Hitachi S-4500 field-emission SEM in secondary electron mode.

Table 3.4 The polishing schedule for SEM specimens.

	Diamond Suspension	Lubricant	Speed (*rpm*)	Force (*N/mm*^{2})	Time (*min*)
68 *mm* diamond grind disc	N/A	Water	150	20	As-needed
30 *mm* diamond grind disc	N/A	Water	150	20	2
12 *mm* diamond grind disc	N/A	Water	150	20	2
diamond pad	6 *mm*	DP-Lubricant Green	150	20	5
diamond pad	3 *mm*	DP-Lubricant Green	150	20	5
diamond pad	1 *mm*	DP-Lubricant Green	150	20	5

SEM micrographs were manually traced onto transparencies where each color represented a different phase and the grain boundaries were traced in black. The transparencies were then scanned and analyzed using image analysis software (Clemex Vision Version 2.2, Quebec, Canada). Mean grain sizes and grain size distributions, based on the equivalent circular diameter of individual grains, were measured. Equivalent circular diameter, D, was defined as $D = (4A/p)^{1/2}$, where A was the cross-sectional area of the grain. The average grain size, $\bar{d}$, was 1.27 times the mean equivalent circular diameter [105].

3.3.3 Transmission Electron Microscopy

Specimens for analysis in a Transmission Electron Microscope (TEM) were ground to about 100 mm, using a surface-grinding machine and then manually polished using diamond pastes with a final grit size of 1 mm. After polishing, the specimens were about 40 mm thick and then further thinned using an ion beam, with a low angle milling and polishing system. TEM images were taken in digital format using JEOL 2010 TEM with GATAN digital photography system.

3.3.4 Optical Microscopy

Cross sections of particulate laminates before and after testing and the morphology of the superplastically deformed samples were observed using an optical microscope (Zeiss Inc., West Germany). All the optical micrographs were captured digitally using image analysis software (Clemex Vision Version 2.2, Quebec, Canada) at a resolution of 640 × 480 pixels.

3.4 MECHANICAL TESTING

3.4.1 Compression Strain-Rate-Change (SRC) Testing

The sintered particulate composites and laminates were cut and ground into rectangular bars with the dimensions 6 *mm* × 4 *mm* × 4 *mm*. For the particulate composites, the longest edge was perpendicular to the laminated layer interfaces. For the particulate laminates, the largest dimension was either perpendicular or parallel to the layer interfaces. Figure 3.4 shows a schematic of particulate composites and particulate laminates under compression. There were two configurations for particulate laminates: one was isostress orientation, where the applied stress was perpendicular to the layer interface, as shown in Figure 3.4b; the other was isostrain orientation, where the applied stress was parallel to the layer interface, as shown in Figure 3.4c.

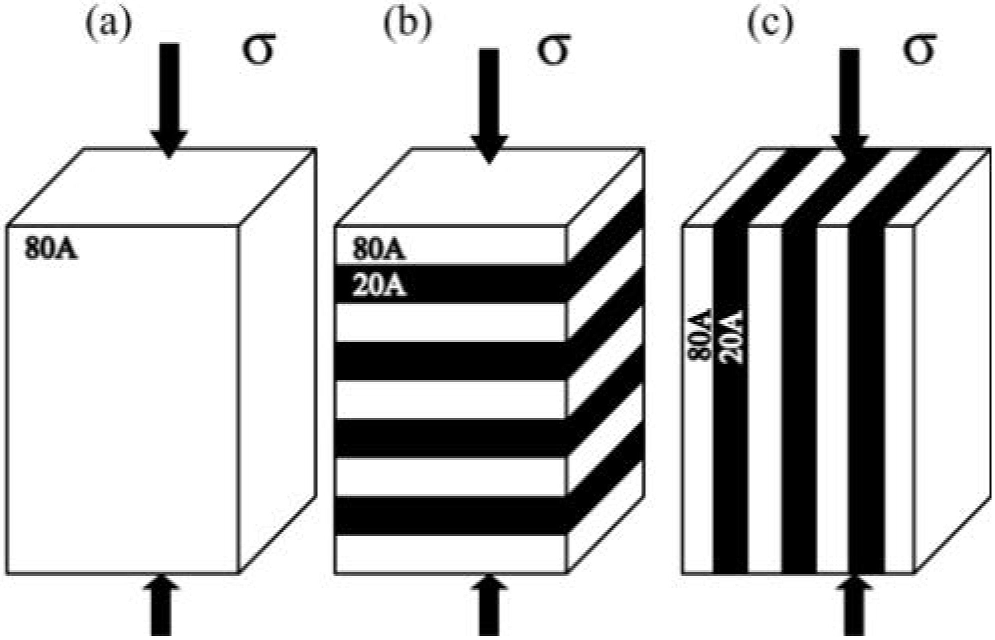

Figure 3.4 Illustrations of particulate composites and particulate laminates: (a) particulate composite; (b) particulate laminate, isostress orientation; (c) particulate laminate, isostrain orientation.

Compression SRC testing was performed at 1300 - 1450^{o}C in air using a MTS (Material Testing Systems, Inc.) model 657.01 split tube furnace with $MoSi_2$ heating elements. Loading was applied using a computer-controlled MTS 810 servohydraulic test frame equipped with SiC compression fixtures and water-cooled mounts. A schematic of furnace, compression fixture, and load cell is shown in Figure 3.5. The compression fixture consisted of upper and lower compression rods (A) held in place with stainless steel mounts (B). The mounts were directly attached to the actuator and to the load cell (C). In this study, 5 *kN* load cell was used. As shown in Figure 3.5, the specimen was placed between two SiC compression platens, which were polished with 45 *mm* diamond suspension to remove the oxides on the surface before testing. A small amount of a boron nitride/isopropanol suspension was applied on the surface of these two SiC compression platens. After evaporation of the alcohol, the boron nitride powder acted as a lubricant between the test specimen and the SiC compression platens, minimizing the effects of friction and barreling.

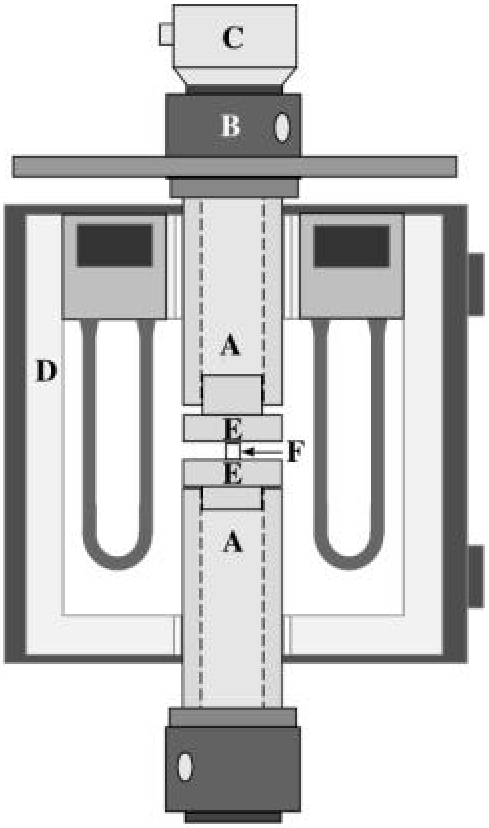

A: SiC compression rods

B: Water-cooled stainless steel mount

C: Load cell

D: Furnace

E: SiC compression platens

F: Specimen

Figure 3.5 A schematic of furnace, compression fixture, and load cell used in compression SRC testing.

Compression SRC testing procedure was programmed using MTS Multipurpose Testware (MPT), version 3.0A. The testing included nine steps in engineering strain rate, $\dot{e}_{eng}$, which was defined as

$$\dot{e}_{eng} = \frac{V}{h_0} \tag{3.2}$$

where V was the crosshead speed, h_0 was the initial sample height at the beginning of each step. A prestrain of approximately 2% was initially applied at a strain rate of 1.00 × 10^{-4} s^{-1} in order to ensure mating between the sample and the compression platens and to stabilize the sample microstructure. Following the prestrain step, seven steps with strain rates from 1.00 × 10^{-5} s^{-1} up to 3.16 × 10^{-4} s^{-1} were applied. The strain rate of 1.00 × 10^{-4} s^{-1} was repeated in the final step of the series to test the repeatability of flow stress. The total engineering strain was about 11%. Table 3.5 summarizes the procedure used for the compression SRC testing.

Table 3.5 The procedure used for compression SRC testing.

Initial sample height: 6 *mm*						
Zero position: 0 *mm*						
Step	Strain (%)	Engineering strain rate (s^{-1})	Final position (*mm*)		Final height of sample (*mm*)	Crosshead speed (*mm/s*)
			Relative	Absolute		
1	2	1.00 × 10^{-4}	-0.1200	0.1200	5.8800	6.000 × 10^{-4}
2	1	1.00 × 10^{-5}	-0.0588	0.1788	5.8212	5.880 × 10^{-5}
3	1	1.77 × 10^{-5}	-0.0582	0.2370	5.7630	1.030 × 10^{-4}
4	1	3.16 × 10^{-5}	-0.0576	0.2946	5.7054	1.821 × 10^{-4}
5	1	5.62 × 10^{-5}	-0.0571	0.3517	5.6483	3.206 × 10^{-4}
6	1	1.00 × 10^{-4}	-0.0565	0.4082	5.5918	5.648 × 10^{-4}
7	1.5	1.77 × 10^{-4}	-0.0839	0.4921	5.5079	9.898 × 10^{-4}
8	2	3.16 × 10^{-4}	-0.1102	0.6022	5.3978	1.741 × 10^{-3}
9	1	1.00 × 10^{-4}	-0.0540	0.6562	5.3438	5.398 × 10^{-4}
Final sample height: 5.3438 *mm*						
Total engineering strain: 11%						

Displacement was measured using a linear variable differential transducer (LVDT) mounted on the actuator of the test frame. Engineering strain, e_{eng}, and engineering stress, s_{eng}, were calculated from the displacement and load, respectively, by assuming that the displacement of the crosshead corresponded to the reduction in the height of the specimen, after compensation for elastic deflection, using standard definitions for e_{eng} and s_{eng}:

$$e_{eng} = \frac{\Delta h}{h_0} \tag{3.3}$$

$$s_{eng} = \frac{F}{A_0} \tag{3.4}$$

where Δh is the absolute displacement, h_0 is the initial sample height, F, is the load, and A_0 is the initial cross-sectional area of the sample. Figure 3.6 shows the data from a typical compression SRC test at 1350^{o}C for a 50A particulate composite.

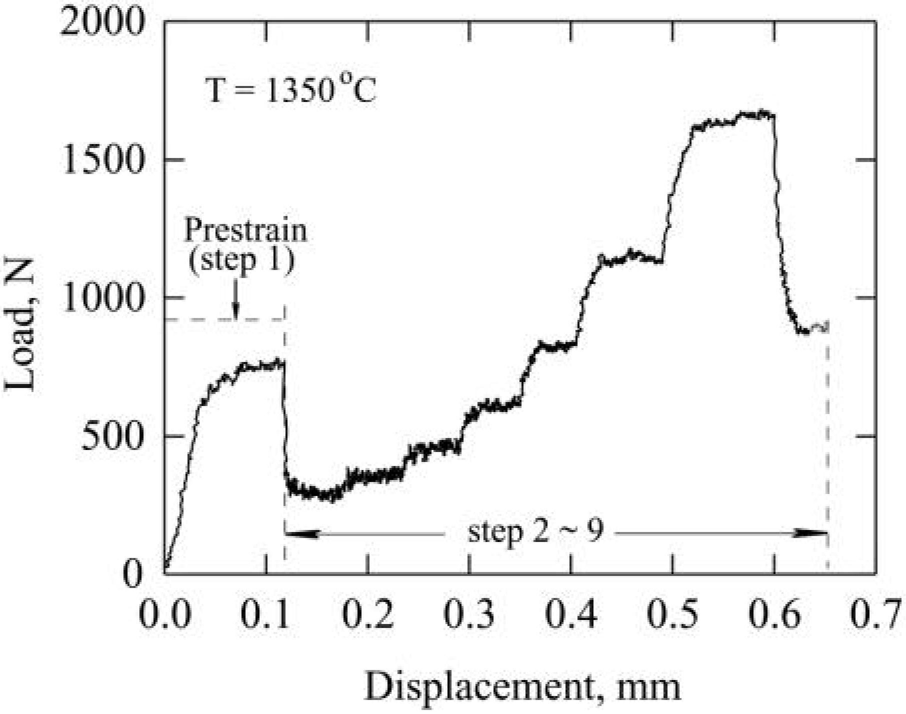

Figure 3.6 Data for a typical compression SRC testing at 1350°C for a 50A particulate composite.

Assuming uniform deformation and volume conservation, true strain, e_{true}, and true stress, s_{true}, were calculated from engineering strain and engineering stress from

$$e_{true} = -\ln(1 - e_{eng}) \tag{3.5}$$

$$s_{true} = s_{eng}(1 - e_{eng}) \tag{3.6}$$

where $e_{true} > 0$, $e_{eng} > 0$. In addition, true strain rate, $\dot{e}_{true}$, was given as

$$\dot{e}_{true} = \frac{V}{h_i} \tag{3.7}$$

where h_i was the instantaneous sample height. Combining Equations 3.2 and 3.7,

$$\dot{e}_{true} = \dot{e}_{eng} \cdot \frac{1}{1 - e_{eng}} \tag{3.8}$$

since

$$e_{eng} \equiv \frac{h_0 - h_i}{h_0} \tag{3.9}$$

Due to the small engineering strain ($\leq 2\%$) for each step, the true strain rate was approximately equal to the engineering strain rate with a maximum deviation of 2%.

3.4.2 Tensile SRC Testing

Tensile testing specimens were diamond-machined from the billets (13.85 *mm* × 59.55 *mm* × 0.8 *mm*) with the largest dimension parallel to the layer interfaces. The gage length of the specimens was 27.25 *mm*. The thickness of the specimens was 0.8 *mm*. A schematic diagram of the tensile specimen was shown in Figure 3.7.

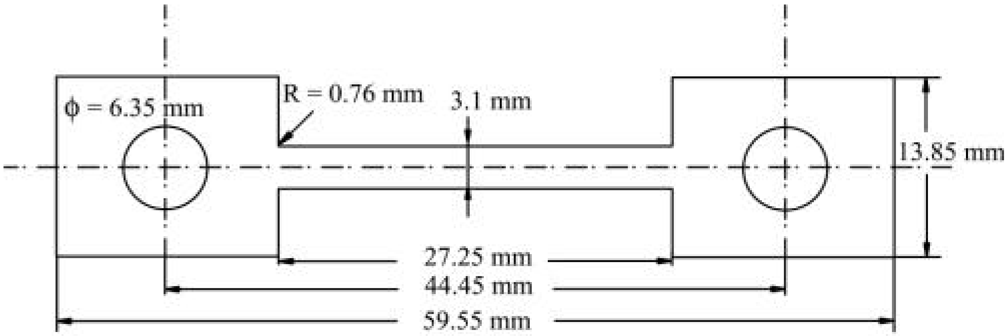

Figure 3.7 A schematic diagram of a tensile specimen.

Tensile SRC testing was performed in a vacuum system (~ 10^{-5} Pa) at 1350°C, using a Testmaster 3-8-3W High-Temperature Vacuum/Inert-Gas Furnace with a 50 mm × 50 mm × 150 mm working hot zone. Loading was applied using a computer-controlled MTS Alliance™ RF/100 test frame with a 5 kN load cell. The tensile fixture, which was essentially a universal joint with a pin-loading mechanism for the test sample, was made of thoriated tungsten and was designed to minimize the misalignment of the test system. The specimen was pin-loaded to the tensile fixture using two SiC pins. The applied load was parallel to the layer interfaces, *i.e.* isostrain orientation.

Tensile SRC testing procedure was programmed using Material Testing Software TestWorks® 4. The testing included nine steps in true strain rate, $\dot{e}_{true}$, which was defined as

$$\dot{e}_{eng} = \frac{V}{l_i} \tag{3.10}$$

where V was the crosshead speed, l_i was the instantaneous gage length. During the testing, true strain rate started with 1.00 × 10^{-4} s^{-1} and then varied from 1.00 × 10^{-5} s^{-1} to 3.16 × 10^{-4} s^{-1}. The strain rate of 1.00 × 10^{-4} s^{-1} was repeated in the final step of the procedure. The range of the strain rates and the strain for each step in the tension tests were the same as the compression tests, except that the tension SRC testing procedure required ~ 4% strain for the prestrain step (*i.e.* step 1) to reach a reasonably steady state. During the compression SRC testing, the engineering strain rate was controlled, instead of true strain rate, due to the limitation in the software. During the tension SRC testing, the crosshead speed and instantaneous gage length were recalculated every second so that the strain rate was a very close approximation to the true strain rate.

The crosshead movement was monitored by the computer equipped with a data acquisition system. Engineering strain, e_{eng}, and engineering stress, s_{eng}, were obtained by assuming that the change in displacement of the crosshead corresponded to the increase in the gage length of the specimen. The relationships were given as

$$e_{eng} = \frac{\Delta l}{l_0} \tag{3.11}$$

$$s_{eng} = \frac{F}{A_0} \tag{3.12}$$

where Δl is the absolute displacement, l_0 is the initial sample gage length, F, is the load, and A_0 is the initial cross-sectional area of the gage section. True strain, e_{true}, and true stress, s_{true}, were given as

$$e_{true} = \ln(1 + e_{eng}) \tag{3.13}$$

$$s_{true} = s_{eng}(1 + e_{eng}) \tag{3.14}$$

where $e_{true} > 0$, $e_{eng} > 0$, assuming the volume conservation.

3.4.3 Elongation-to-Failure Testing

For some selected particulate composites and particulate laminates, tensile SRC test was directly followed by an elongation-to-failure test at 1350°C with a true strain rate of 1.00×10^{-4} s^{-1}. The elongation on the gage-length portion of the specimens was measured. The elongation-to-failure, e_f, was given as

$$e_f = \frac{\Delta l_{\max}}{l_0} \tag{3.15}$$

where $\Delta l_{\max}$ was the maximum displacement at failure.

Chapter 4

High-Temperature Deformation of Al_2O_3/Y-TZP Particulate Composites in Compression

4.1 INTRODUCTION

One prerequisite for achieving superplasticity in ceramics is a fine grain size that is resistant to both static and dynamic grain growth. Particulate composites consisting of two well-mixed phases can exhibit high resistance to coarsening [101] and therefore provide a path for achieving superplasticity [56]. The high-temperature deformation behaviors of particulate composites consisting of Al_2O_3 and Y-TZP have been studied extensively, largely because these two-phase composites are stable in air at high temperatures, do not form intermediate compounds, and can exhibit remarkably high tensile elongations of up to 625% [21].

Previous studies of Al_2O_3/Y-TZP composites have shown that, when tested in tension, the stress exponent is about 2 over a large range of compositions (0 - 80 wt% Al_2O_3), strain rate (10^{-7} - 10^{-2} s^{-1}) and temperature (1250 - 1650^{o}C), suggesting that a common deformation mechanism may exist under these conditions [8,11,20]. Most of the studies of Al_2O_3/Y-TZP particulate composites have aimed at achieving superplasticity; thus, testing temperatures in these studies have generally been very high (1450 - 1650^{o}C). At these temperatures, dynamic grain growth and other microstructural changes, such as alteration of grain shape and cavitation, have been observed [8,35]. As suggested by Nieh *et al.* [30], differences in grain size between composites with different compositions, as well as microstructural changes during testing at high temperatures, make the interpretation of deformation mechanisms quite challenging.

In the present investigation, the influence of Al_2O_3 volume fraction on the deformation response of Al_2O_3/Y-TZP particulate composites at elevated temperature is studied for composites ranging from 20 to 80 vol% Al_2O_3. Ultra-high-purity Al_2O_3 and high-purity Y-TZP are used to fabricate specimens in order to minimize impurity content. Processing routes and processing temperatures are selected to minimize differences in grain size with composition. Specimens were tested in compression at a relatively low temperature of 1350^{o}C and to relatively small strains (engineering strain of ~ 11%) to minimize microstructural changes during testing. With these precautions, the high-temperature deformation behaviors of five Al_2O_3/Y-TZP particulate composites containing from 20 to 80 vol% Al_2O_3 are experimentally evaluated. The data obtained are compared to data available in the literature and to existing theoretical models for particulate composites.

4.2 EXPERIMENTAL RESULTS

4.2.1 Microstructure

Scanning electron micrographs of the Al_2O_3/Y-TZP particulate composites containing 20 to 80 vol% Al_2O_3 are shown in Figure 4.1 both before and after SRC testing at 1350^oC. The grains with the light shading are Y-TZP and the grains with the dark shading are Al_2O_3. The Al_2O_3 and Y-TZP phases are generally well-dispersed except at high volume fractions where some clustering of the phases is apparent. All of the materials exhibit high densities (≥ 98%) and fine grain sizes. Narrow grain size distributions are observed for both phases, as shown in Figure 4.2. Before testing, the mean grain size of Al_2O_3 ranges from 0.46 to 0.35 *mm* and decreases slightly with increasing volume fraction of Y-TZP, while the mean grain size of Y-TZP varies from 0.22 to 0.32 *mm*, with the smallest size occurring at the greatest Al_2O_3 content. A comparison of the microstructures before and after testing at 1350^oC is shown in Figure 4.1 and indicates that the grain shapes remain equiaxed and that very little grain growth occurred during testing, as shown in Table 4.1. In addition, no measurable change in density was detected after testing, indicating that appreciable cavitation did not occur.

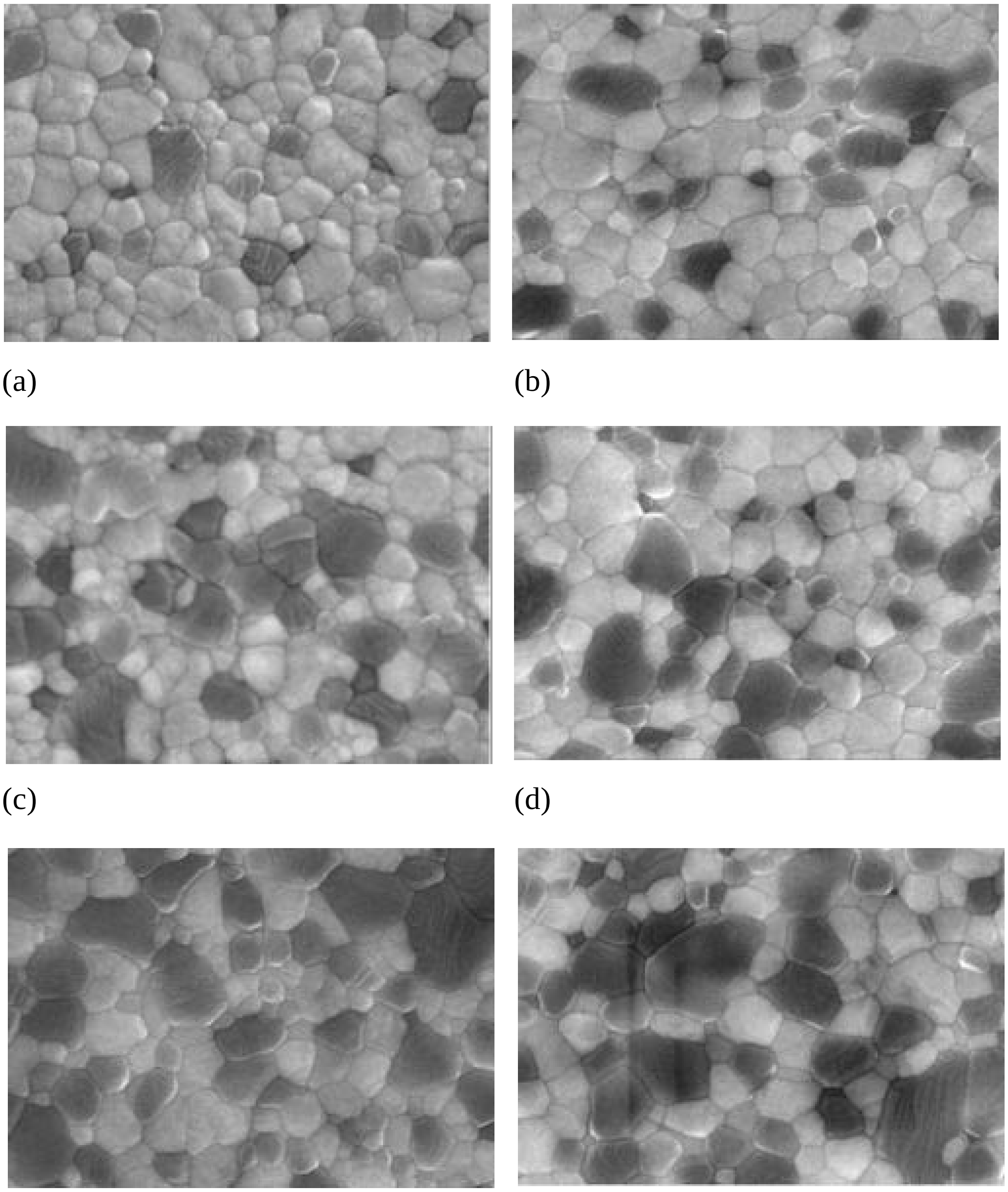

(a) (b)

(c) (d)

(e) (f)

Figure 4.1

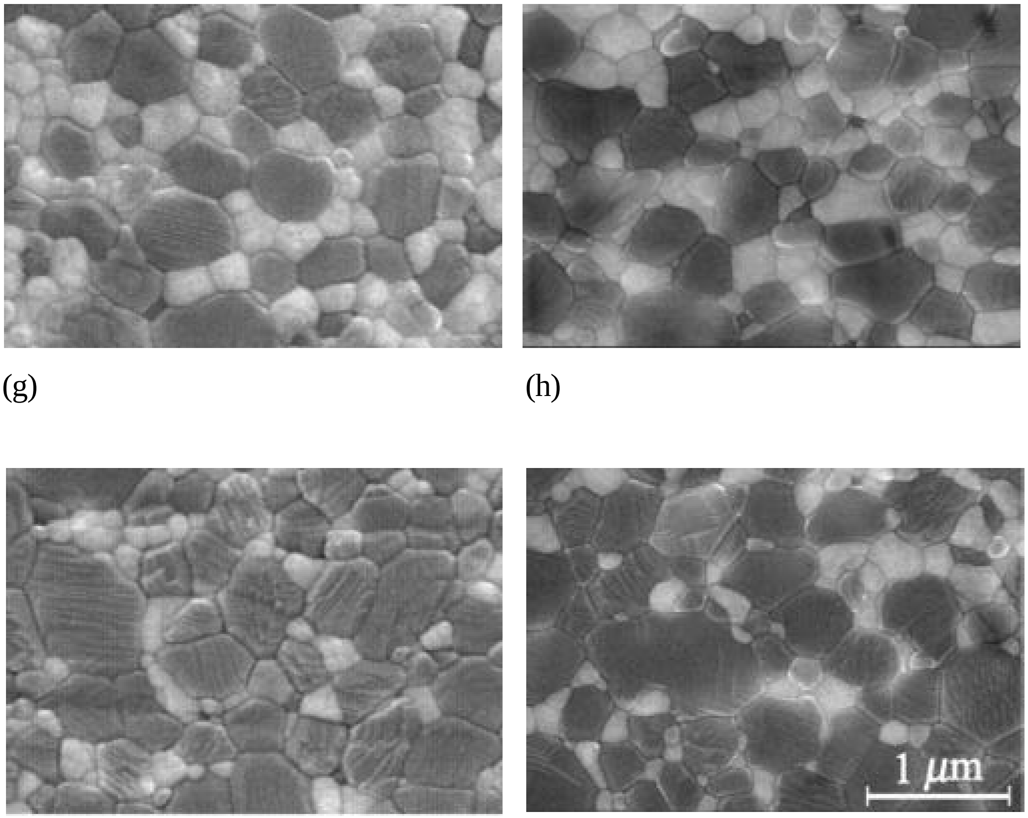

(g) (h)

(i) (j)

Figure 4.1 Scanning electron micrographs for Al_2O_3/3Y-TZP particulate composite specimens (a) 20A before testing, (b) 20A after testing, (c) 40A before testing, (d) 40A after testing, (e) 50A before testing, (f) 50A after testing, (g) 60A before testing, (h) 60A after testing, (i) 80A before testing, and (j) 80A after testing. These tests were performed at 1350°C.

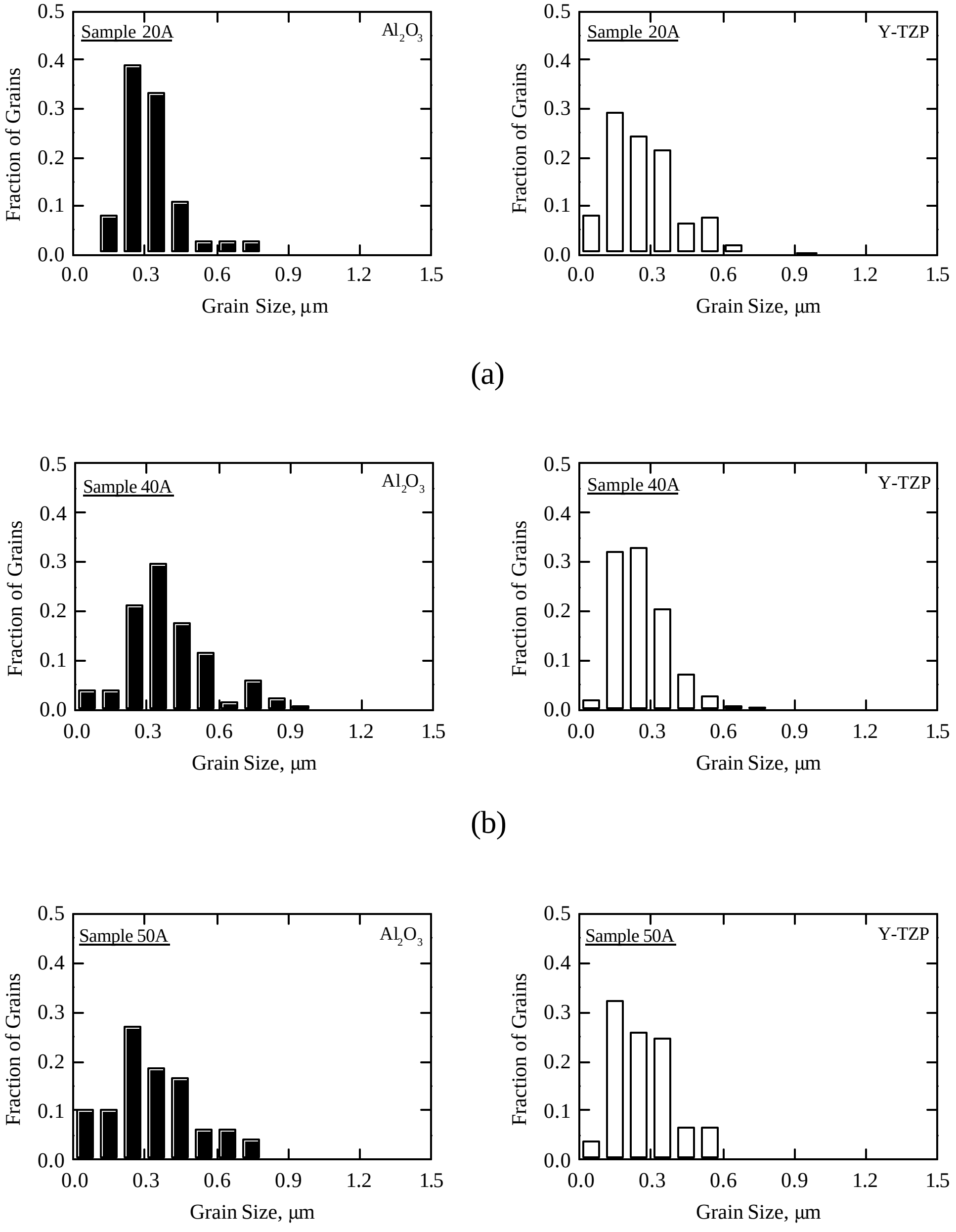

(a)

(b)

(c)

Figure 4.2

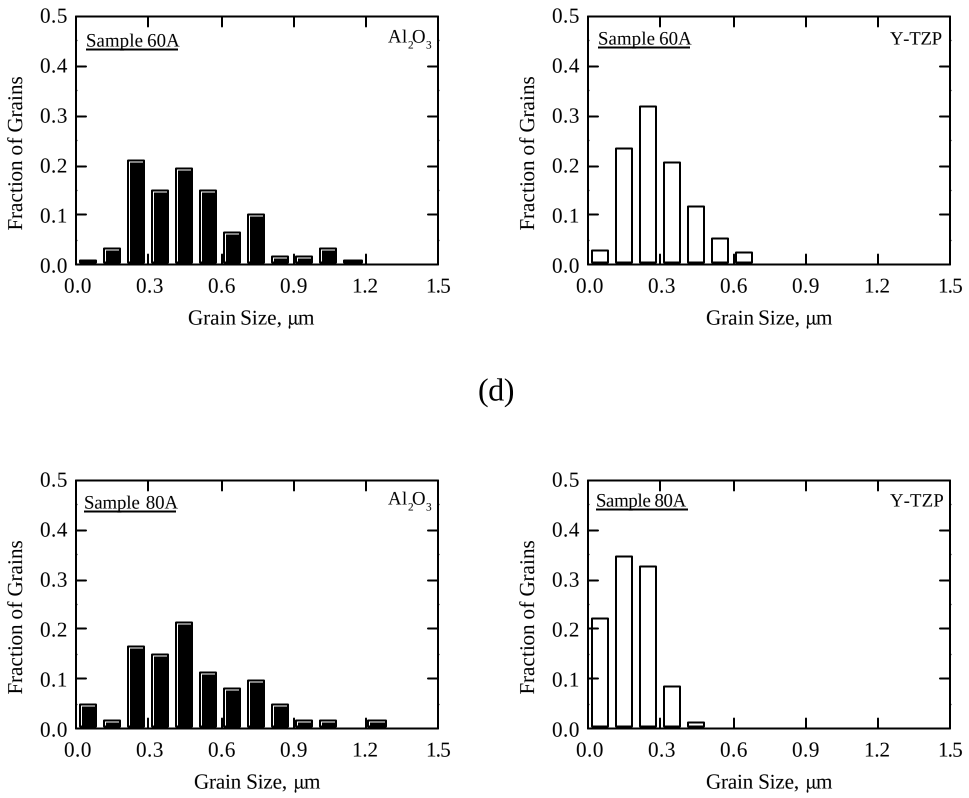

(d)

(e)

Figure 4.2 Grain size distributions for (a) 20A, (b) 40A, (c) 50A, (d) 60A, and (e) 80A samples before testing.

Table 4.1 Mean grain sizes and their standard deviations for Al_2O_3/Y-TZP particulate composites before and after deformation at 1350°C.

Particulate Composites	Relative Density (%)	Before Deformation		After Deformation	
		$\bar{d}_{Al_2O_3}(mm)$	$\bar{d}_{Y-TZP}(mm)$	$\bar{d}_{Al_2O_3}(mm)$	$\bar{d}_{Y-TZP}(mm)$
20A	99.1	0.35 ± 0.14	0.32 ± 0.15	0.35 ± 0.15	0.32 ± 0.12
40A	98.0	0.39 ± 0.17	0.29 ± 0.12	0.39 ± 0.16	0.31 ± 0.11
50A	98.2	0.40 ± 0.16	0.29 ± 0.11	0.41 ± 0.18	0.32 ± 0.12
60A	99.4	0.46 ± 0.22	0.30 ± 0.11	0.46 ± 0.20	0.30 ± 0.11
80A	98.2	0.46 ± 0.18	0.22 ± 0.07	0.46 ± 0.24	0.24 ± 0.09

A representative bright-field transmission electron micrograph of a Al_2O_3/Y-TZP particulate composite containing 50 vol% Al_2O_3 and 50 vol% Y-TZP is shown in Figure 4.3 after SRC testing at 1350°C. The grains with light contrast are Al_2O_3 and the grains with dark contrast are Y-TZP. Special efforts have been made to examine the structure along grain boundaries, and in particular, at grain boundary triple junctions. More than 20 grains were examined and no experimental evidence was found to indicate the existence of glassy phase in the Al_2O_3/Y-TZP particulate composites. This indicates that the grain boundaries and triple junctions of the material examined in this study are likely free of the low melting temperature glassy phases that were present in some previous studies [19,40] and which can make interpretation of deformation mechanisms more difficult.

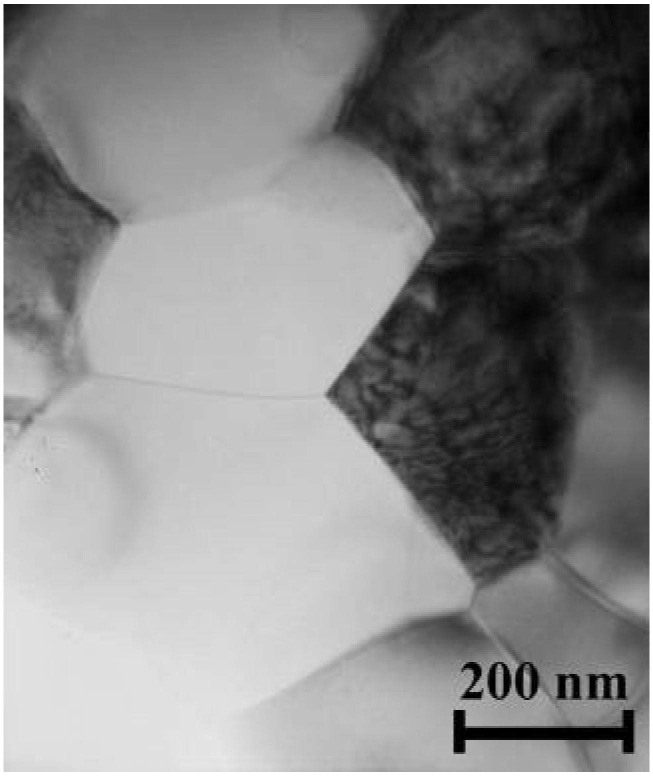

Figure 4.3 A transmission electron micrograph of 50 vol% Al_2O_3/50 vol% Y-TZP particulate composite after testing at 1350°C.

4.2.2 Mechanical Behavior

In general, the strain rate, $\dot{e}$, in the deformation of polycrystalline materials at elevated temperature may be expressed using the phenomenological equation for creep [68]:

$$\dot{e} = A\left(\frac{s}{E}\right)^{n}\left(\frac{b}{d}\right)^{p}\exp\left(-\frac{Q_c}{RT}\right) \tag{4.1}$$

where s is the stress, E is the dynamic, unrelaxed Young's modulus, T is the absolute temperature, b is the magnitude of Burgers vector, d is the grain size, n is the stress exponent, p is the inverse grain-size exponent, Q_c is the activation energy for creep, R is the gas constant, and A is a material constant.

Data from a representative compression SRC test at 1350°C of the 20A specimen are shown in Figure 4.4. The total strain for this test is $e = 0.126$. After a brief transient at every rate change, a reasonably steady-state stress is achieved. As is demonstrated in Figure 4.4 by the repeated steps at a strain rate of 10^{-4} s^{-1}, the flow stress at a given rate is nearly constant over the range of strains imposed in any single SRC test. Behaviors similar to those shown in Figure 4.4 were observed in SRC tests of all the composites tested, except for 60A and 80A, where some strengthening occurred at the end of the test, likely because of slight grain coarsening. As discussed before, the results from measured grain size before and after deformation do not definitively support grain growth. However, the occurrence of slight grain coarsening for 60A and 80A during the deformation is still possible due to the limitations in the accuracy of grain-size measurement (see Table 4.1) and the strong sensitivity of flow stress to grain size.

The relationships between true stress and strain rate are plotted on log-log scales in Figure 4.5 for each of the five compositions tested at 1350°C. At a given strain rate, the flow stress decreases as the volume fraction of Y-TZP increases. The negative curvature apparent in the data of Figure 4.5 indicates a decrease in stress exponent with increasing stress for a given composition. Stress exponents vary from approximate 2 to 3, as indicated by the slopes identified in Figure 4.5. A value of $n = 3$ is observed at low Al_2O_3 content and low stresses, while a value of $n = 2$ is observed at stresses above approximate 20 to 30 *MPa*. The strain rate associated with the transition from $n = 3$ to $n = 2$ increases as the Al_2O_3 volume fraction decreases. At the highest stresses ($s > 100$ *MPa*) and highest Al_2O_3 volume fractions, the apparent stress exponent is reduced to values of less than 2, which may be the result of slight coarsening of the 60A and 80A microstructures during SRC tests, leading to strengthening in the latter SRC test steps.

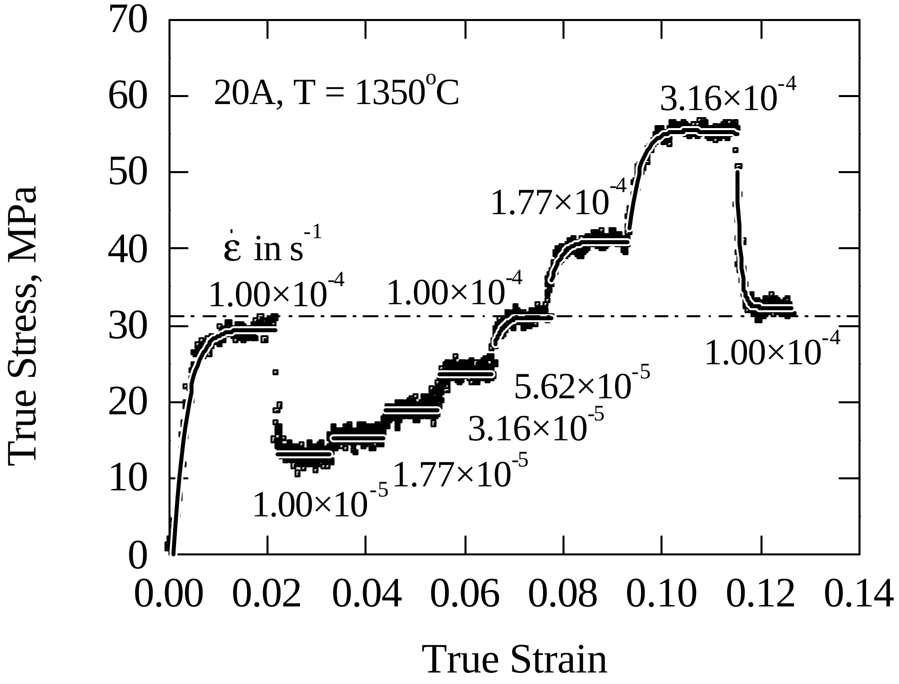

Figure 4.4 A plot of true stress versus true strain for the 20A specimen during a representative compression SRC test. The dashed line indicates the flow stress at a strain rate of 1.00×10^{-4} s^{-1}.

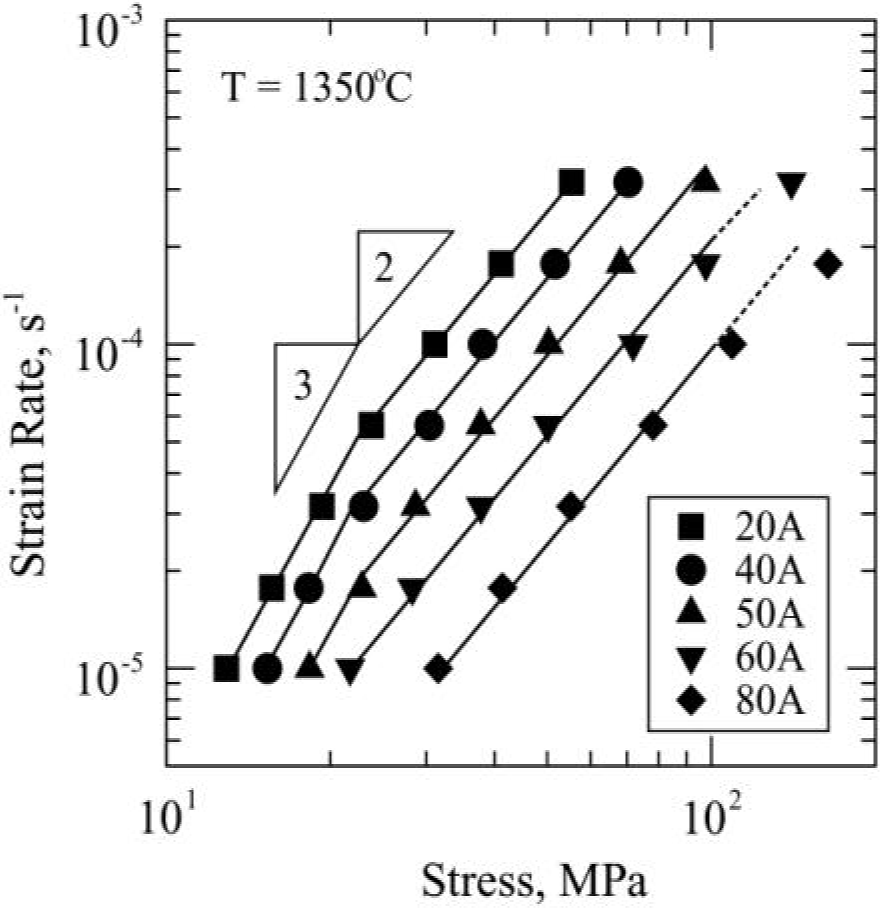

Figure 4.5 Strain rate versus stress on log-log scales for Al_2O_3/Y-TZP particulate composites.

Figure 4.6 shows the strain rate dependence of the stress for 20A, 40A, and 50A particulate composites over the temperature range from 1300°C to 1450°C. In the current study, we did not take into account the temperature dependence of Young's modulus, E, and did not compensate Young's modulus since there are no available Young's modulus data for Al_2O_3/Y-TZP particulate composites. The stress exponents for all the temperatures tested were measured to be 2 - 3. The negative curvature is evident at lower temperatures. Figure 4.7 shows the temperature dependence of the strain rate for 20A, 40A, and 50A at 20 *MPa*, 30 *MPa*, and 50 *MPa*. Since $\dot{e} \propto \exp\left(-\frac{Q_c}{RT}\right)$, activation energy, Q_c, can be determined from the slope of the lines in Figure 4.7, using the relationship $\frac{d(\log \dot{e})}{d(1/T)} = -\frac{Q_c}{R\ln 10}$. Activation energies of 660, 670 and 740 kJ/mol were calculated for 20A, 40A, and 50A at 20 *MPa*, increasing with an increase of the volume fraction of Al_2O_3, as shown in Figure 4.8, which are in good agreement with the previous studies [20]. In addition, the activation energies decrease with increasing stress (see Figure 4.8), which may result from slight grain growth at high stress [32].

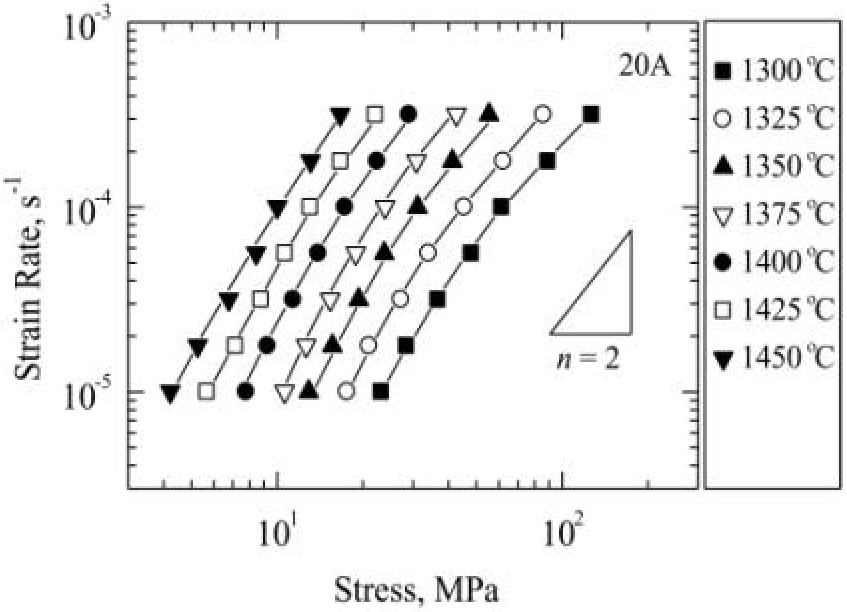
Strain Rate, s^{-1}
Stress, MPa
10^{-3}
10^{-4}
10^{-5}
10^{1}
10^{2}
20A
n = 2
■ 1300 ℃
○ 1325 ℃
▲ 1350 ℃
▽ 1375 ℃
● 1400 ℃
□ 1425 ℃
▼ 1450 ℃

(a)

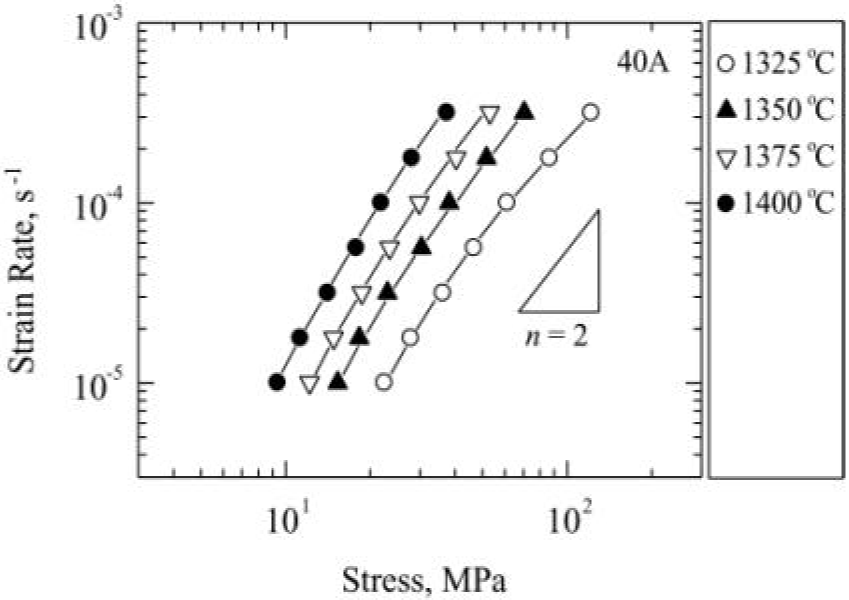
Strain Rate, s^{-1}
Stress, MPa
10^{-3}
10^{-4}
10^{-5}
10^{1}
10^{2}
40A
n = 2
○ 1325 ℃
▲ 1350 ℃
▽ 1375 ℃
● 1400 ℃

(b)

Figure 4.6

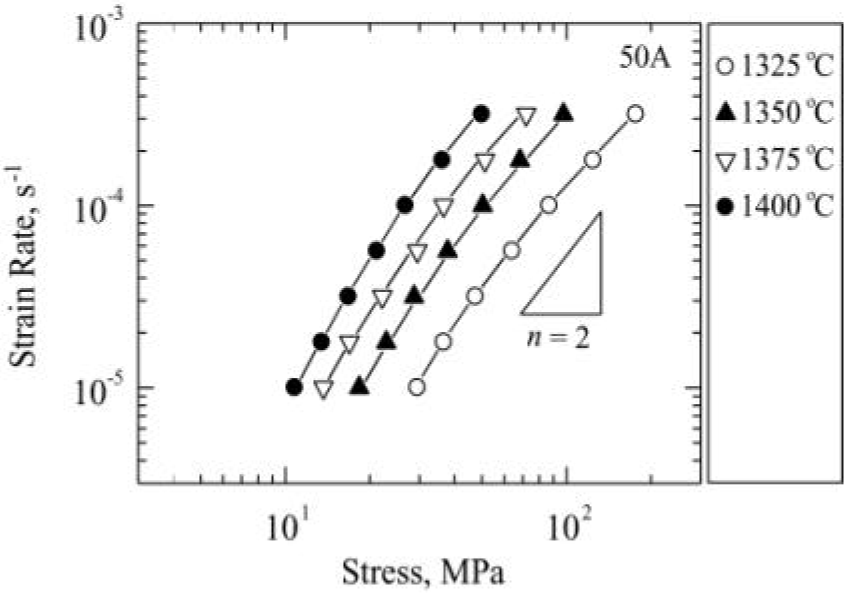

(c)

Figure 4.6 Strain rates as a function of stresses at a temperature range from 1300°C to 1450°C on log-log scales for particulate composites (a) 20A; (b) 40A; (c) 50A.

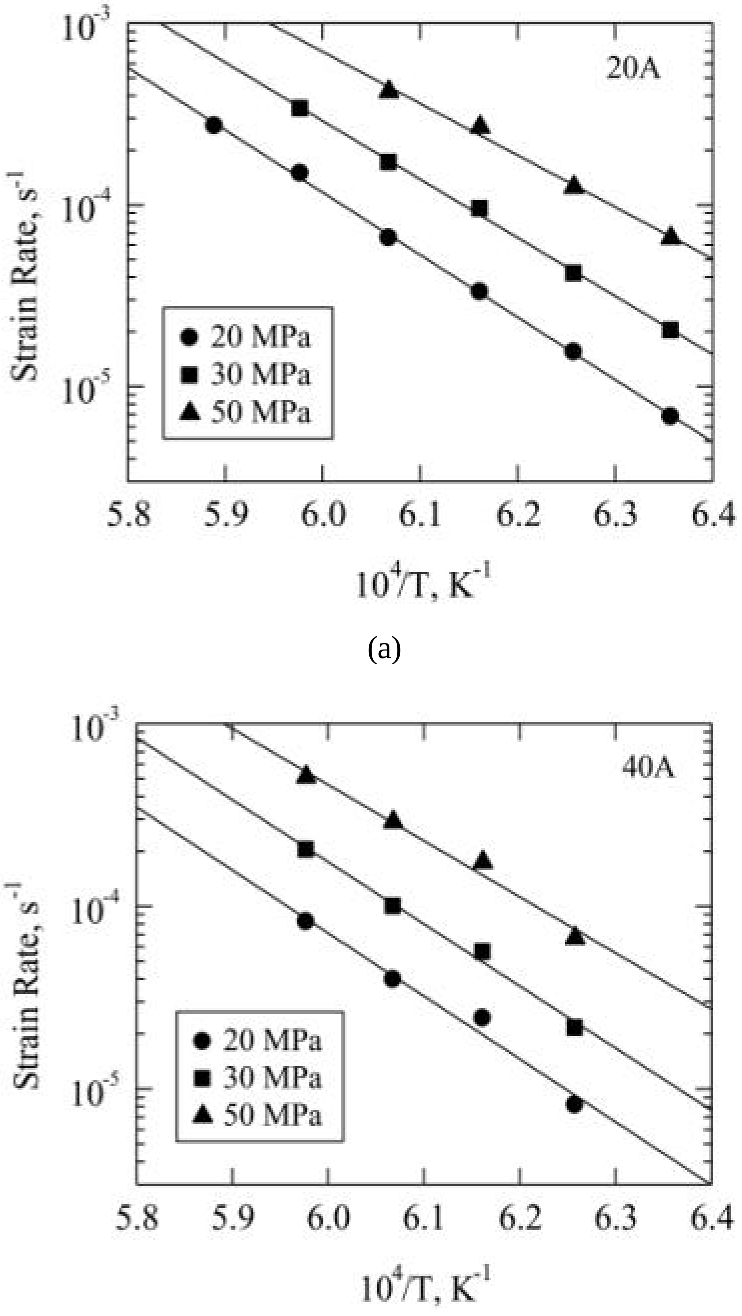
20A
Strain Rate, s⁻¹
10⁻³
10⁻⁴
10⁻⁵
5.8
5.9
6.0
6.1
6.2
6.3
6.4
10⁴/T, K⁻¹
● 20 MPa
■ 30 MPa
▲ 50 MPa
40A
Strain Rate, s⁻¹
10⁻³
10⁻⁴
10⁻⁵
5.8
5.9
6.0
6.1
6.2
6.3
6.4
10⁴/T, K⁻¹
● 20 MPa
■ 30 MPa
▲ 50 MPa

(a)

(b)

Figure 4.7

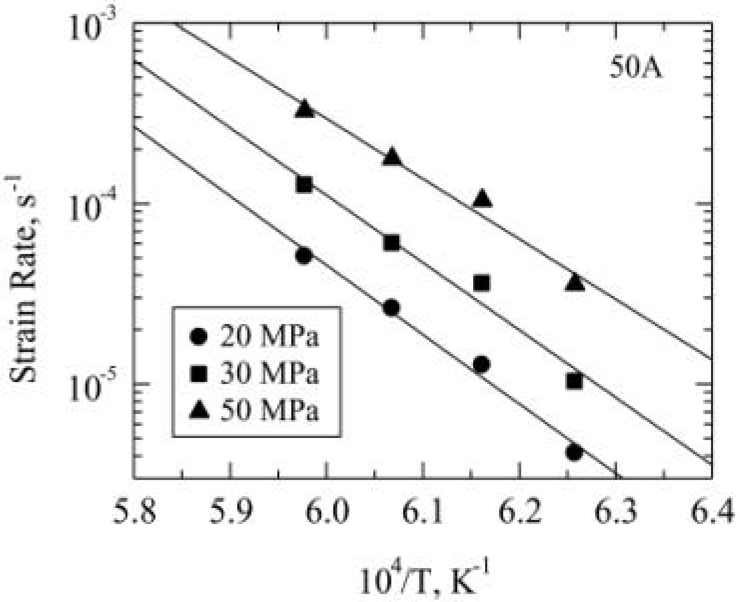

(c)

Figure 4.7 Strain rates on log scale as a function of reciprocal absolute temperature for particulate composites (a) 20A; (b) 40A; (c) 50A.

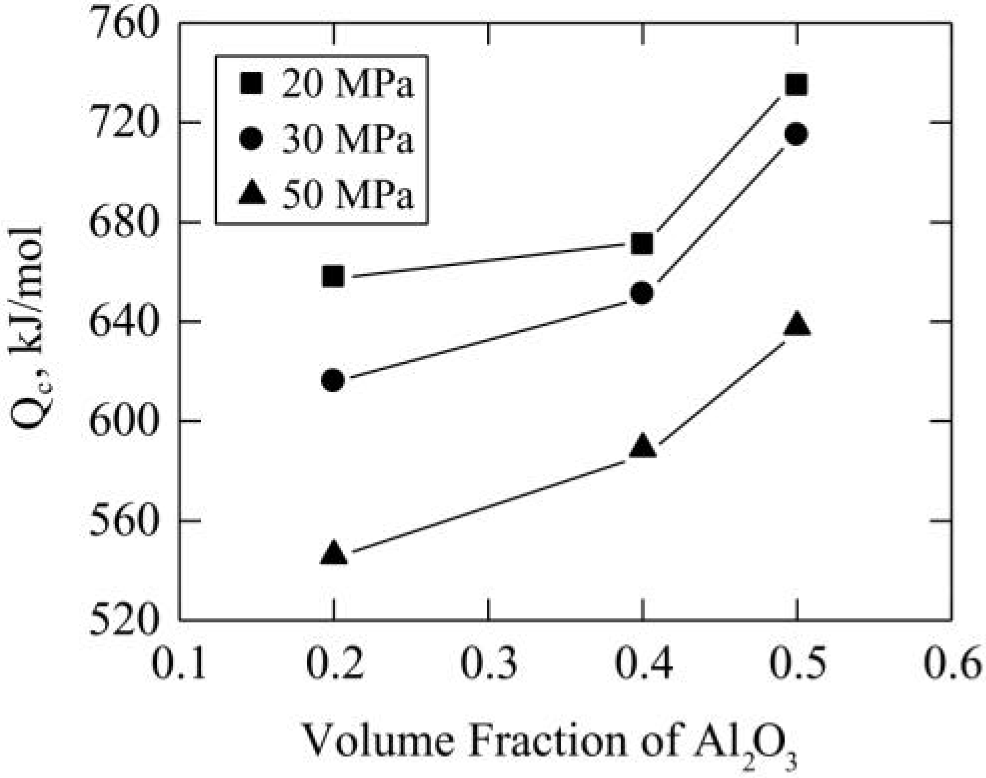

Figure 4.8 The variation of activation energies with stress and the volume fraction of Al_2O_3.

4.3 DISCUSSION

4.3.1 Comparison with Existing Models

French *et al.* proposed that the creep of particulate composites can be analyzed using isostress or isostrain models [106]. The isostress model assumes that the average stress in the composite, s_c, is equal to that in each component of the composite, s_1 and s_2 for a two-component composite, *i.e.* $s_c = s_1 = s_2$. The average strain rate in the composite, $\dot{e}_c$, is given by

$$\dot{e}_c = V_1\dot{e}_1 + V_2\dot{e}_2 \tag{4.2}$$

where V_1 and $\dot{e}_1$ are the volume fraction and strain rate of component one and V_2 and $\dot{e}_2$ are the volume fraction and strain rate of component two. The isostrain model, on the other hand, requires that the strain in each component of the composite equal the average composite strain, *i.e.* $e_c = e_1 = e_2$. Thus, the strain rates must also be equal, *i.e.* $\dot{e}_c = \dot{e}_1 = \dot{e}_2$. The average stress in the composite can be represented for the isostrain case as

$$s_c = V_1 s_1 + V_2 s_2 \tag{4.3}$$

Assuming that each component obeys Equation 4.1, the isostrain model predicts the composite flow stress to be

$$s_c = V_1 K_1 \dot{e}_c^{1/n_1} + V_2 K_2 \dot{e}_c^{1/n_2} \tag{4.4}$$

where $K_i = E_i (A_i)^{1/n_i} (d_i / b_i)^{p_i/n_i} \exp(Q_{ci} / n_i RT)$ for each component i.

A rheological model has also been proposed by Chen and Xue to predict the deformation response of particulate composites when one phase is rigid and the other is deformable [56]. This model has been previously applied to Al_2O_3/Y-TZP and other particulate composites [20,56]. Using the rheological model, the strain rate of the composite is given by

$$\dot{e}_c = (1 - V_2)^{2+n_1/2} a s^{n_1} \tag{4.5}$$

where V_2 is the volume fraction of rigid inclusions, n_1 is the stress exponent of the deformable matrix, and a is a reference strain rate [60]. In the Al_2O_3/Y-TZP system Al_2O_3 has been assumed to be rigid [8].

To determine the applicability of these models to the materials used in this study, experimental data were fit using a non-linear, least-squares method to Equations 4.2, 4.4, and 4.5. For the isostrain model, the fitting parameters were n_1, n_2, K_1, and K_2, where the subscripts 1 and 2 represent Y-TZP and Al_2O_3, respectively. For the isostress model, the fitting parameters were $\dot{e}_1$ and $\dot{e}_2$ and, for the rhelogical model, the fitting parameters were n_1 and a. Since microstructural stability degrades with less than 10 - 20 vol% second phase [102,103], the compositions that were measured for this study were limited to 20 - 80 vol% Al_2O_3. Thus, the curve fits were used both to assess the agreement between the data and models and to extrapolate from the data for comparison with the properties of Al_2O_3 (doped with Y^{3+}) and Y-TZP. A summary of the curve-fitting results at $s = 50$ MPa is presented in Table 4.2.

Table 4.2 Results from nonlinear curve fits at $s = 50$ MPa and T = 1350°C.

Models & Governing Equations	Fit Parameters			
a. Constrained isostrain $\dot{e}_c = s_c^2 (V_1 K_1 + V_2 K_2)^{-2}$	K_1	K_2		
	1634	8422		
b. Isostrain (unconstrained) $s_c = V_1 K_1 \dot{e}_c^{1/n_1} + V_2 K_2 \dot{e}_c^{1/n_2}$	K_1	K_2	n_1	n_2
	3.8×10^{15}	2898	0.25	2.74
c. Rheological $\dot{e}_c = (1 - V_2)^{2+n_1/2} a s^{n_1}$	n_1	a		
	0.087	0.0003		
d. Isostress $\dot{e}_c = (1 - V_2)\dot{e}_1 + V_2 \dot{e}_2$	$\dot{e}_1$	$\dot{e}_2$		
	0.0003	-0.00008		

Subscript 1 - Y-TZP; subscript 2 - Al_2O_3.

Figure 4.9 presents three plots of the logarithm of strain rate against volume fraction of Al_2O_3 at flow stresses of 20, 50, and 70 MPa. Fits of an isostress model, a rheological model, an isostrain model, and a constrained isostrain model, which is discussed in the next section, match the data well within the range of Al_2O_3 compositions (20 - 80 vol%) for which data are available. Extrapolations of the fitted equations beyond the compositions are also examined. When the fitted equations extrapolate to 100% Y-TZP, the creep rates predicted by all the models seem to be physically realistic, which will be discussed further in the next section. When the fitted equations extrapolate to 100% Al_2O_3, the creep rate predicted by the rheological model is zero, and the creep rate extrapolated from the isostress model is negative. Both zero and negative values of creep rate for 100% Al_2O_3 (doped with Y^{3+}) are physically unrealistic. As suggested by Yoon and Chen, the assumption that Al_2O_3 is rigid is likely violated in this system [60]. In contrast, the isostrain model provides a more reasonable prediction of the creep rate of 100% Al_2O_3 than do either the rheological model or the isostress model. However, when the fitting parameters in the isostrain model are left unconstrained, the results given by least-squares fits for these parameters are not satisfying. For example, at $s = 50\ MPa$, using the isostrain model, the best fit value of the stress exponent for Y-TZP is $n_1 = 0.25$ which is significantly less than the experimentally measured values of 2 to 3.

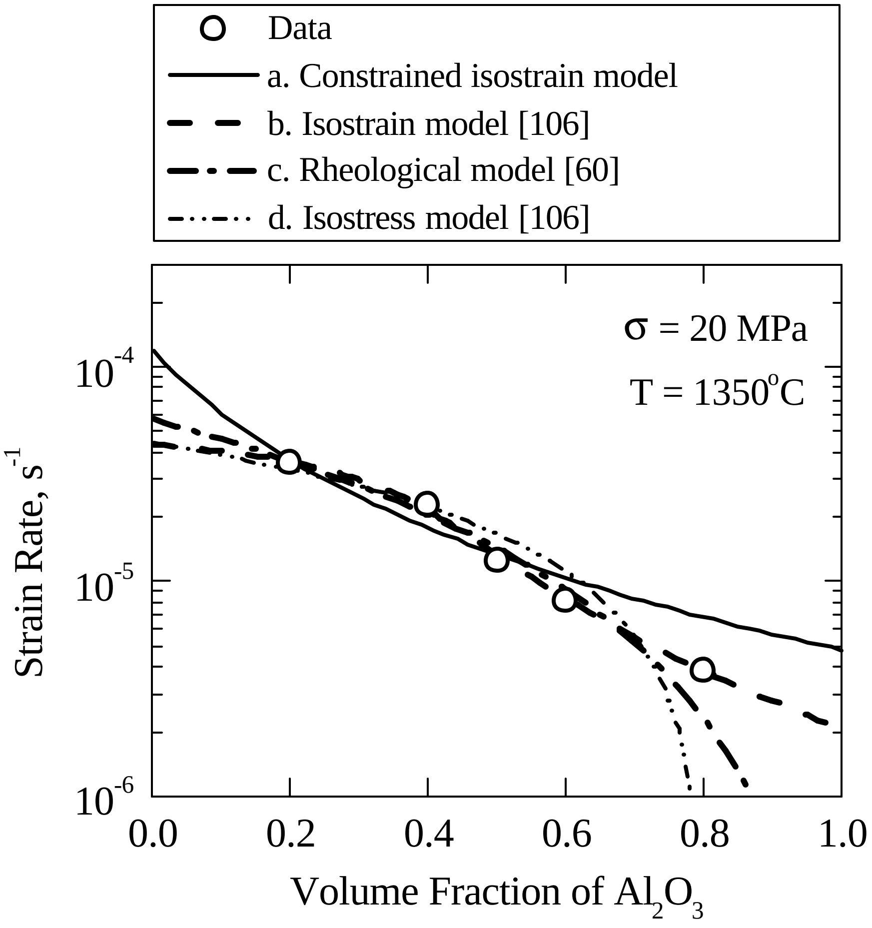

Data
a. Constrained isostrain model
b. Isostrain model [106]
c. Rheological model [60]
d. Isostress model [106]
σ = 20 MPa
T = 1350°C
Strain Rate, s⁻¹
10⁻⁴
10⁻⁵
10⁻⁶
0.0
0.2
0.4
0.6
0.8
1.0
Volume Fraction of Al₂O₃

(a)

Figure 4.9

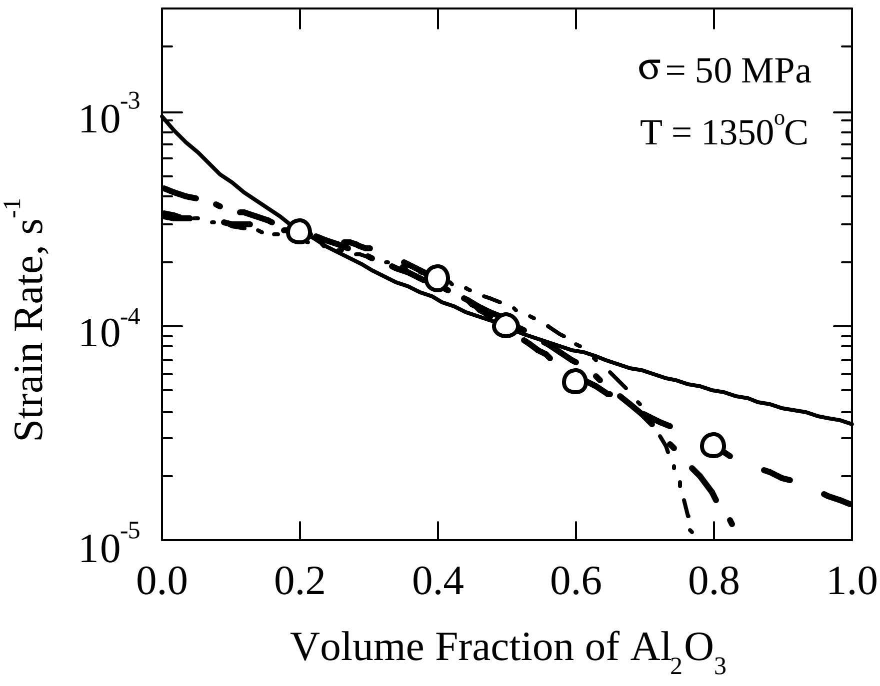

σ = 50 MPa
T = 1350°C
Strain Rate, s^-1
10^-3
10^-4
10^-5
0.0
0.2
0.4
0.6
0.8
1.0
Volume Fraction of Al2O3

(b)

Figure 4.9

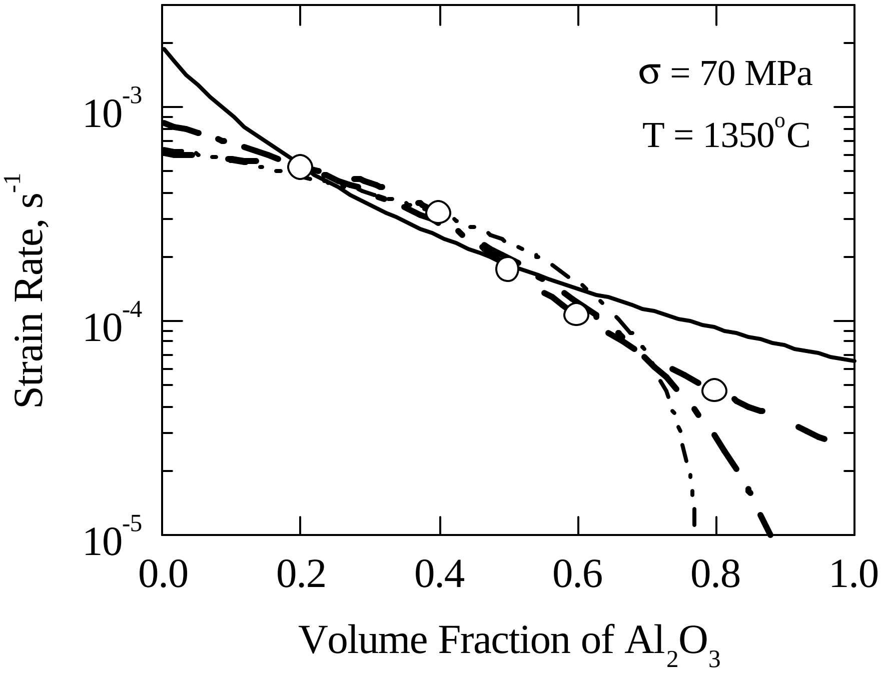

(c)

Figure 4.9 Strain rates on log scale as a function of the volume fraction of Al_2O_3 for Al_2O_3/Y-TZP particulate composites at stresses of (a) 20 *MPa*, (b) 50 *MPa*, and (c) 70 *MPa*.

4.3.2 Constrained Isostrain Model

Good agreement is found between the isostrain model and the available data. To further examine the applicability of the isostrain model, the effects of constraining the stress exponents to realistic values, consistent with those observed experimentally, are investigated. Previous studies indicate that n = 1 - 3 for 3Y-TZP [82,83,92] and values between 1 - 2 have been reported for fine-grained Al_2O_3 [95,107]. By assuming that the stress exponents in each phase are equal (*i.e.* $n = n_1 = n_2$), Equation 4.4 can be simplified and written in terms of the composite strain rate, $\dot{e}_c$,

$$\dot{e}_c = s_c^n \left(V_1 K_1 + V_2 K_2\right)^{-n} \tag{4.6}$$

Equation 4.6 was used to fit the experimental data at stresses of 20, 50, and 70 *MPa* using three integer values for n, *i.e.* $n=1$, $n=2$, and $n=3$ to determine an approximate value of n for the constrained isostrain model. Only integer values of n were selected because integer values of n are predicted from existing theoretical models [30] and because our ability to distinguish to more than one significant digit is limited by the experimental data. Unlike the fits shown in Figure 4.9, where each curve is independently fit at each stress, the constrained isostrain model was required to fit data at all three stresses simultaneously using one set of fit parameters, *i.e.* K_1 and K_2 at a given n. The resulting fits are shown in Figure 4.10. These results suggest that $n = 2$ is a better choice than either $n = 1$ or $n = 3$, and it is also a physically realistic value (see Figure 4.5).

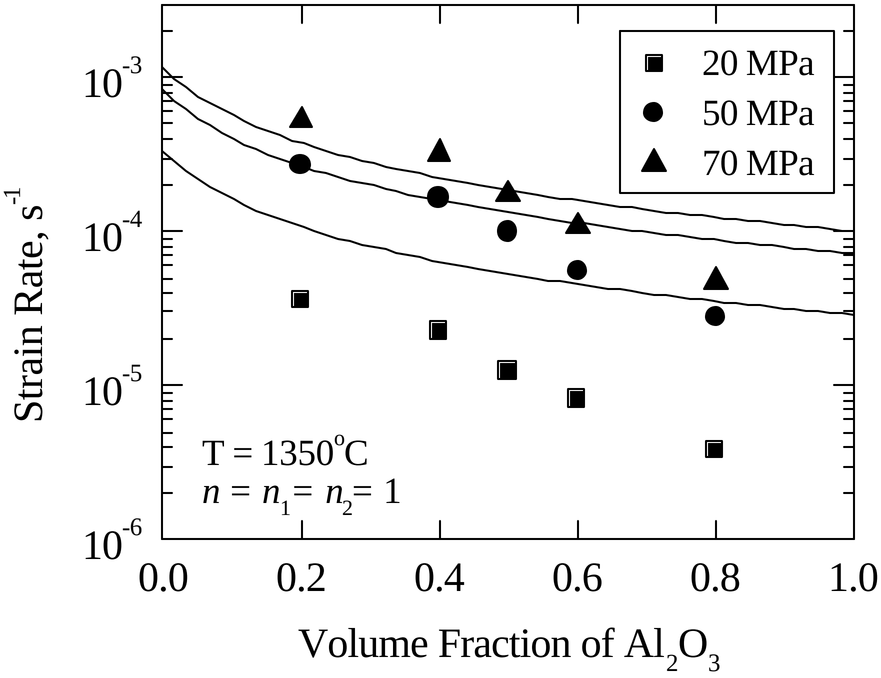

(a)

Figure 4.10

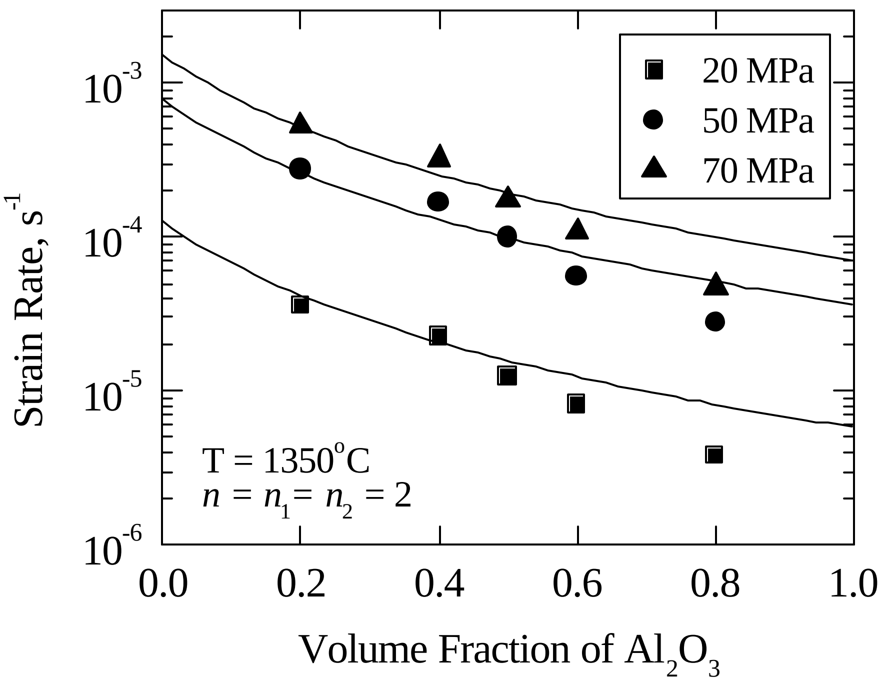

20 MPa
50 MPa
70 MPa
T = 1350°C
n = n1 = n2 = 2
Strain Rate, s-1
10-3
10-4
10-5
10-6
0.0
0.2
0.4
0.6
0.8
1.0
Volume Fraction of Al2O3

(b)

Figure 4.10

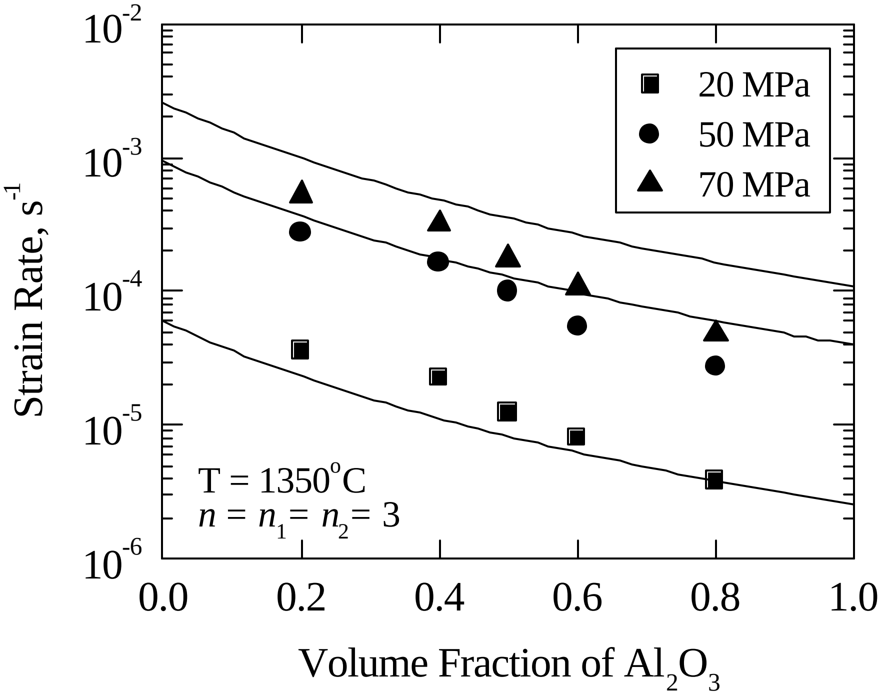

(c)

Figure 4.10 Fits of the constrained isostrain model to experimental data over a wide range of stresses for (a) $n = 1$; (b) $n = 2$; (c) $n = 3$.

Qualitative comparison with the other fitted equations indicates that the constrained isostrain model provides the most satisfying result when one considers the practical significance of the parameters. In Figure 4.9 the fits resulting from the constrained isostrain model (for $n = n_1 = n_2 = 2$) are shown as solid lines. The constrained isostrain model deviates most from the data points of the 60A and 80A. For these materials, the constrained isostrain model predicts a faster creep rate than that experimentally observed, which is the correct deviation when the coarser grain sizes of the 60A and 80A materials, compared with the other particulate composites, are considered.

Predictions of normalized creep rate for pure Y-TZP are shown in Figure 4.11 for the four models considered. In Figure 4.11, creep rate is normalized by the average grain size of pure Y-TZP ($\overline{d}_{Y-TZP} \approx 0.30\, mm$), assuming a grain-size exponent of $p = 2$. Jiménez-Melendo *et al.* [83] summarized all available data on the creep rate of Y-TZP at 1350^{o}C in the same fashion, and the results of their summary are shown in Figure 4.11 as a solid line representing the average of $\dot{e} \cdot d^2$ values they presented and dashed lines representing the approximate scatter in those data. The constrained isostrain model is the closest to the average of the data available from the literature, as is shown in Figure 4.11. Furthermore, the constrained isostrain and the isostrain models provide more reasonable predictions for the creep rate of 100% Al_2O_3 than do the other models. At $s = 50$ *MPa*, the creep rates predicted for 100% Al_2O_3 (doped with Y^{3+}) by the constrained isostrain model and the isostrain model are 3.5×10^{-5} s^{-1} and 1.5×10^{-5} s^{-1}, respectively. Unfortunately, Al_2O_3 cannot retain a fine grain size during creep deformation at 1350°C, and thus no experimental data are available for comparison. Indeed, the ability to predict physically realistic creep rates for compositions that are difficult or impossible to fabricate or test is one of the major advantages of the constrained isostrain model.

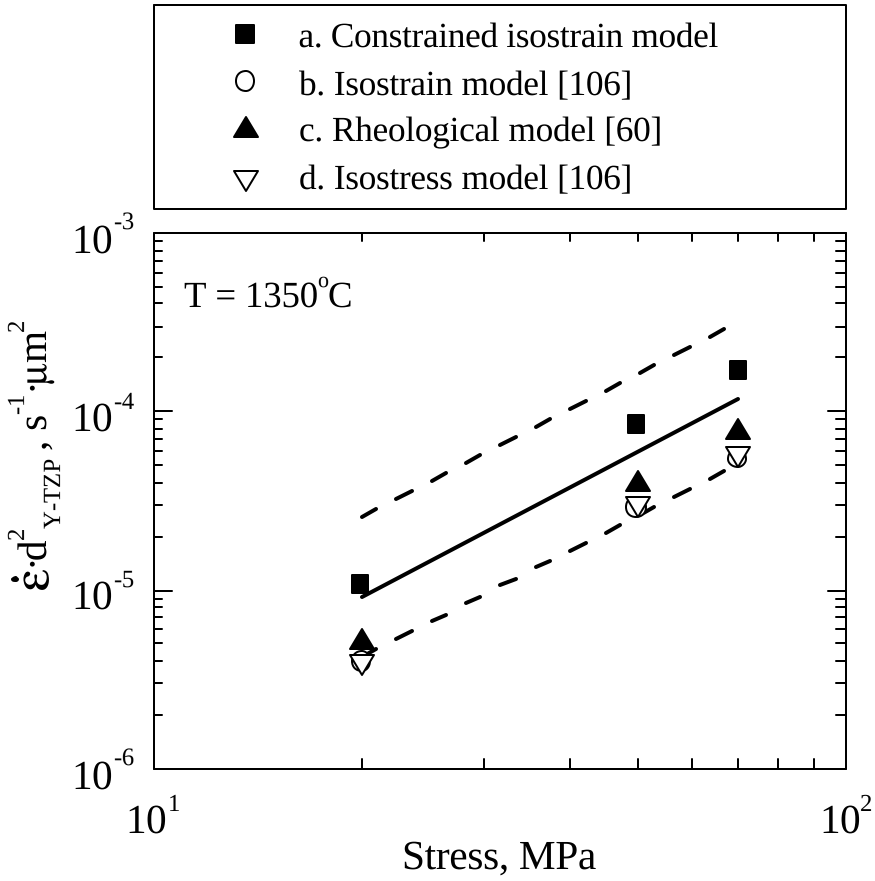

Figure 4.11 Predictions of creep rate for pure Y-TZP for the four models are compared to a fit of all available creep data from pure Y-TZP, as given by Jiménez-Melendo *et al.* (solid line), and the approximate scatter of those data (dashed lines) [83].

4.3.3 Comparison with Previous Studies

All of the data available from the literature for Al_2O_3/Y-TZP particulate composites similar to those of the present investigation were compiled and are listed in Table 4.3. Although the Al_2O_3/Y-TZP particulate composites prepared for this study were processed using techniques different from those of other investigations [8,9,20], the microstructures produced are quite similar, with well-dispersed Al_2O_3 and Y-TZP phases. The grain sizes of the materials in the present study are finer than those of previous investigations by factors of 1.5 and 2 for the Y-TZP and Al_2O_3 phases, respectively [20], after compensation for the methods of grain-size measurement used in each investigation.

For Al_2O_3/Y-TZP composites tested in compression at temperatures of 1400 - 1550^{o}C, a previous study has indicated that the stress exponent increases monotonically with temperature from 1.2 at 1400^{o}C to 1.9 at 1550^{o}C [9]. In contrast, subsequent studies on similar materials conducted in tension [11] and compression [65] consistently indicated much higher stress exponents of between 2 and 3 at temperatures from 1250^{o}C to 1650^{o}C, as shown in Table 4.3. In the current study, stress exponents are approximately 2 at high Al_2O_3 content and high stresses and approximately 3 at low Al_2O_3 content and low stresses (see Figure 4.5). The discrepancy between the current results and a previous study that reported stress exponents of less than 1.5 in compression may result from the relatively high values and narrow range of strain rates at which those tests were conducted, as shown in Table 4.3. Data from the present investigation also suggest that a transition occurs to lower values of stress exponent as strain rate increases, which is consistent with previous studies [107,108].

Table 4.3 Creep behaviors of Al_2O_3/Y-TZP particulate composites, as given in the literature.

Materials [a]	Grain Size (*mm*)		T (^{o}C)	$\dot{e}$ (s^{-1})	Test [b]	*n*
	Y-TZP	Al_2O_3				
27.3A [9]	0.90	0.80	1400-1550	10^{-4}-2×10^{-3}	C	1.2-1.9
27.3A [65]	0.70	0.70	1292	10^{-8}-10^{-3}	C	2.8
					T	2.8
27.3A [11]	0.50	0.50	1450-1650	8×10^{-5}-5×10^{-3}	T	2.0-3.0
27.3A [8]	0.50	0.50	1250-1450	10^{-7}-10^{-2}	T	2.0-2.2
50.0A [20]	0.51	0.61	1250-1450	10^{-7}-10^{-2}	T	2.1-2.4
69.2A [20]	0.59	0.99	1250-1450	10^{-7}-10^{-2}	T	1.9-2.4
85.7A [20]	0.47	1.00	1250-1450	10^{-7}-10^{-2}	T	1.7-2.1

[a] Compositions were designated by the volume faction of Al_2O_3;

[b] C = Compression; T = Tension.

In addition, the current study on samples tested in compression indicated that the activation energies of Al_2O_3/Y-TZP particulate composites, 20A, 40A, and 50A, varied from 660 kJ/mol to 740 kJ/mol at a flow stress of 20 *MPa*, and increased with the volume fraction of Al_2O_3. These values are consistent with previous studies on samples tested in tension by Wakai *et al.* [20]. During the high-temperature deformation of Al_2O_3/Y-TZP composites, O^{2-} diffuses much more rapidly than the cations and creep is therefore controlled by the diffusion of the slower-moving Zr^{4+} ion in the lattice or along the grain boundaries [109]. At present, there are no cation diffusion data for tetragonal Y-TZP, but data are available for the diffusion of Zr^{4+} in cubic zirconia. Oishi *et al.* reported the activation energies were 293 kJ/mol and 423 kJ/mol for grain boundary and lattice diffusion of Zr^{4+} ions in 16 mol% Y_2O_3-stabilized cubic ZrO_2 polycrystal, respectively [110]. Chien and Heuer deduced $Q_c = 511$ kJ/mol for the lattice diffusion of Zr^{4+} in 9.4 mol% Y_2O_3-stabilized ZrO_2 single crystal [111]. Lakki *et al.* determined $Q_c = 460$ kJ/mol for the lattice diffusion of Zr^{4+} in 8 mol% Y_2O_3-stabilized ZrO_2 polycrystal [112]. Apparently, the measured Q_c values are closer to the values for lattice diffusion than that for grain boundary diffusion of Zr^{4+}. However, the uncertainty in the diffusion data for lattice and boundary diffusion of Zr^{4+} and the possibility of interface-controlled creep [56] prelude a definitive interpretation of the activation energy. Comparing with non-doped Al_2O_3 [107,113] and pure Y-TZP [83,114], where most of activation energies range between 450 - 600 kJ/mol, a higher activation energy for high-temperature deformation of Al_2O_3/Y-TZP has been attributed to the segregation of Zr^{4+} at the Al_2O_3 grain boundaries resulting in a decrease of the diffusivity of Al^{3+}, limited by the interface-reaction [56,79,115-117].

To examine the influence of volume fraction of Al_2O_3 on deformation behavior, the constrained isostrain model was used to analyze all currently available data. The data were normalized to a 50A composition by plotting

$\dot{e}_c\left(\frac{V_1K_1+V_2K_2}{0.5K_1+0.5K_2}\right)^2$ versus stress on dual-logarithmic scales, as is shown in Figure 4.12a. By plotting the data in this manner, the data from 20A, 40A and 50A with similar grain sizes ($\bar{d}_{Al_2O_3} \approx 0.38\, mm,\ \bar{d}_{Y-TZP} \approx 0.30\, mm$) fall onto a single curve with a slope of 2, which is labeled in Figure 4.12a as “fine grains”. Wakai *et al.* have studied the Al_2O_3/Y-TZP composite system using samples with a slightly larger grain size than in the present study [8,20]. They tested these materials at 1350ºC in tension. Their data from materials with 27.3 vol% and 50 vol% Al_2O_3 (labeled as 27.3AW and 50AW, both of which have similar grain sizes ($\bar{d}_{Al_2O_3} \approx 0.55\, mm,\ \bar{d}_{Y-TZP} \approx 0.50\, mm$), are also shown in Figure 4.12a. These data are fit with a line of slope 2, which is shown in Figure 4.12a with the label “coarse grains”. The constrained isostrain model is used to successfully collapse the data from particulate composites with different compositions, but similar grain sizes, onto a single curve. The differences in grain sizes result in a difference in flow stress. The 60A and 80A materials have Al_2O_3 grain sizes which are intermediate between those of the materials with data along the “fine grains” and “coarse grains” lines in Figure 4.12a. Data from 60A and 80A materials should, thus, lie between those of the “fine grains” and “coarse grains” lines, which are shown to indeed be the case in Figure 4.12b. The observed grain size dependence, composition dependence, and similarities in stress exponent and activation energy between the data obtained in compression for the current study and previous data obtained in tension suggest that the same deformation mechanisms are dominant in compression and tension.

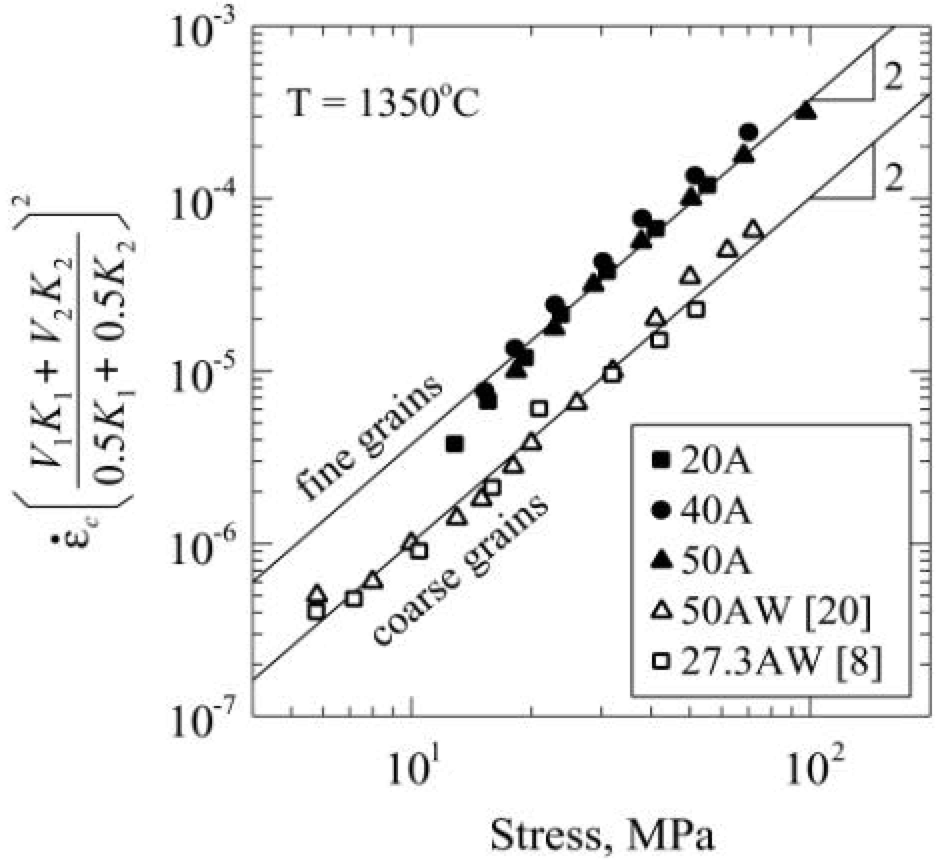

(a)

Figure 4.12

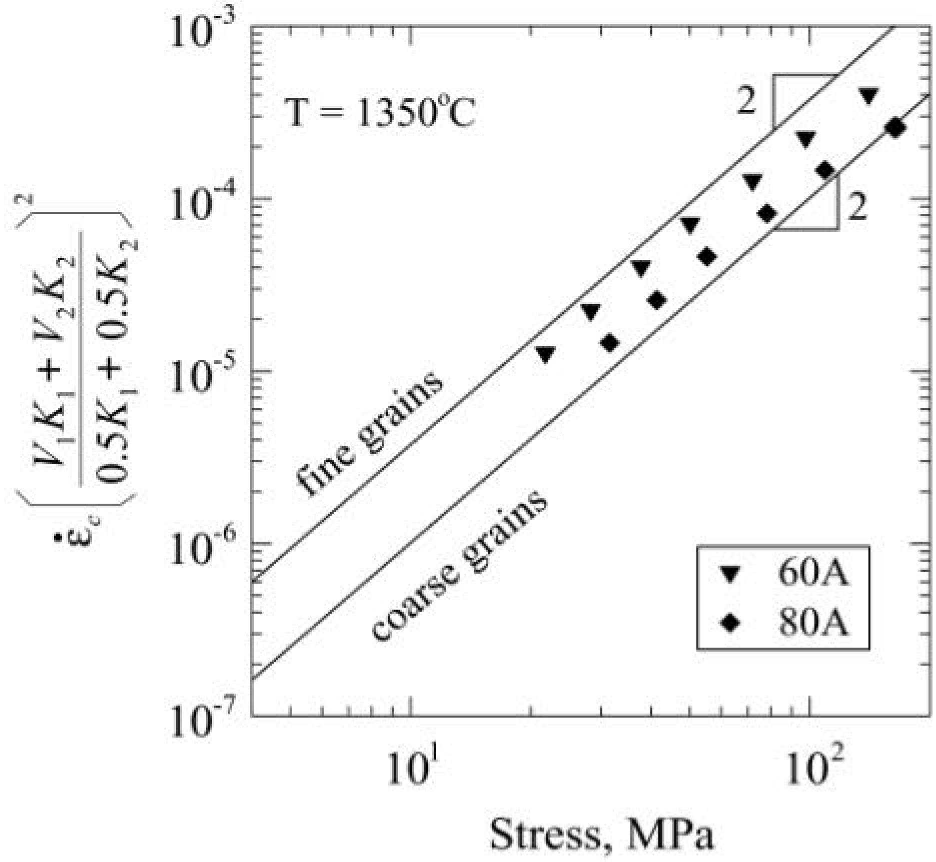

(b)

Figure 4.12 The logarithm of strain rate, normalized to a 50 vol% Al_2O_3 composition by the constrained isostrain model, versus the logarithm of flow stress for composites with (a) less than 50 vol% Al_2O_3 and (b) greater than 50 vol% Al_2O_3. The fit lines have a slope of 2.

4.4 CONCLUSIONS

The deformation behaviors of Al_2O_3/Y-TZP particulate composites have been systematically studied under conditions for which changes in microstructure during testing have been deliberately minimized. The results of these tests suggested that stress exponents were approximately 2 at high Al_2O_3 contents and high stresses and approximately 3 at low Al_2O_3 contents and low stresses. There is little difference in deformation mechanism between Al_2O_3/Y-TZP particulate composites tested in the current study in compression and those tested previously in tension. Good qualitative agreement between the experimental data and a constrained isostrain model, for which the stress exponents of the constituent Al_2O_3 and Y-TZP phases were constrained to physically realistic values, was observed. This model successfully predicts the difference in flow stress and strain rates with different compositions, but similar grain size. In addition, no experimental evidence was found to indicate the existence of glassy phase in the Al_2O_3/Y-TZP particulate composites.

Chapter 5

High-Temperature Deformation of Al_2O_3/Y-TZP Particulate Laminates in Compression

5.1 INTRODUCTION

In the past decade, laminated composites have emerged as promising candidates for use in structural applications [118-121]. By controlling the microstructure, the properties of laminated composites can be tailored to be superior to their monolithic counterparts [122,123]. So far, a number of studies have been conducted to explore mechanical properties of laminated composites [124]. For example, enhanced fracture toughness was observed in Al_2O_3/Ce-TZP laminates [118]. The deformation behaviors of laminated metal composites have also been explored, including a TiAl laminar alloy [125] and a ferrous laminar composite [126]; yet, few attempts have been made to study the creep of laminated ceramic composites. Recently, Jiménez-Melendo *et al*. [127,128] have studied the high-temperature behaviors of Al_2O_3/85 vol% Al_2O_3 + 15 vol% 3Y-TZP and 3Y-TZP/60 vol% Al_2O_3 + 40 vol% 3Y-TZP hybrid laminate composites, where one layer was monolithic, the other was composite. They reported that the behavior of the laminates was influenced by the layer interfaces [129].

Previously, the high-temperature deformation of Al_2O_3/Y-TZP particulate composites have been extensively studied [8,11,20,21]. In the present work, Al_2O_3/Y-TZP particulate composites with different compositions are used as starting materials to build up a novel layered architecture, *i.e.* particulate laminates, where two compositing schemes are chosen to minimize microstructural change in both layers. The main objective of this work is to study the high-temperature behaviors of Al_2O_3/Y-TZP particulate laminates in compression as function of phase assemblage, specimen orientation, and layer thickness ratios. The data obtained for particulate laminates are compared to existing theoretical models and to data for particulate composites.

5.2 EXPERIMENTAL RESULTS

5.2.1 Microstructure

As discussed before, particulate composites showed a fine-equiaxed microstructure. An example of the microstructure of a typical particulate composite, prior to testing, is shown in Figure 5.1a. The grains with the lighter contrast are Y-TZP and the grains with the darker contrast are Al_2O_3. A SEM micrograph of a representative 20A/60A (1:1) particulate laminate after compression SRC testing is shown in Figure 5.1b, where the darker layers contain more alumina. An optical micrograph of this 20A/60A (1:1) laminates before testing is shown in Figure 5.1c, where the layers with the lighter contrast are 60A.

As can be seen, the interfaces between the layers of particulate composites with different compositions are straight and remain bonded during testing. Previously we have shown that within the test temperature and range of strain rates used in the current study, no statistically significant changes in grain size and grain shape occurred during the compression SRC testing for particulate composites with compositions ranging from 20 to 80 vol% Al_2O_3. Comparing the microstructures, there also does not appear to be any change in grain size or shape during the SRC testing for particulate laminates.

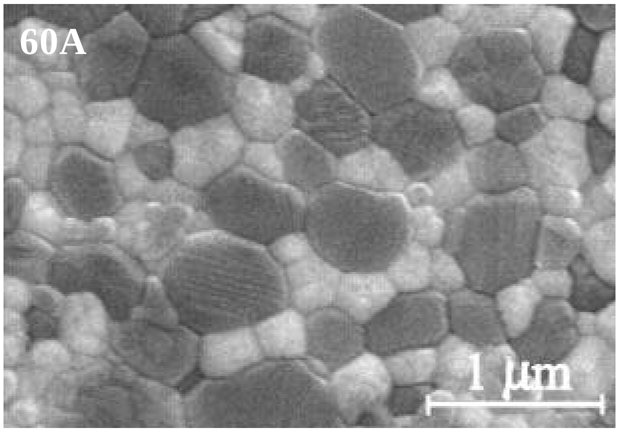

(a)

Figure 5.1

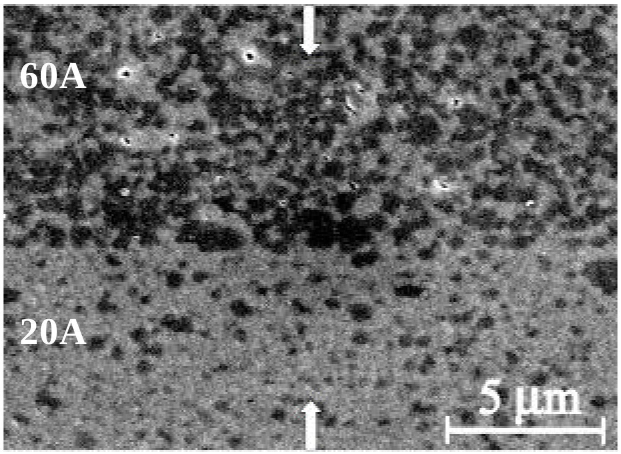

(b)

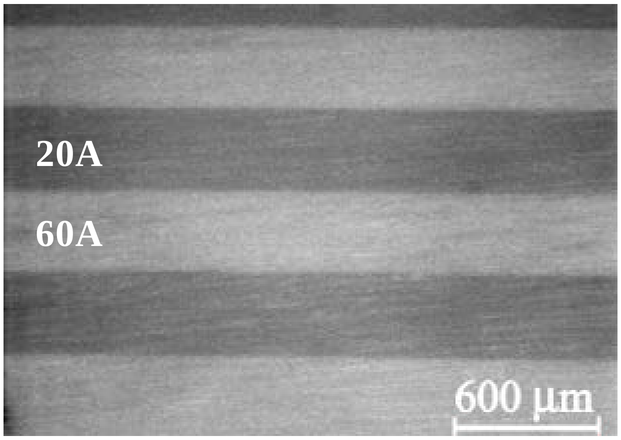

(c)

Figure 5.1 Scanning electron micrographs: (a) 60A before testing; (b) 20A/60A (1:1) after testing at 1350^{o}C. Optical micrograph: (c) 20A/60A (1:1) before testing. The arrows indicate the orientation of applied stress.

The relative densities of selected laminates are shown in Table 5.1 before and after compression SRC testing at 1350°C. The densities prior to testing range from 95% - 99%. The highest densities are obtained in materials where the composition difference between the layers is small (*e.g.* 20A/40A and 40A/60A). These results are consistent with previous studies on similar Al_2O_3/Y-TZP hybrid laminates where it was found that large composition variations resulted in differential sintering rates between the layers, which inhibited the sintering [104]. Comparing the densities before and after testing, a slight increase in density is observed (≤ 1%).

Table 5.1 Relative densities of Al_2O_3/Y-TZP particulate laminates before and after SRC testing at 1350°C (in the isostrain orientation).

Laminates	Relative Densities (%)							
	2:1		1:1		1:2		1:4	
	before	after	before	after	before	after	before	after
20A/40A	98.9	99.1	99.1	99.1	98.4	99.2		
20A/50A	97.6	98.5	97.9	98.9	99.1	99.4		
20A/60A	97.3	98.0	97.3	98.3	98.6	99.0	97.3	97.8
20A/80A			95.8	96.4	95.9	96.6		
40A/60A			98.4	99.2	97.1	98.1		

5.2.2 Deformation Behavior

Figure 5.2 shows a representative compression strain-rate-change (SRC) test for the 20A/40A (1:2) specimen tested in the isostress orientation at 1350°C. The total true strain for this test is $e = 0.115$. After a brief transient at every rate change, a reasonably steady-state stress is achieved. It is also apparent that for the repeated steps at a strain rate of 1.00 × 10^{-4} s^{-1}, the flow stress at a given rate is nearly constant over the range of strains imposed in any single SRC test. Behaviors similar to those shown in Figure 5.2 were observed for all the particulate laminates tested.

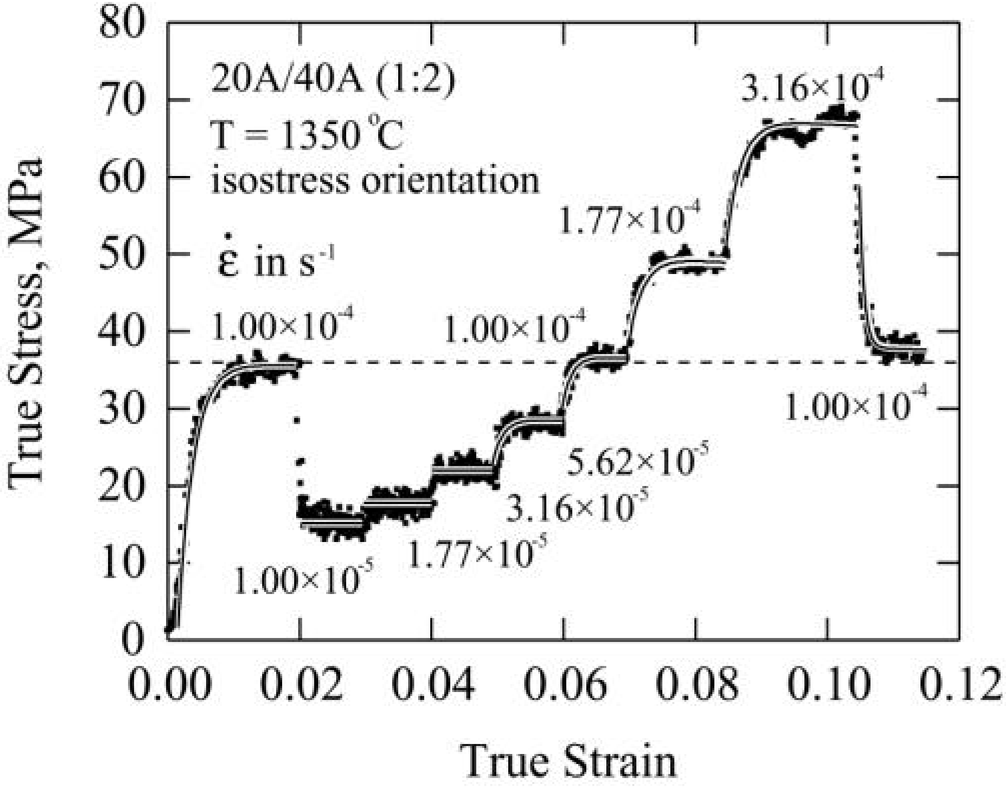

Figure 5.2 A plot of true stress versus true strain for a 20A/40A (1:2) specimen in the isostress orientation during a representative SRC test. The dashed line indicates the average flow stress at a strain rate of 1.00 × 10^{-4} s^{-1}.

Previously, it has been shown that for Al_2O_3/Y-TZP particulate composites, resistance to deformation increases with Al_2O_3 content and grain size [20,130]. In Figure 5.3, the behaviors of particulate composites and laminates are compared for materials with similar grain sizes. Also shown are trend lines for the particulate composites (solid line) and laminates (dashed line). It is apparent that for the same overall composition, the laminates tend to be more resistant to deformation. The difference between the deformation rates of the particulate composites and laminates is most apparent when the composition difference between the layers is large (*e.g.* 20A/80A). This phenomenon can be attributed to the influence of layer constraint imposed by the hard layer on the soft layer during the deformation of particulate laminates. The layer constraint is large when the composition difference between the layers is large.

To further explore the influence of the layer constraint on the deformation, in Figure 5.4 strain rate is plotted against flow stress on log-log scales for three materials that have the same overall composition of 50 vol% Al_2O_3. A comparison between the 50A particulate composite and 40A/60A (1:1) particulate laminate indicates that they have similar flow stresses at a given strain rate. In contrast, the 20A/80A (1:1) particulate laminate is considerably more resistant to deformation due to constraint.

The stress exponent can also be assessed from Figure 5.4. For all these materials the stress exponents were approximately equal to 2. A slight negative curvature is apparent in all of the data, indicating a decrease in stress exponent with increasing stress. Similar behavior was observed for all the laminates tested and has also been observed previously in Al_2O_3/Y-TZP particulate composites (see Chapter 4).

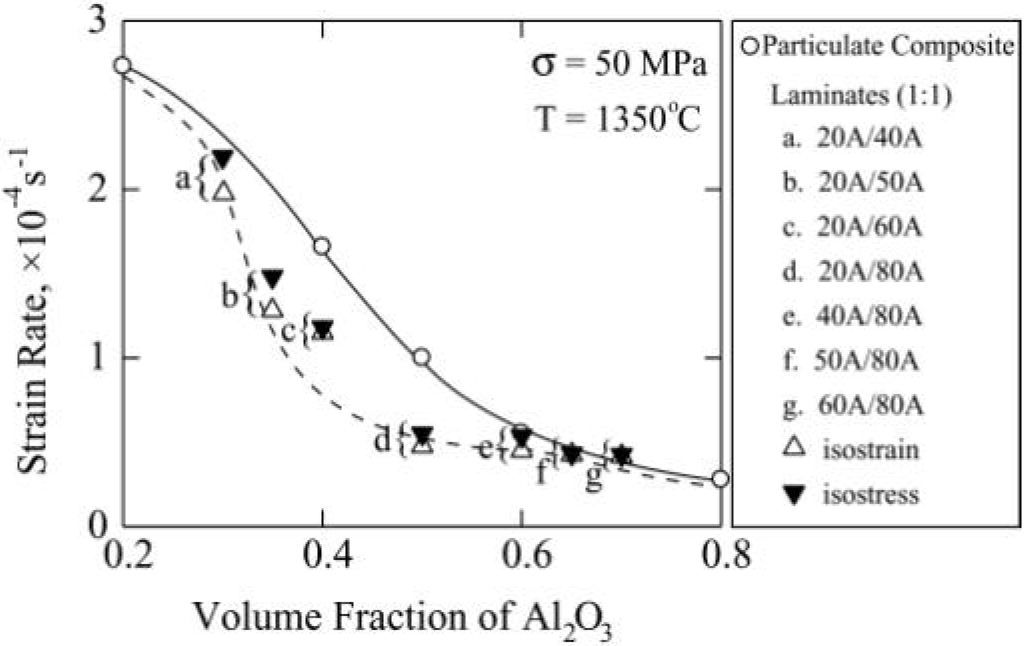

Figure 5.3 The dependence of strain rate on the volume fraction of Al_2O_3. The solid line indicates the trend for monolithic particulate composites and the dashed line indicates the trend for particulate laminates.

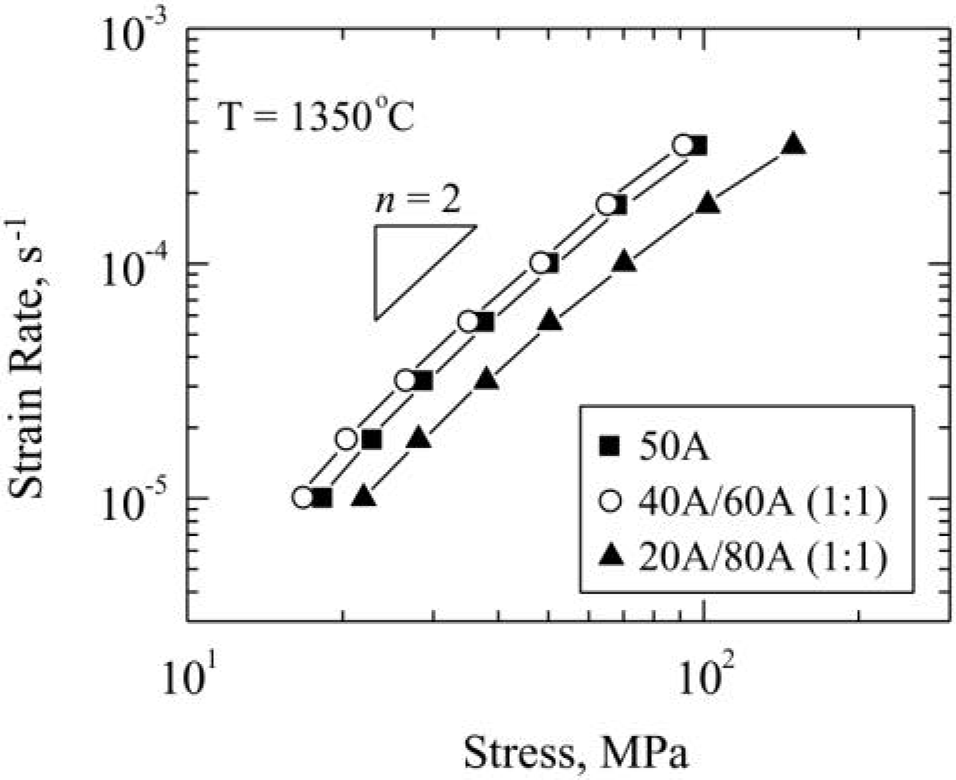

Figure 5.4 Strain rate versus stress on dual-logarithmic scales for 50A particulate composite, 20A/80A (1:1), 40A/60A (1:1) particulate laminates in the isostress orientation. All three materials have an overall composition of 50 vol% Al_2O_3.

In Figure 5.5, the influence of the layer composition on the deformation is studied systematically by varying the composition of only one of the layers. In Figure 5.5a, the composition of the hard layer (*e.g.* 80A) is fixed and the composition of the soft layer is varied. As the fraction of Al_2O_3 in the soft layer is increased, the resistance to deformation increases only slightly. In Figure 5.5b, the composition of the soft layer (*e.g.* 20A) is fixed and the composition of the hard layer is varied. In this case, the resistance to deformation increases markedly as the volume fraction of Al_2O_3 in the hard layer is increased. These results show that composition of the hard layer plays a larger role in determining the deformation response of the laminates than does the composition of the soft layer.

Strain rate is plotted versus flow stress on log-log scales in Figure 5.6 for 20A/60A laminates with different layer thickness ratios. Comparing laminates in which the layer thickness ratios are equal or the thicker layer contains more Al_2O_3 (*i.e.* 1:1, 1:2, and 1:4), it can be seen that there is little effect of layer thickness ratios on flow stress. However, when the thicker layer contains more Y-TZP (*i.e.* 4:1) the resistance to deformation decreases markedly. This suggests that the influence of the hard layer is significant even when the thickness of hard layer is relatively small.

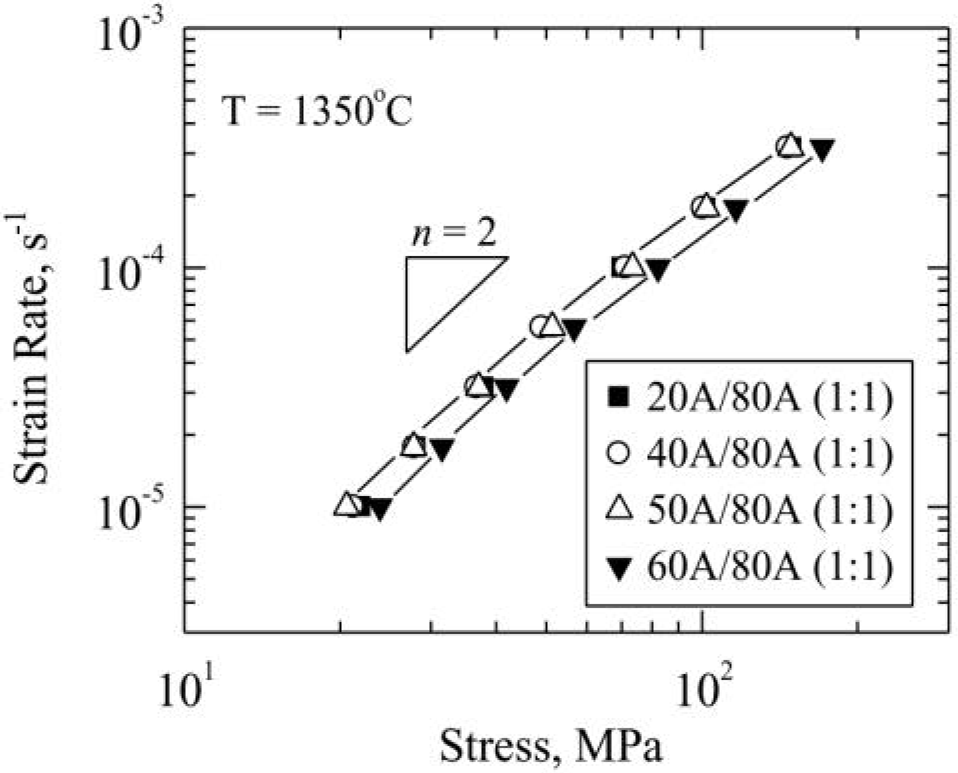
T = 1350°C
n = 2
Strain Rate, s⁻¹
Stress, MPa
10⁻³
10⁻⁴
10⁻⁵
10¹
10²
■ 20A/80A (1:1)
○ 40A/80A (1:1)
△ 50A/80A (1:1)
▼ 60A/80A (1:1)

(a)

Figure 5.5

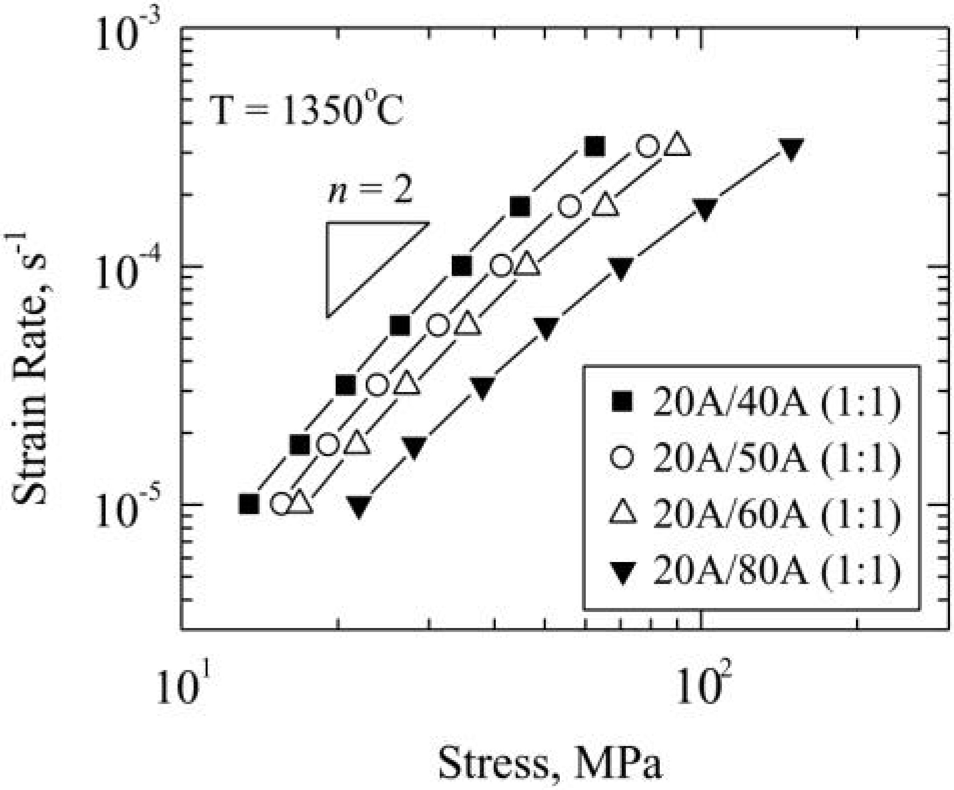

(b)

Figure 5.5 Influence of layer composition on deformation response in the isostress orientation, where (a) composition of the hard layer is held constant and the composition of the soft layer is varied and (b) composition of the soft layer is held constant and the composition of the hard layer is varied.

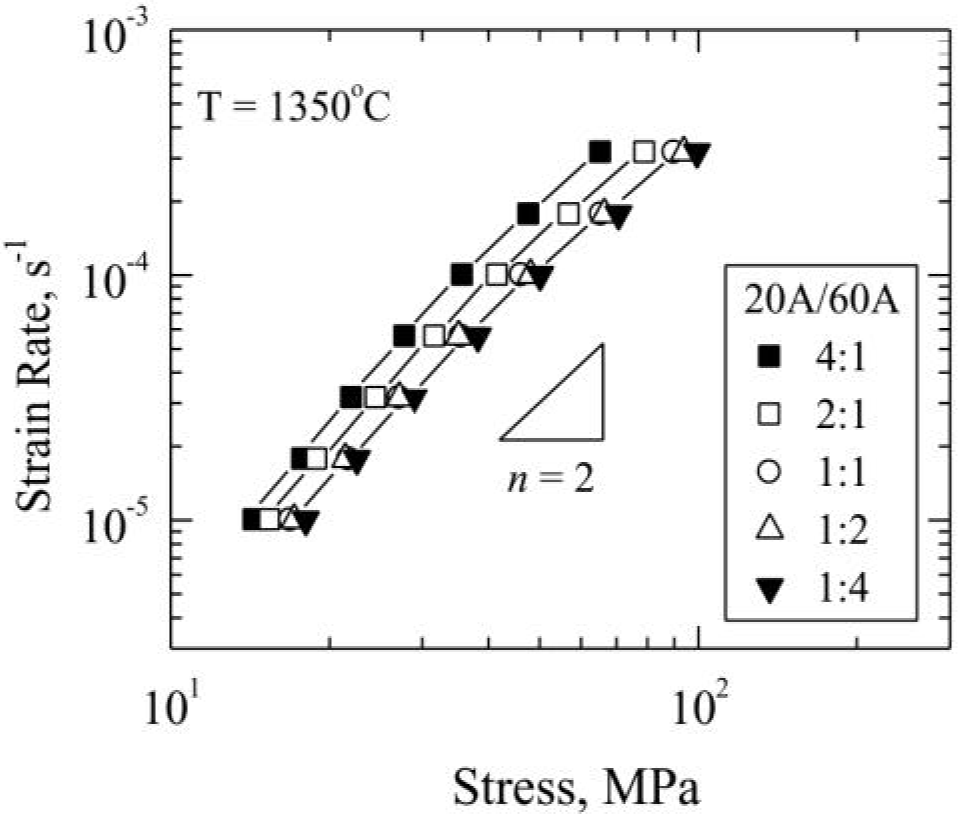

Figure 5.6 Influence of layer thickness ratios on the deformation response of 20A/60A particulate laminates in the isostress orientation.

Figure 5.7 shows the influence of orientation of the applied load on the deformation of particulate laminates. For a large range of compositions, laminates tested in the isostress and isostrain orientations show similar behaviors, but samples tested in the isostrain orientation show slightly greater resistance to deformation. The difference between the two orientations increases with an increasing strain rate, which is in agreement with the observation of Jiménez-Melendo *et al.* [128].

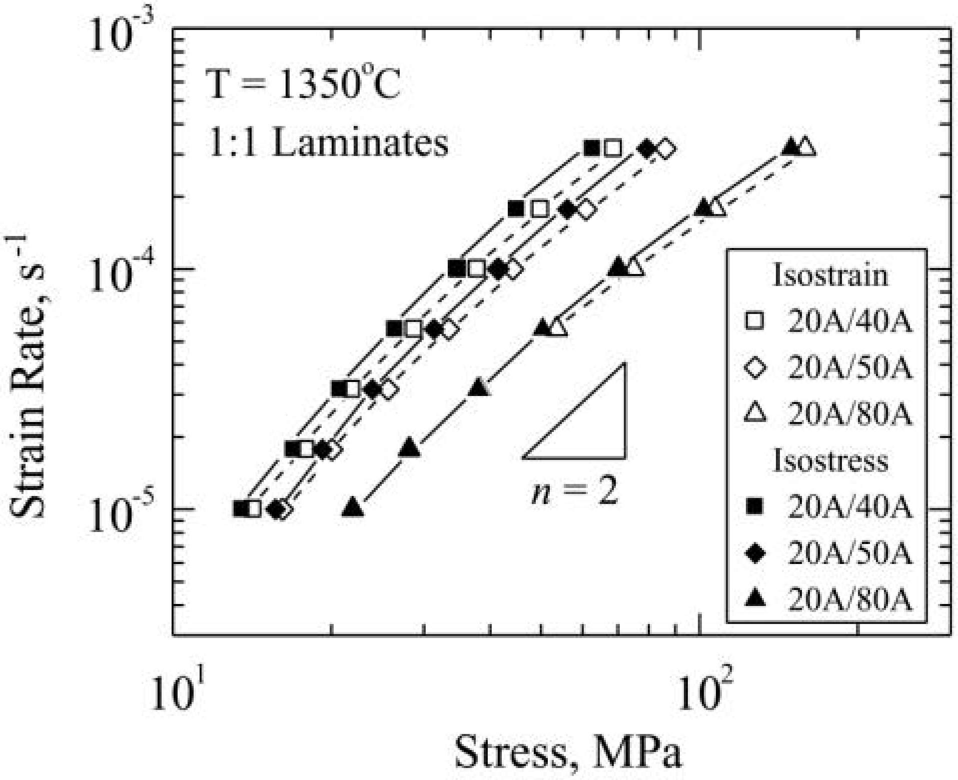

Figure 5.7 Influence of the orientation of the applied stress on the deformation of particulate laminates.

In Figure 5.8, the strain rate is plotted as function of stress for 20A/50A (1:1) laminates in the isostress orientation over a temperature range from 1325^{o}C to 1400^{o}C. The stress exponents calculated vary from approximate 2 to 3. The negative curvature indicates a decrease in stress exponent with increasing stress for a given temperature.

Figure 5.9 shows the temperature dependence of strain rate for 20A/50A (1:1) particulate laminates in the isostress orientation. Since high-temperature deformation follows an Arrhenius relationship $\dot{e} \propto \exp(-Q_c/RT)$, the activation energies were calculated from the slope of the lines in Figure 5.9, yielding the values of 710, 680, and 610 kJ/mol for 20 *MPa*, 30 *MPa*, and 50 *MPa*. It can be seen that the activation energies decrease with increasing stress. Similar results have been also found in the particulate composites (See Chapter 4). Figure 5.10 shows the temperature dependence of strain rate for 20A/50A (2:1) particulate laminates in the isostress and isostrain orientation. The activation energies of Al_2O_3/Y-TZP particulate laminates in the isostrain orientation are slightly higher than that in the isostress orientation, as shown in Figure 5.11, with a maximum difference of less than 70 kJ/mol. Although the limited accuracy resulting from the narrow temperature range precludes a definitive conclusion, there does not appear to be a statistically significant influence of orientation on the activation energies. Figure 5.12 shows that the activation energies of Al_2O_3/Y-TZP particulate laminates range between the two constituent particulate composites.

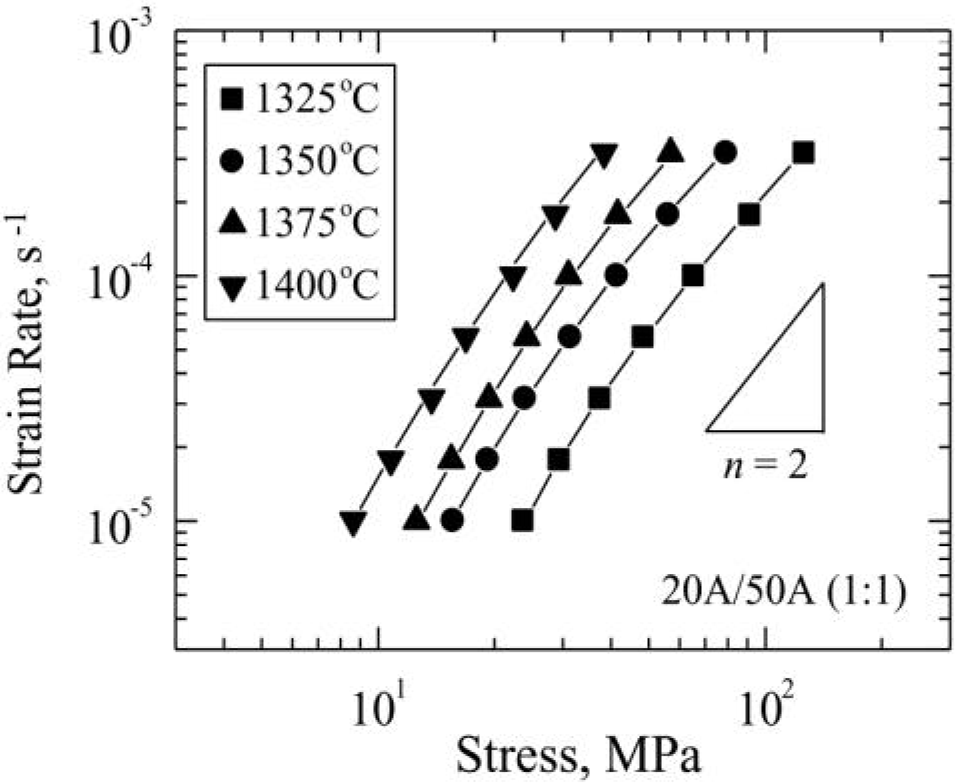

Figure 5.8 Strain rate versus stress on dual-logarithmic scales for 20A/50A (1:1) laminates in the isostress orientation over a temperature range from 1325°C to 1400°C.

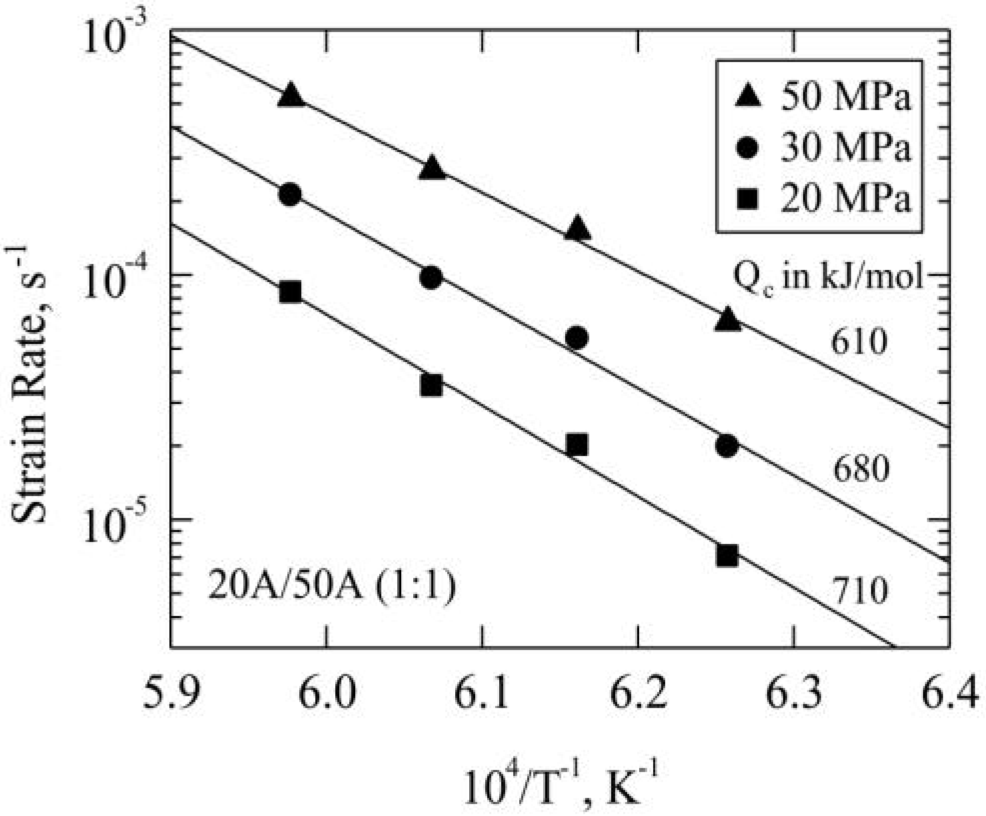

Figure 5.9 The temperature dependence of strain rate for 20A/50A (1:1) particulate laminates in the isostress orientation at 20 *MPa*, 30 *MPa*, and 50 *MPa*.

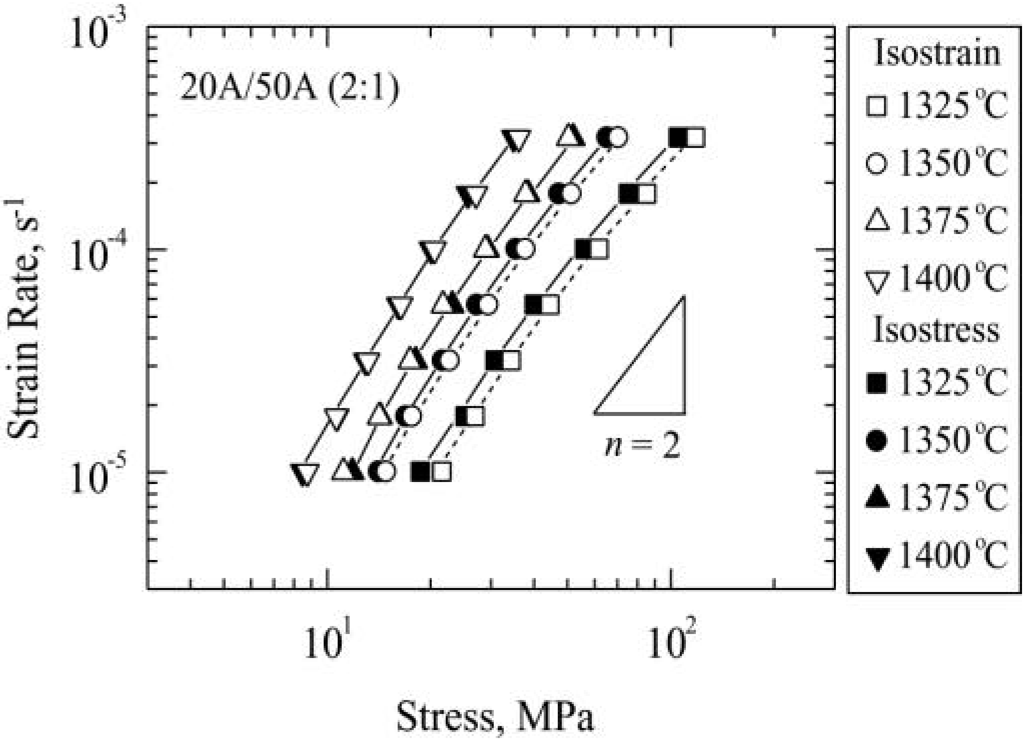

Figure 5.10 Strain rate versus stress for 20A/50A (2:1) particulate laminates in the isostress and isostrain orientation over a temperature range from 1325^{o}C to 1400^{o}C.

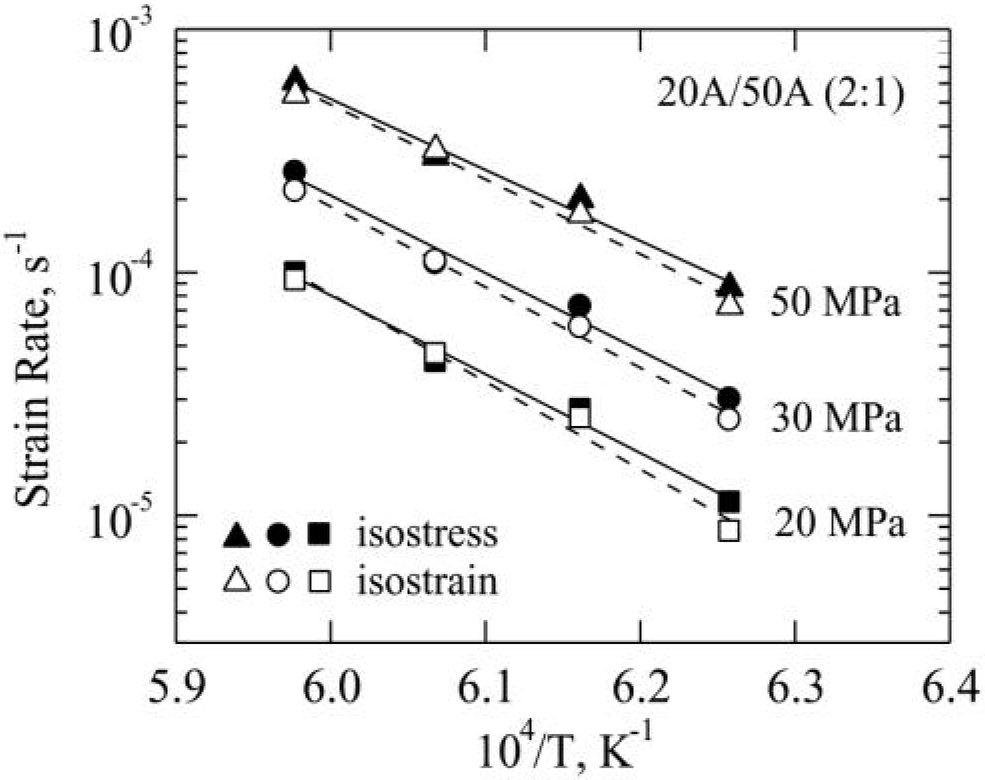

Figure 5.11 The temperature dependence of the strain rate for 20A/50A (2:1) particulate laminates in the isostress orientation and isostrain orientation at 20 *MPa*, 30 *MPa*, and 50 *MPa*.

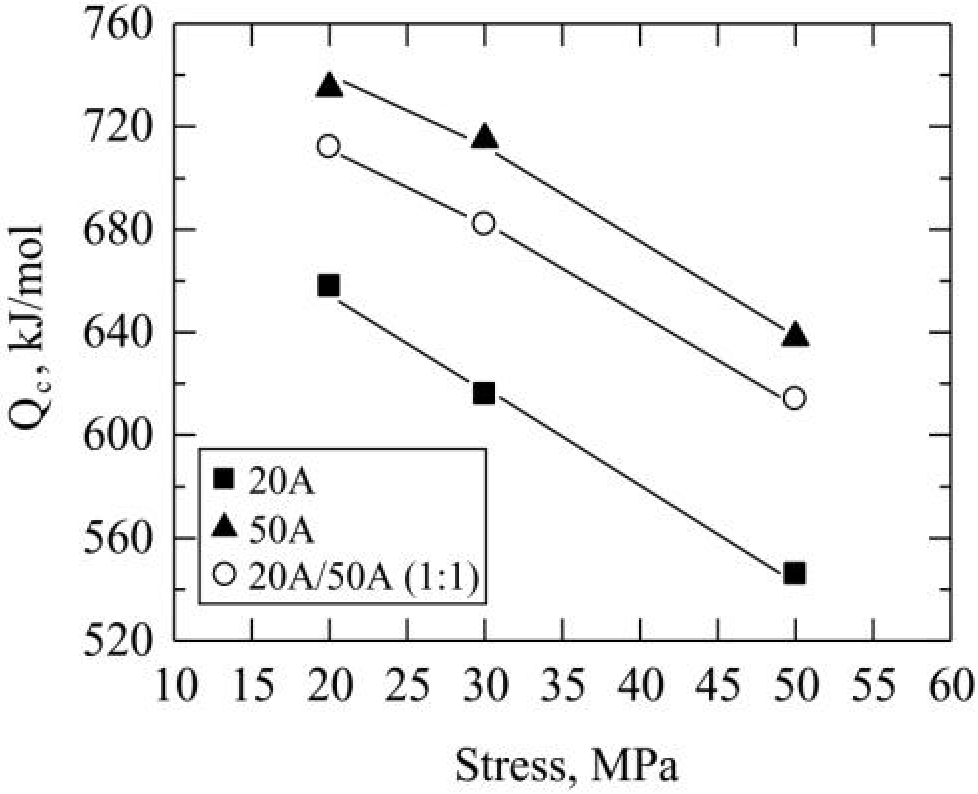

Figure 5.12 The dependence of the activation energy on stress for 20A, 50A particulate composites, and 20A/50A (1:1) particulate laminate in the isostress orientation.

5.3 DISCUSSION

5.3.1 Microstructure

Prior to testing, the particulate laminates used in the current study exhibited lower density than the particulate composites used in Chapter 4. As a result, many of the specimens exhibited a slight increase $(\leq 1\%)$ in density during compression testing. To evaluate the influence of changes in density that occurred during compressive deformation, the strain, e_p, attributed to densification was calculated.

The mass, m, and cross-sectional area, A, are assumed not to change with the reduction of the porosity, *i.e.* $m_0 = m_1 = m$ and $A_0 = A_1 = A$, but the height of the sample, L, decreases from L_0 to L_1. The subscripts 0 and 1 represent the sample with and without the porosity. The density of the sample, r, is given by

$$r_0 = \frac{m}{V_0} \tag{5.1}$$

$$r_1 = \frac{m}{V_1} \tag{5.2}$$

where V is the volume of the sample. Since $V_0 = AL_0$ and $V_1 = AL_1$,

$$\frac{r_1 - r_0}{r_0} = \frac{\dfrac{m}{AL_1} - \dfrac{m}{AL_0}}{\dfrac{m}{AL_0}} = \frac{\dfrac{1}{L_1} - \dfrac{1}{L_0}}{\dfrac{1}{L_0}} = \frac{L_0 - L_1}{L_0} = e_p \qquad (5.3)$$

Therefore, the strain from densification corresponds to a linear decrease of the height of the sample. Experimental measurements indicated that $e_p \leq 1\%$. Compared to the total engineering strain (~ 11%) during testing, the strain from densification is relatively small. The flow stress at a given strain rate is nearly constant for different strains (see Figure 5.2), further confirming that densification and other changes in microstructure do not strongly influence the deformation behavior for the current tests.

5.3.2 High-Temperature Deformation

Previous studies of Al_2O_3/Y-TZP particulate composites suggested that stress exponents were approximately 2 for composites with high Al_2O_3 contents and at high strain rates and approximately 3 for low Al_2O_3 contents and at low strain rates [130]. In addition, Jiménez-Melendo *et al.* [128] have reported stress exponents of approximately 2 over similar stress and temperature ranges for Al_2O_3/Y-TZP hybrid laminates consisting of layers of Y-TZP and Al_2O_3/Y-TZP. Our results for Al_2O_3/Y-TZP particulate laminates are similar, with stress exponents of approximately 2 at higher strain rates and a transition to higher values as strain rate is decreased. This suggests that there is a similar deformation mechanism between Al_2O_3/Y-TZP particulate composites and particulate laminates.

5.3.3 The Constraint between Soft Layer and Hard Layer

Jiménez-Melendo *et al.* [128] have shown that the hard layer imposes constraint on the deformation of the soft layer. Due to constraint, the particulate laminates are more resistant to deformation than particulate composites, especially when the compositions difference between the layers is large. Figure 5.13 and 5.14 illustrate the influence of constraint on deformation. To enhance the observation of this effect, all the samples shown in Figure 5.13 and 5.14 were tested to relatively large strains, which were obtained by running compression SRC tests several times on the same samples. Figure 5.13a illustrates the sample in the isostress orientation, where the applied stress is perpendicular to the layer interface. The shaded surface shown in Figure 5.13a was observed by optical microscopy and the results are shown in Figure 5.13b - 5.13d with the layers with the darker shading contain more Y-TZP. The influence of constraint is most apparent near the edges of the samples after testing because of the loss of constraint at free surfaces away from the interfaces. During compressive loading in the isostress orientation, both layers expand in the direction perpendicular to the loading but because of the constraint imposed on the layers, differences in strain can only occur near the free surfaces. It is apparent that the softer layers containing more Y-TZP exhibit more strain at the free surface, as expected. Similar observations were made on samples tested in the isostrain orientation (see Figure 5.14). Note, the samples tested in the isostrain orientation have only 2 free surfaces that contain interfaces and are not under the applied load whereas the samples tested in the isostress orientation have 4 free surfaces that contain interfaces and are not under the applied load.

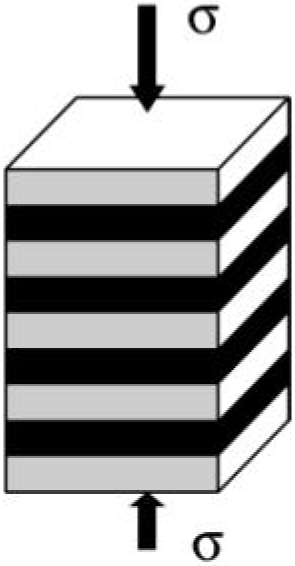

(a)

Figure 5.13

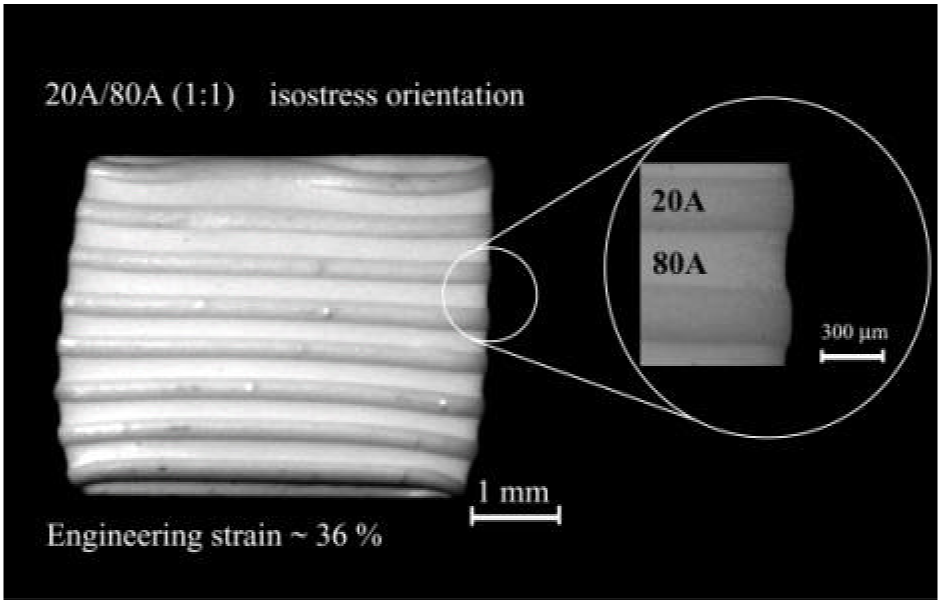

(b)

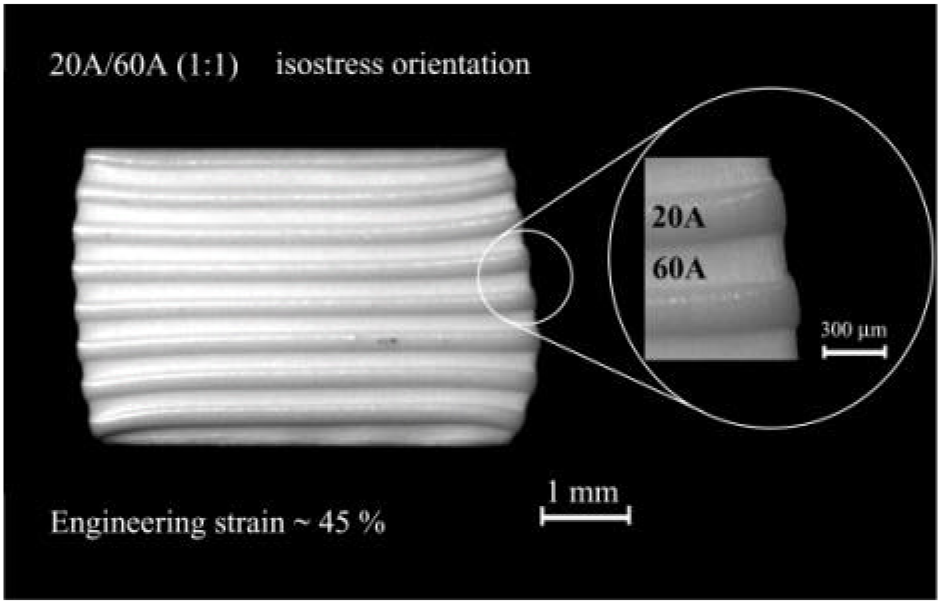

(c)

Figure 5.13

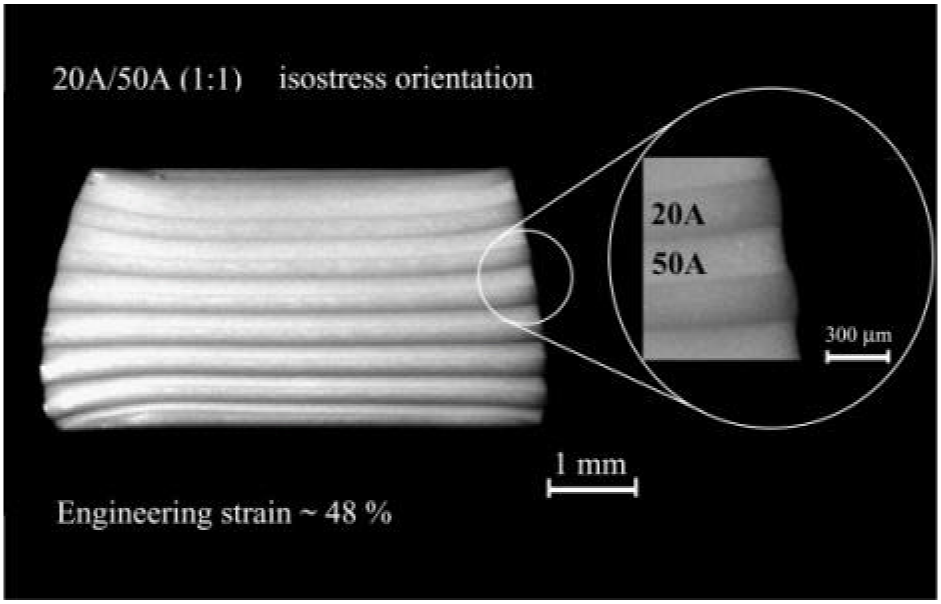

(d)

Figure 5.13 (a) a schematic of the isostress orientation where the axis of applied stress is perpendicular to the layer interface. The shaded face is observed by optical microscopy in (b), (c), and (d) for the 20A/80A (1:1), 20A/60A (1:1), and (d) the 20A/50A (1:1) specimens.

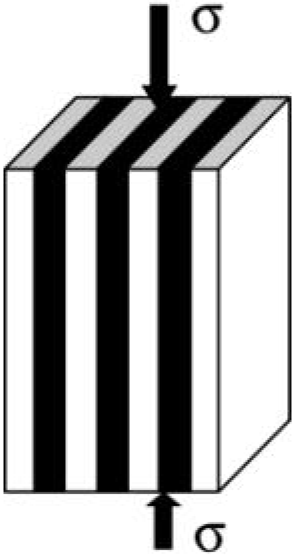

(a)

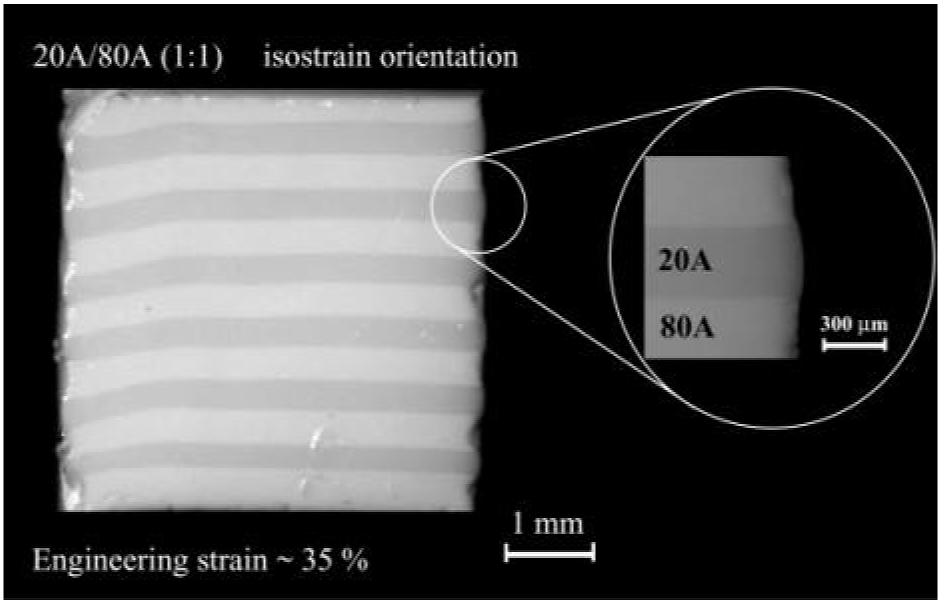

(b)

Figure 5.14

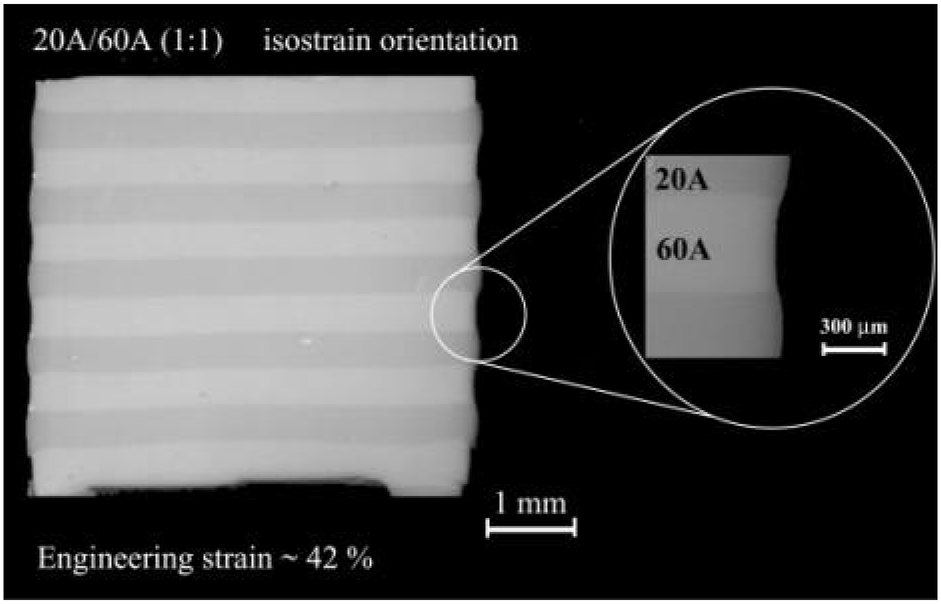
20A/60A (1:1) isostrain orientation
20A
60A
300 µm
1 mm
Engineering strain ~ 42 %

(c)

Figure 5.14

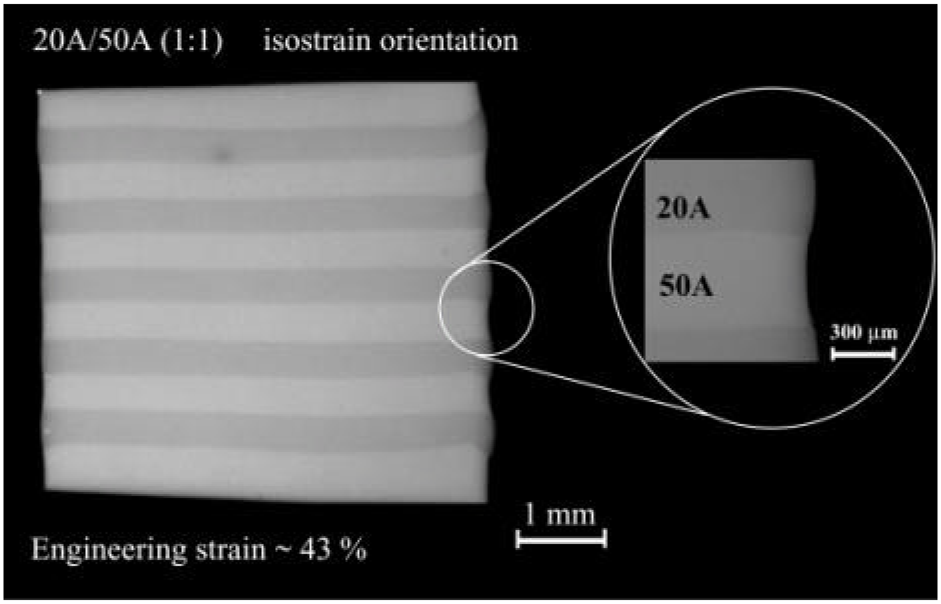

(d)

Figure 5.14 (a) a schematic of the isostrain orientation where the axis of applied stress is parallel to the layer interface. The shaded face is observed by optical microscopy in (b), (c), and (d) for the 20A/80A (1:1), 20A/60A (1:1), and 20A/50A (1:1) specimens.

5.3.4 Models for Deformation Behavior

In general, the strain rate, $\dot{e}$, in the deformation of polycrystalline materials at elevated temperature may be expressed using the phenomenological equation for creep [68]:

$$\dot{e} = A\left(\frac{s}{E}\right)^{n}\left(\frac{b}{d}\right)^{p}\exp\left(-\frac{Q_c}{RT}\right) \tag{5.4}$$

where s is the stress, E is the dynamic, unrelaxed Young's modulus, T is the absolute temperature, b is the magnitude of Burgers vector, d is the grain size, n is the stress exponent, p is the inverse grain size exponent, Q_c is the activation energy for creep, R is the gas constant, and A is a material constant.

French *et al.* [106] proposed that the creep of particulate composites could be analyzed using either an isostress or an isostrain model. In the isostress model, the average strain rate in the composite, $\dot{e}_c$, is given by

$$\dot{e}_c = V_1\dot{e}_1 + V_2\dot{e}_2 \tag{5.5}$$

where V_1 and $\dot{e}_1$ are the volume fraction and strain rate of component one and V_2 and $\dot{e}_2$ are the volume fraction and strain rate of component two. In the isostrain model, the average stress in the composite, s_c, can be represented as

$$s_c = V_1 s_1 + V_2 s_2 \tag{5.6}$$

where σ_1 and σ_2 are the stress of component one and component two, respectively. Assuming that each component obeys Equation 5.4, the isostrain model predicts the composite flow stress to be

$$\sigma_c = V_1 K_1 \dot{\varepsilon}_c^{1/n_1} + V_2 K_2 \dot{\varepsilon}_c^{1/n_2} \tag{5.7}$$

where $K_i = E_i (A_i)^{1/n_i} (d_i / b_i)^{p_i / n_i} \exp(Q_{ci} / n_i RT)$ for each component i.

To determine whether existing models could be used to describe the deformation behaviors of particulate laminates, the behavior of particulate composites with compositions between 20A - 80A were first examined. Previously, we have shown that the isostress model did not fit the experimental data well for Al_2O_3/Y-TZP particulate composites. Although the isostrain model yielded better fits to the data, physically unrealistic values of the fitting parameters were observed. We found that the deformation behavior of Al_2O_3/Y-TZP particulate composites could be accurately modeled using a constrained isostrain model, *i.e.*

$$\sigma_c = (V_1 K_1 + V_2 K_2) \dot{\varepsilon}_c^{1/2} \tag{5.8}$$

where the subscripts 1 and 2 represent Y-TZP and Al_2O_3, respectively, and the stress exponents for Al_2O_3 and Y-TZP were both taken to be 2, *i.e.* $n_1 = n_2 = 2$, for all the compositions ranging from 20 - 80 vol% Al_2O_3 [130]. To model the behaviors of Al_2O_3/Y-TZP particulate laminates, they were considered to consist of two layers, each of which was particulate composite. In Chapter 4, it was shown that the stress exponents for Al_2O_3/Y-TZP particulate composites were about 2. Therefore, the constrained isostrain model (Equation 5.8) should also be appropriate for particulate laminates, with a value of $n = 2$ for both layer 1 and layer 2.

The isostress and constrained isostrain models (Equation 5.5 and Equation 5.8) where the subscripts 1 and 2 represent layer 1 and layer 2, respectively, were then used to predict the deformation behaviors of particulate laminates and comparison to experimental data was performed. For this analysis, a flow stress of 50 *MPa* was selected. Note that no fitting parameters were used since all parameters are specified for each laminate composition. The data for particulate composites from Table 5.2 were obtained from the results of Chapter 4 and used as input for the behavior of each layer.

Table 5.2 The properties of Al_2O_3/Y-TZP particulate composites (T = 1350^{o}C, $s = 50\ MPa,\ n = 2$), where $s = K\dot{e}^{1/n}$ [130].

Particulate Composites	$\dot{e}$ (s^{-1})	*K*
20A	2.73×10^{-4}	3026.1
40A	1.66×10^{-4}	3880.8
50A	1.00×10^{-4}	5000.0
60A	5.51×10^{-5}	6735.9
80A	2.77×10^{-5}	9500.1

The experimental data and predictions from the isostress model and constrained isostrain models are shown in Figure 5.15a - 5.15d. It is apparent that when the composition differences between the layers are small (*e.g.* 20A/40A and 60A/80A), the differences between the predictions for the isostress model and constrained isostrain model are not discernable. As a result, we cannot tell which model fits the data better only from Figure 5.15a and Figure 5.15d. When the composition differences between the layers are large (*e.g.* 20A/60A and 40A/80A), the differences between the predictions are large, as shown in Figures 5.15b and 5.15c, where it can be concluded that the experimental data tend to follow the isostrain model whether the samples are tested in the isostress or isostrain orientation.

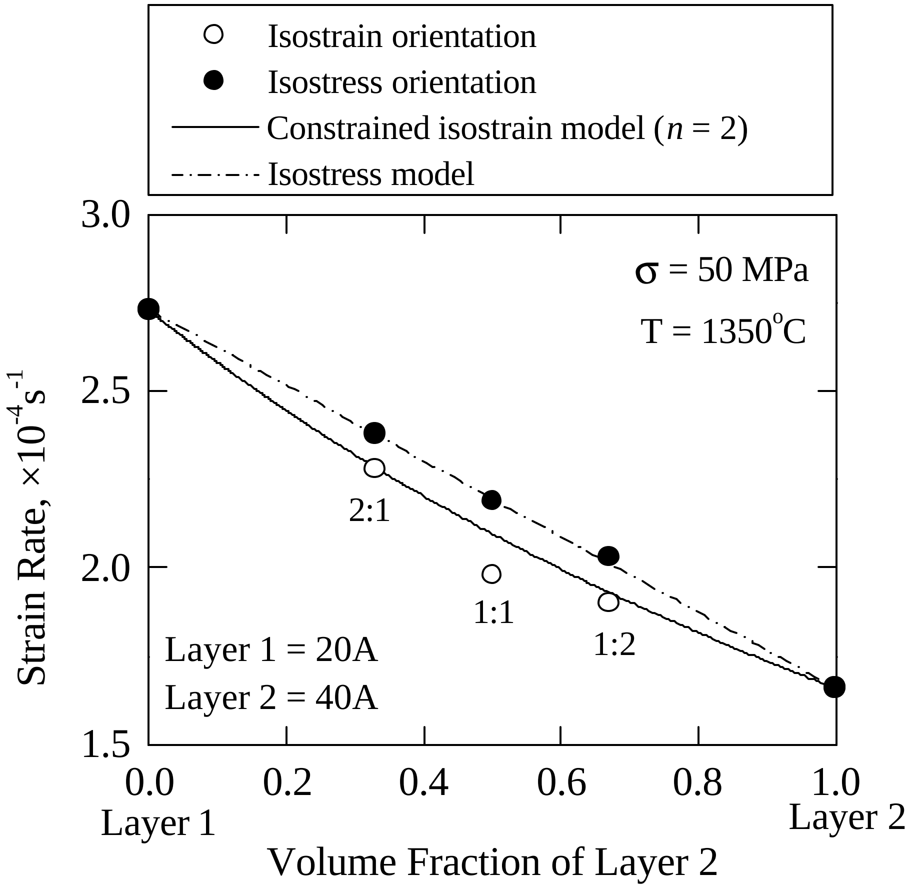
○ Isostrain orientation
● Isostress orientation
Constrained isostrain model (n = 2)
Isostress model
σ = 50 MPa
T = 1350°C
Strain Rate, ×10^{-4} s^{-1}
3.0
2.5
2.0
1.5
2:1
1:1
1:2
Layer 1 = 20A
Layer 2 = 40A
0.0
0.2
0.4
0.6
0.8
1.0
Layer 1
Layer 2
Volume Fraction of Layer 2

(a)

Figure 5.15

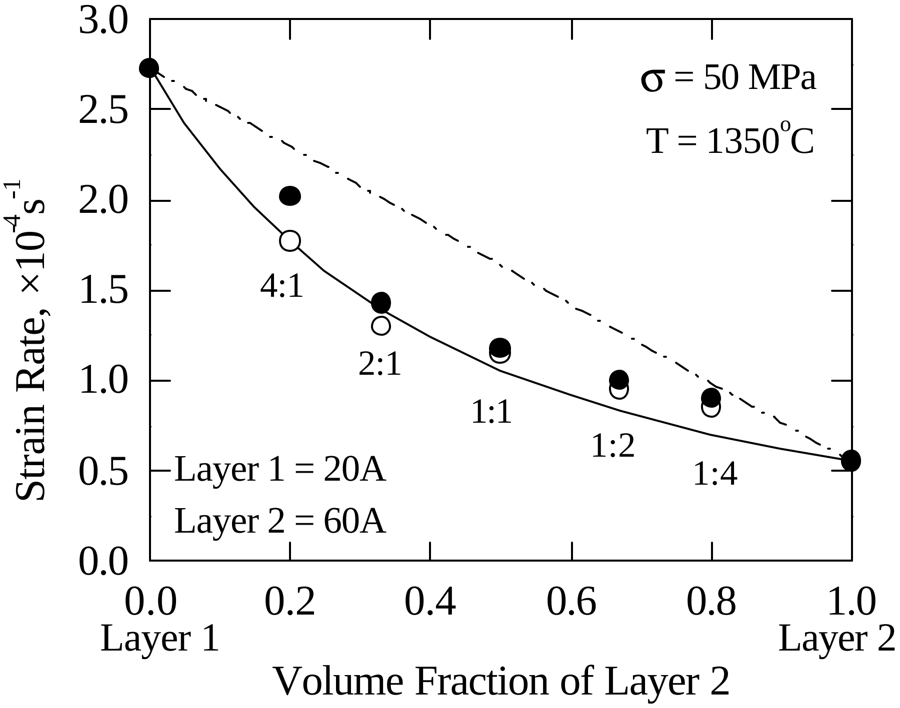
σ = 50 MPa
T = 1350°C
Layer 1 = 20A
Layer 2 = 60A
4:1
2:1
1:1
1:2
1:4
Strain Rate, ×10⁻⁴s⁻¹
Volume Fraction of Layer 2
Layer 1
Layer 2
0.0
0.5
1.0
1.5
2.0
2.5
3.0
0.0
0.2
0.4
0.6
0.8
1.0

(b)

Figure 5.15

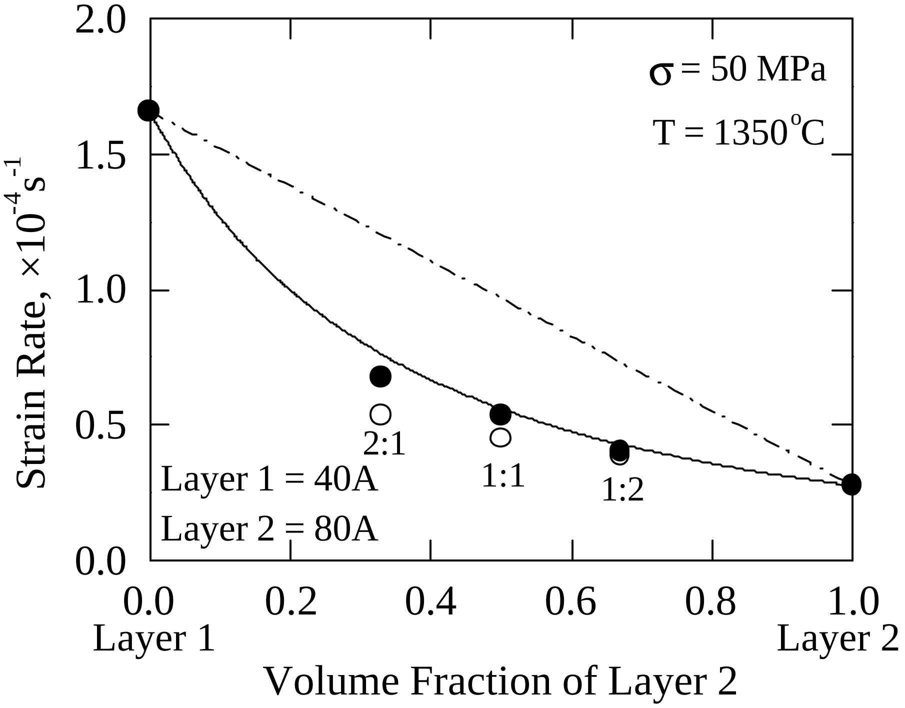

2.0
1.5
1.0
0.5
0.0
Strain Rate, ×10^{-4}s^{-1}
σ = 50 MPa
T = 1350°C
2:1
1:1
1:2
Layer 1 = 40A
Layer 2 = 80A
0.0
0.2
0.4
0.6
0.8
1.0
Layer 1
Layer 2
Volume Fraction of Layer 2

(c)

Figure 5.15

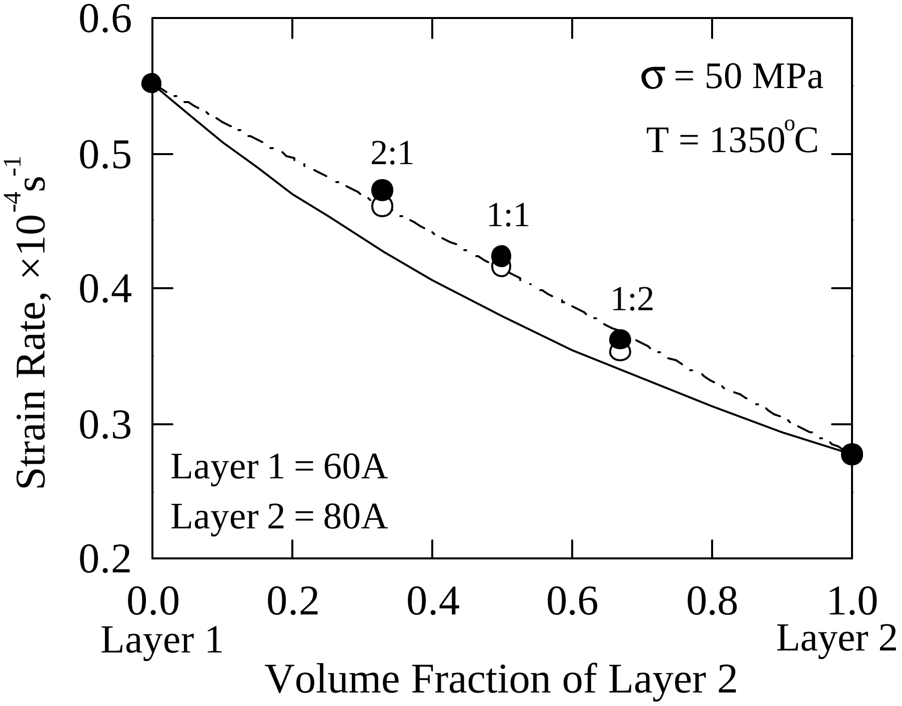

(d)

Figure 5.15 The dependence of the strain rate on the volume fraction of the hard layer. (a) 20A/40A; (b) 20A/60A; (c) 40A/80A; (d) 60A/80A particulate laminates.

To further determine the applicability of the constrained isostrain model to Al_2O_3/Y-TZP particulate laminates at all applied stresses and strain rates, the flow stresses for 20A/60A laminates at three different strain rates of 1.00×10^{-5} s^{-1}, 1.00×10^{-4} s^{-1}, and 3.16×10^{-4} s^{-1}, are plotted as a function of volume fraction of the hard layer (*i.e.* 60A) in Figure 5.16. The open symbols correspond to the data for particulate composites which were obtained from Figure 4.5. The solid lines in Figure 5.16 are the predictions from the constrained isostrain model (Equation 5.8) with $K_1 = 3026.1$, $K_2 = 6735.9$ (see Table 5.2). The subscripts 1 and 2 represent 20A (layer 1) and 60A (layer 2). Good agreement is observed between the predictions from the constrained isostrain model and the experimental data at all stresses and strain rates. As shown in Figure 5.16, the strength of the particulate laminates increases with increasing volume fraction of the hard layer (*i.e.* 60A), especially at higher strain rates, *e.g.* 3.16×10^{-4} s^{-1}.

As discussed by Jiménez-Melendo *et al.* [128], the discrepancy between the isostress model and experimental data for samples tested in the isostress orientation results from the constraint imposed by the hard layer on the soft layer, which is not accounted for this model, where the stresses are assumed to be constant in each layer, but the strains can vary. In reality, because volume is conserved during plastic deformation and because the layers remain bonded, the strains in each layer must also be constant, except near the free surfaces, where this constraint is relaxed away from the interfaces. As a result, the behavior of specimens tested in both orientations should be similar, as was observed. The slightly harder response for specimens tested in the isostrain orientation likely results from this orientation having fewer free surfaces where the constraint can be relaxed (2 for the isostrain versus 4 for the isostress orientation). Jiménez-Melendo also found that the isostrain model could be used to predict the behavior of Y-TZP/Al_2O_3+Y-TZP hybrid laminates tested in the isostrain orientation [128]. Although they did not attempt to predict the behavior of specimens tested in the isostress orientation, it is apparent from visual inspection that the isostrain model could be also used to predict the behavior of their specimens tested in the isostress orientation.

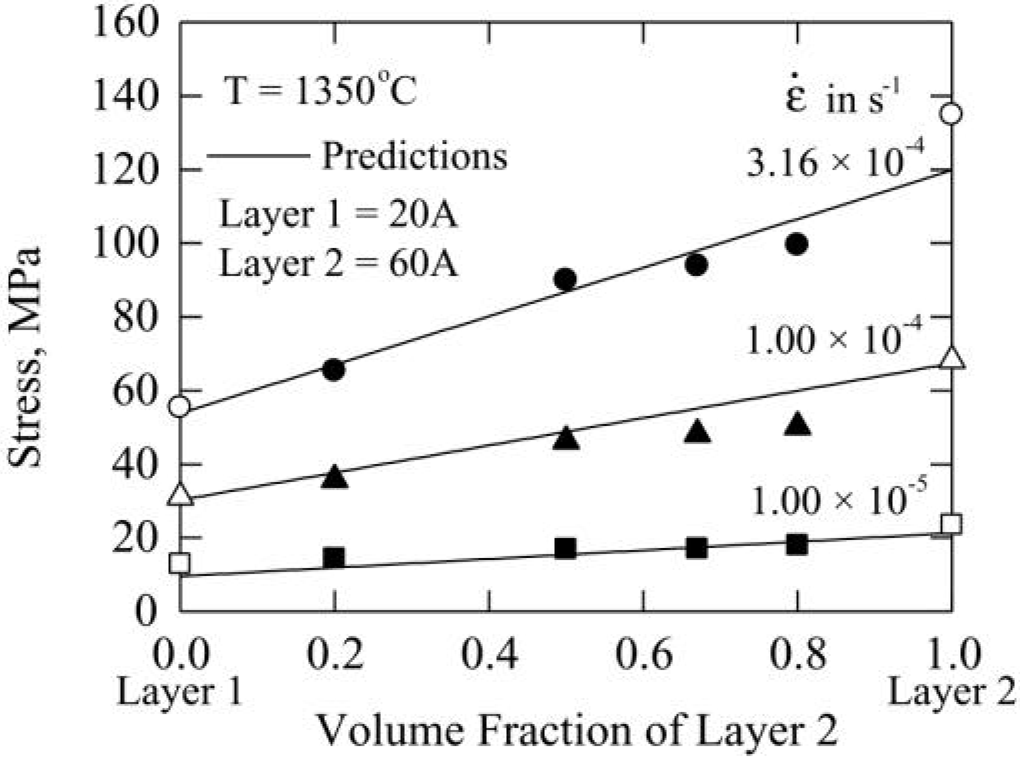

Figure 5.16 The flow stresses at three different strain rates for 20A/60A specimens in the isostress orientation. The solid lines are predictions from the constrained isostrain model.

In addition to flow stress and strain rate, the activation energy of particulate laminates could also be analyzed using either an isostress model or an isostrain model [106]. For the isostress case, the activation energy of the laminate, Q_c, is expressed by the relation

$$Q_c = (V_1)(\dot{e}_1/\dot{e}_c)Q_1 + (V_2)(\dot{e}_2/\dot{e}_c)Q_2 \tag{5.9}$$

where Q, V, and $\dot{e}$ are the activation energy, the volume fraction, and strain rate. The subscripts 1 and 2 represent layer 1 and layer 2, respectively. According to Equations 5.5, Equation 5.9 can be rearranged as

$$Q_c = \frac{V_1\dot{e}_1Q_1 + V_2\dot{e}_2Q_2}{V_1\dot{e}_1 + V_2\dot{e}_2} \tag{5.10}$$

For the isostrain case, the activation energy of the laminate, Q_c, is given by

$$Q_c = (V_1)(n_c/n_1)(s_1/s_c)Q_1 + (V_2)(n_c/n_2)(s_2/s_c)Q_2 \tag{5.11}$$

where n is the stress exponent and s is the stress. For the constrained isostrain model, Equation 5.11 can be simplified as

$$Q_c = (V_1)(s_1/s_c)Q_1 + (V_2)(s_2/s_c)Q_2 \tag{5.12}$$

where the stress exponent of Al_2O_3/Y-TZP particulate laminates and their constituent layers were taken to be 2, *i.e.* $n_c = n_1 = n_2 = 2$. According to Equation 5.8, Equation 5.12 can be rewritten as

$$Q_c = \frac{V_1K_1Q_1 + V_2K_2Q_2}{V_1K_1 + V_2K_2} \tag{5.13}$$

Using the isostress model (Equation 5.10) and constrained isostrain model (Equation 5.13) the activation energies for particulate laminates were predicted and compared to experimental results. The analysis was performed at a stress of 50 *MPa*. For the isostress model, $s_1 = s_2 = s_c = 50$ *MPa*; the activation energies of layer 1 and layer 2 at 50 *MPa*, Q_1 and Q_2, were taken from the Al_2O_3/Y-TZP particulate composites (see Chapter 4). For the isostrain model, the stresses in layer 1 and layer 2 can be different, therefore Q_1 and Q_2 cannot be determined a prior. For simplification we have assumed that $s_1 = s_2 = 50$ *MPa*, allowing us to use the values of Q_1 and Q_2 from Chapter 4. All the other parameters in Equations 5.10 and 5.13 were obtained from Table 5.2. Figure 5.17 shows the predicted values of the activation energies of 20A/50A particulate laminates as a function of volume fraction of the hard layer, *i.e.* 50A. The experimentally determined data obtained from both isostress orientations and isostrain orientations are also plotted in Figure 5.17. From this plot it is apparent that the constrained isostrain model fits more data than isostress model. However, it is difficult to make a further comparison between the two models due to scatter in the data because of the relatively small difference in the activation energies between Al_2O_3 and Y-TZP. Thus, it is not possible to determine which model fits the data better.

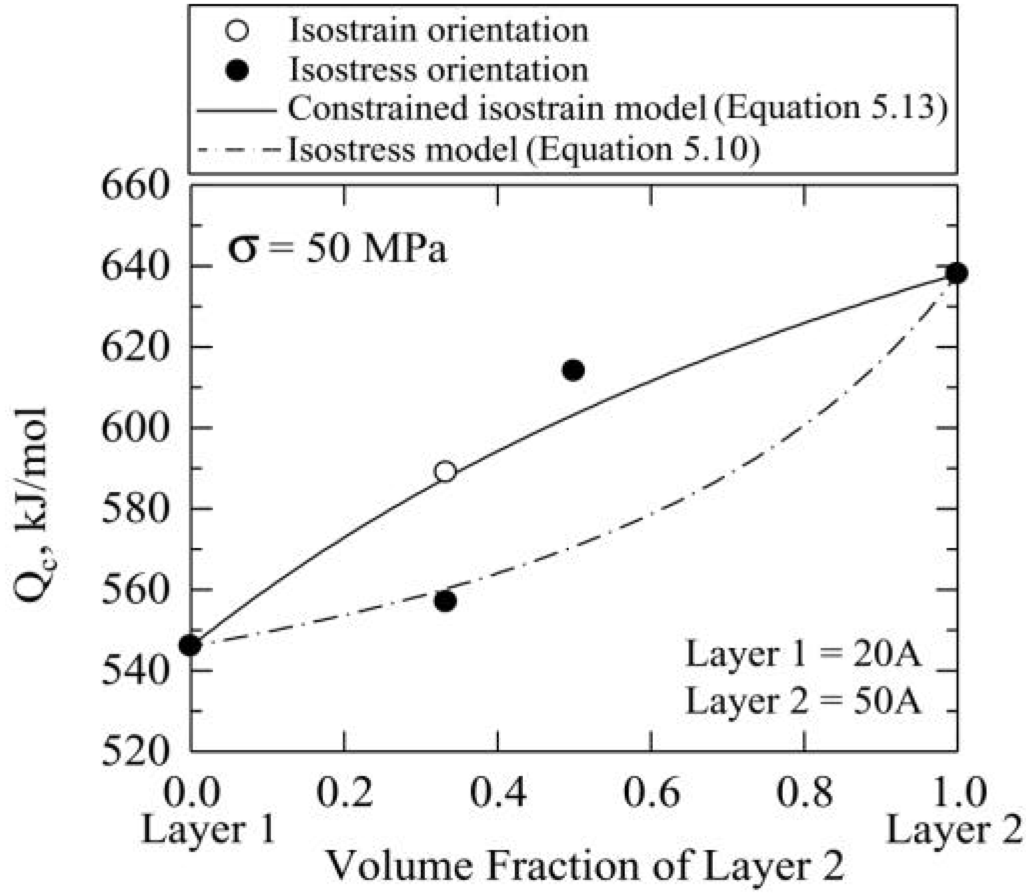

Figure 5.17 The dependence of activation energy on the volume fraction of 50A layer for 20A/50A particulate laminates.

5.4 CONCLUSIONS

Al_2O_3/Y-TZP particulate laminates with varying compositions and ratios of layer thickness were fabricated by tapecasting, lamination, and sintering. Compression SRC tests were conducted at 1350°C with a stable fine-grained microstructure. Experimental results showed that stress exponents of Al_2O_3/Y-TZP particulate laminates were approximately 2, which is similar to particulate composites. High-temperature deformation behaviors of particulate laminates were influenced by the overall compositions and the constraint imposed by the hard layer on the soft layer. Particulate laminates were stronger than particulate composites with the same overall composition, especially when the compositions of the layers in the laminates were markedly different. The composition of the hard layer dominated the observed behaviors of the laminates during the high-temperature deformation. Laminates in the isostrain orientation were only slightly stronger than laminates in the isostress orientation because constraint dictates that the strains in each layer must be constant. As a result, a constrained isostrain model with $n_1 = n_2 = 2$ provides a good prediction of the flow behavior for particulate laminates tested in either the isostrain or isostress orientation.

Chapter 6

High-Temperature Deformation of Al_2O_3/Y-TZP Particulate Composites and Laminates in Tension

6.1 INTRODUCTION

Selected Al_2O_3/Y-TZP particulate composites and laminates were fabricated by tapecasting, lamination and sintering. Tensile strain-rate-change (SRC) tests were conducted at 1350^{o}C with a total engineering strain of $\leq 16\%$. Comparisons of the high-temperature behaviors of both Al_2O_3/Y-TZP particulate composites and laminates tested in tension and compression are made. In addition, elongation-to-failure tests were performed at 1350^{o}C with a constant true strain rate of 1.00×10^{-4} s^{-1} allowing superplastic behaviors of Al_2O_3/Y-TZP particulate composites and laminates to be investigated.

6.2 EXPERIMENTAL RESULTS

6.2.1 Microstructure

SEM micrographs of 20A and 60A particulate composites are shown in Figure 6.1 after tensile SRC testing. Figure 6.1a and 6.1c were taken in the grip section, while Figure 6.1b and 6.1d were taken in the gage section. The grains with the light shading are Y-TZP and the grains with the dark shading are Al_2O_3. The Al_2O_3 and Y-TZP phases are generally well-dispersed. Both phases exhibit an equiaxed grain shape and fine grain size. After tensile SRC testing, the mean grain sizes of Al_2O_3 for the grip section of the 20A and 60A specimens are 0.37 and 0.42 *mm*, respectively; the mean grain size of Y-TZP for the gage section of the 20A and 60A specimens are 0.38 and 0.47 *mm*, respectively. Because the stress in the grip section during testing is much lower than that in the gage section and because the testing temperature is lower than the sintering temperature, it is assumed that the microstructure in the grip section is representative of the material prior to testing. Figure 6.1 indicates that the grain shapes remain equiaxed and that very little grain growth occurred during the SRC testing, as is shown in Table 6.1.

Table 6.1 Grain sizes of 20A and 60A particulate composites after tensile SRC testing.

		$\bar{d}_{Al_2O_3}$ (mm)	$\bar{d}_{Y-TZP}$ (mm)
20A (tensile SRC)	Grip	0.37 ± 0.12	0.32 ± 0.10
	Gage	0.38 ± 0.12	0.34 ± 0.10
60A (tensile SRC)	Grip	0.42 ± 0.15	0.29 ± 0.09
	Gage	0.47 ± 0.16	0.30 ± 0.09
20A (elongation-to-failure)	Grip	0.34 ± 0.10	0.32 ± 0.10
	Gage	0.46 ± 0.18	0.43 ± 0.15

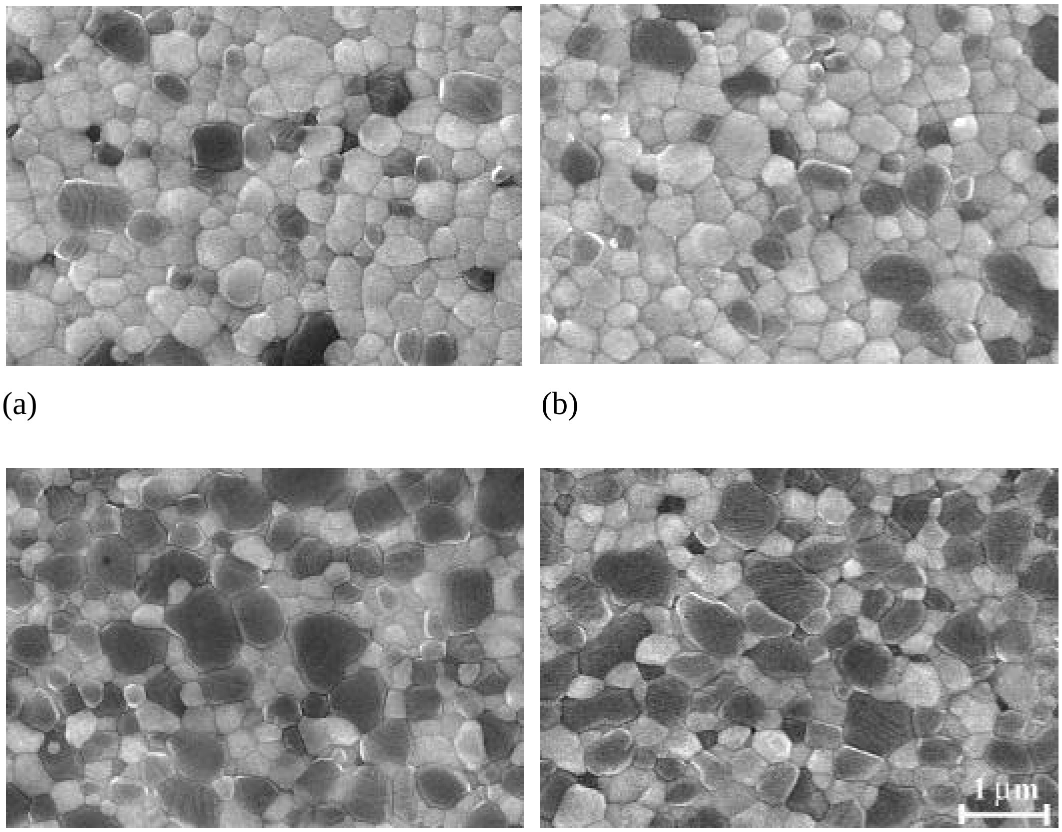

(a) (b)

(c) (d)

Figure 6.1 Microstructure of 20A and 60A particulate composites after tensile SRC testing: (a) 20A grip; (b) 20A gage; (c) 60A grip; (d) 60A gage. The orientation of the applied stress is horizontal.

Figure 6.2 shows the microstructural evolution of the 20A particulate composite during elongation-to-failure testing. After testing, the grain shapes remain equiaxed. The grain size of Al_2O_3 increases from 0.34 to 0.46 *mm*, while the grain size of Y-TZP increases from 0.32 to 0.43 *mm* (See Table 6.1).

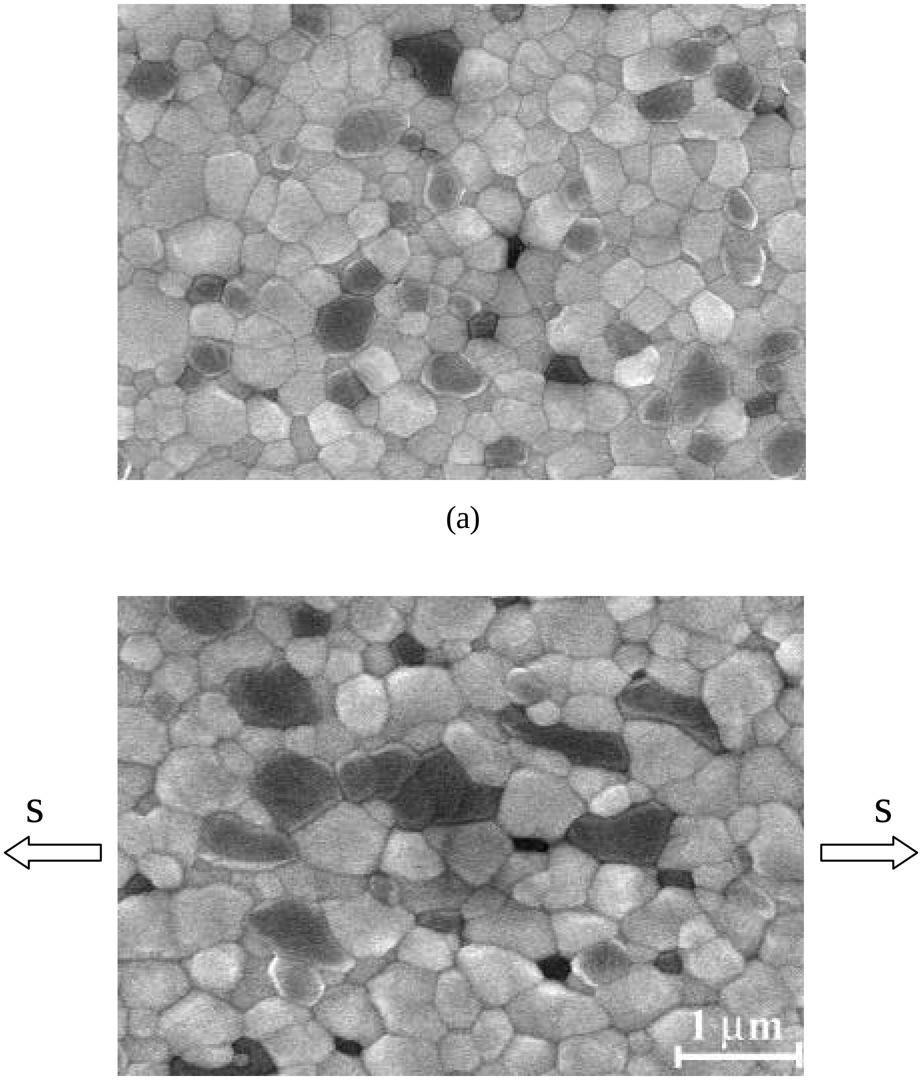

(a)

(b)

Figure 6.2 Microstructure of the 20A particulate composite after elongation-to-failure testing: (a) 20A grip; (b) 20A gage. The orientation of the applied stress is horizontal.

Figure 6.3 shows the microstructure of the 20A/60A (1:1) particulate laminates after tensile SRC testing and elongation-to-failure testing, respectively. The layers containing more dark grains are 60A. The interfaces between the layers of particulate composites with different compositions are straight and remain bonded during testing. As shown in Figure 6.3a, the microstructure of the 20A/60A laminates does not appear to exhibit any change in grain size or grain shape after the SRC testing. However, after the elongation-to-failure testing, significant grain growth and cavitation are apparent in the gage section, especially in the hard layer, *i.e.* 60A, as shown in Figure 6.3b. 3 - 4% decreases in densities of Al_2O_3/Y-TZP particulate composites and laminates after the elongation-to-failure testing were observed, while less than a 1% decrease in densities was observed after the SRC testing (see Table 6.2).

Table 6.2 Relative densities of 20A, 60A particulate composites, and 20A/60A particulate laminates after testing.

Particulate Composites and Particulate Laminates		Relative Densities (%)	
		After tensile SRC testing	After elongation-to-failure testing
20A	Grip	99.6	99.2
	Gage	98.7	95.4
20A/60A (1:1)	Grip	98.2	97.6
	Gage	97.3	94.6
20A/60A (1:2)	Grip	-	98.0
	Gage	-	94.2
20A/60A (1:4)	Grip	97.8	-
	Gage	97.3	-
60A	Grip	98.7	-
	Gage	98.2	-

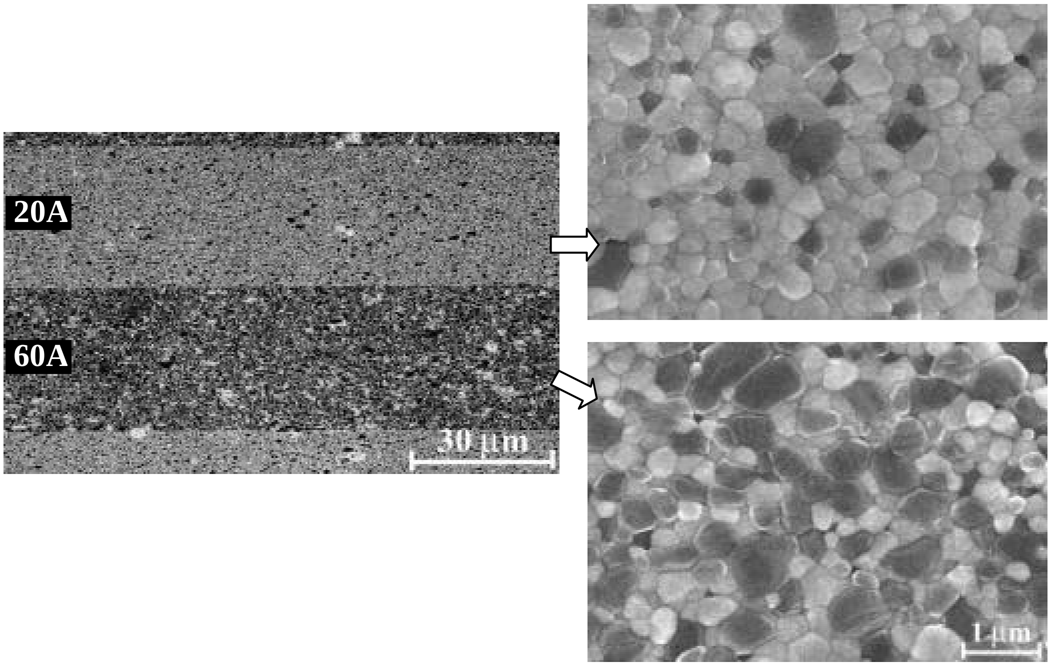

(a)

Figure 6.3

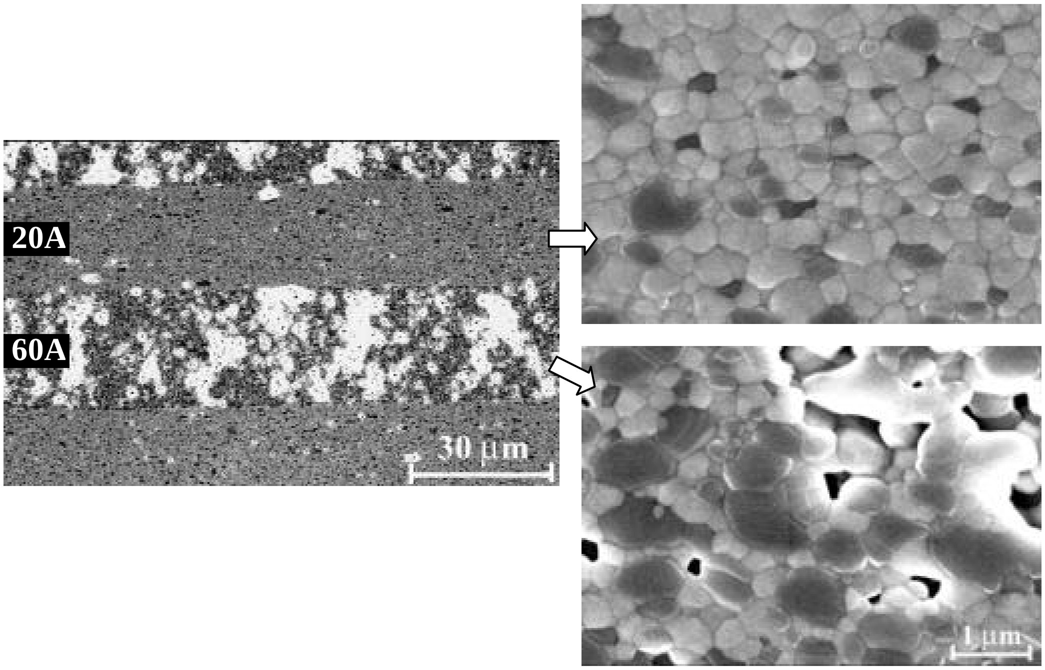

(b)

Figure 6.3 Microstructure of 20A/60A (1:1) particulate laminates in the gage section: (a) after tensile SRC testing; (b) after elongation-to-failure testing.

6.2.2 Deformation Behavior

Figure 6.4 shows data from a representative tensile SRC test for the 20A/60A (1:2). The total true strain for this test is $e = 0.14$. After a brief transient at every rate change, a reasonably steady-state stress is achieved. It is also apparent that for the repeated steps at a true strain rate of 1.00×10^{-4} s^{-1}, the flow stress at a given rate is nearly constant over the range of strains imposed in any single SRC test, with slightly strengthening. Behaviors similar to those shown in Figure 6.4 were observed for all the particulate composites and particulate laminates tested in tension.

The relationships between the true stress and the strain rate are plotted on log-log scales in Figure 6.5 for 20A, 60A particulate composites, and 20A/60A particulate laminates. For all these materials stress exponents are approximately equal to 2. A slight negative curvature is apparent in all of the datum sets, indicating a decrease in stress exponent with increasing stress. Similar behaviors have been observed previously in Al_2O_3/Y-TZP particulate composites and laminates tested in compression. At a given strain rate, the flow stress decreases as the overall volume fraction of Y-TZP increases. Comparing all the 20A/60A particulate laminates with different layer thickness ratios, when the layer thickness ratios are equal or the thicker layer contains more Al_2O_3, there is little effect of layer thickness ratios on flow stress, in agreement with the data presented in Chapter 5 for materials tested in compression.

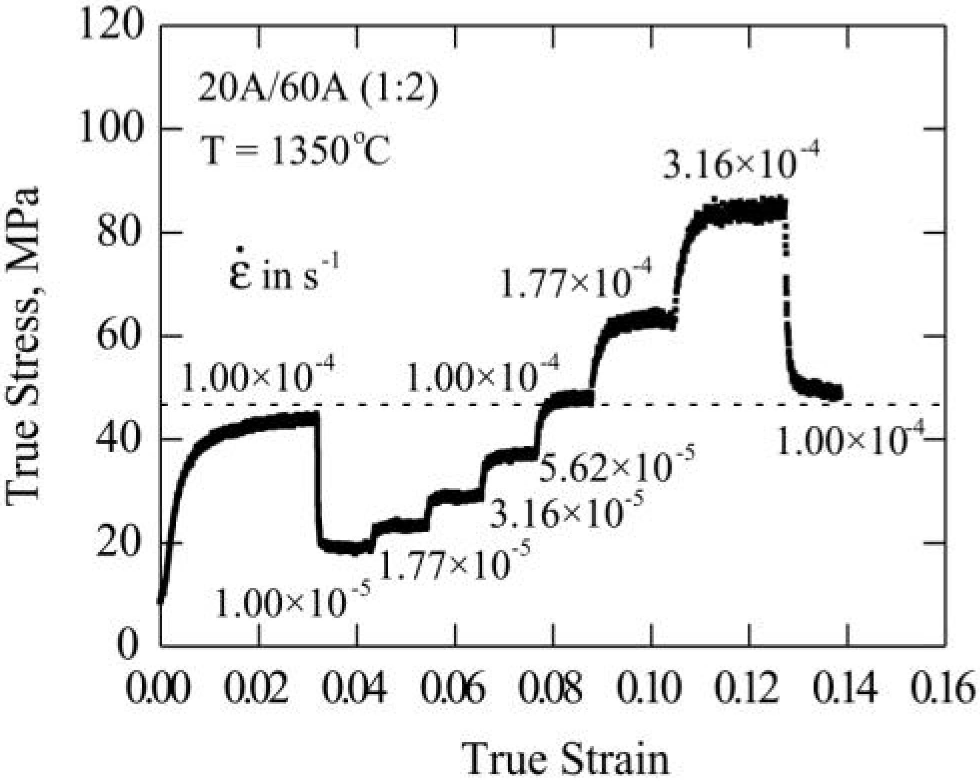

Figure 6.4 True stress versus true strain for 20A/60A (1:2) specimen during a representative tensile SRC test. The dashed line indicates the average flow stress at a strain rate of 1.00×10^{-4} s^{-1}.

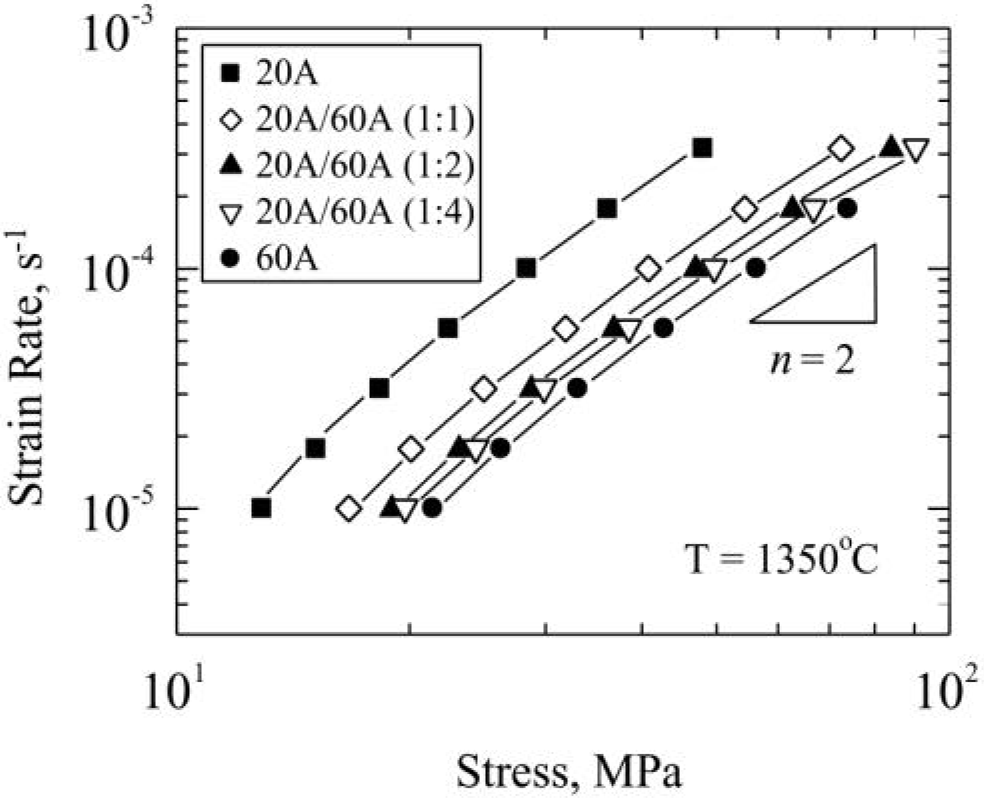

Figure 6.5 Strain rate versus stress on dual-logarithmic scales for 20A, 60A particulate composites, and 20A/60A particulate laminates tested in tension.

Figure 6.6 shows the effect of stress state (compression and tension) on the high-temperature deformation behaviors of Al_2O_3/Y-TZP particulate composites and particulate laminates. The particulate composites and laminates exhibit similar stress exponents (n ~ 2) and resistance to deformation in both tension and compression tests. Taking a closer look at Figure 6.6, it can be seen that the flow stress in tension tends to be slightly lower than that in compression at higher stress, indicating that the material tested in tension is softer at a given strain rate. Both materials tested in compression and tension exhibit a very small amount of grain growth but the density of the material tested in compression slightly increases whereas the density of the material tested in tension decreases during testing. Therefore, it is the cavitation that is responsible for the observed difference between compression and tension at larger strains.

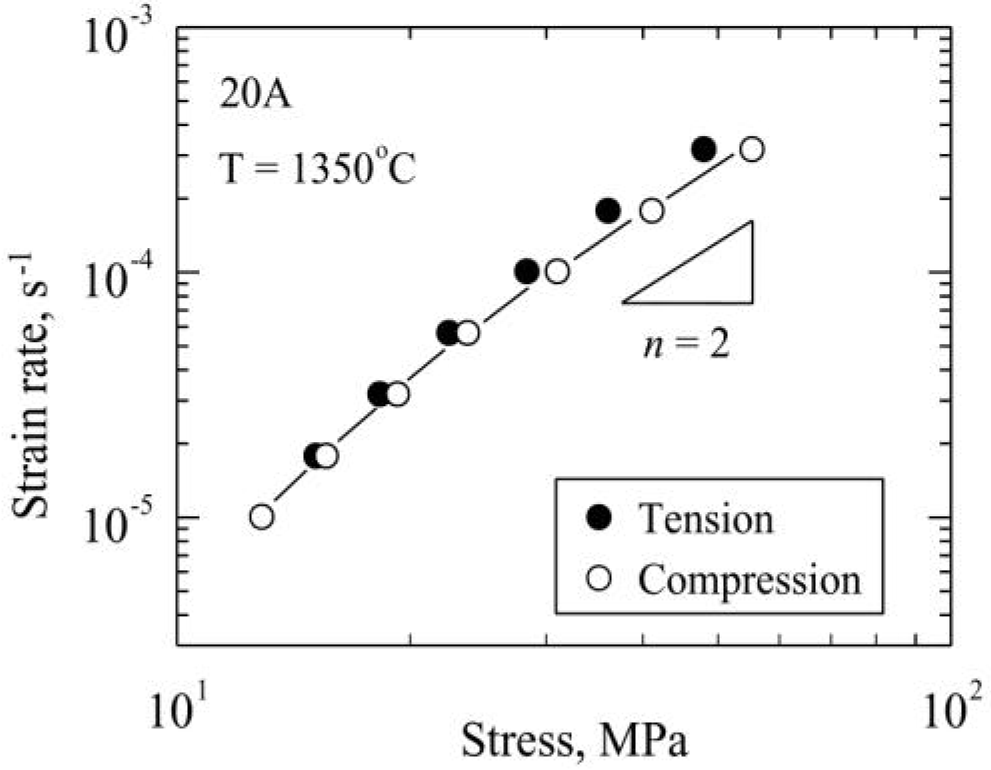
10^{-3}
10^{-4}
10^{-5}
Strain rate, s^{-1}
20A
T = 1350°C
$n = 2$
● Tension
○ Compression
10^1
10^2
Stress, MPa

(a)

Figure 6.6

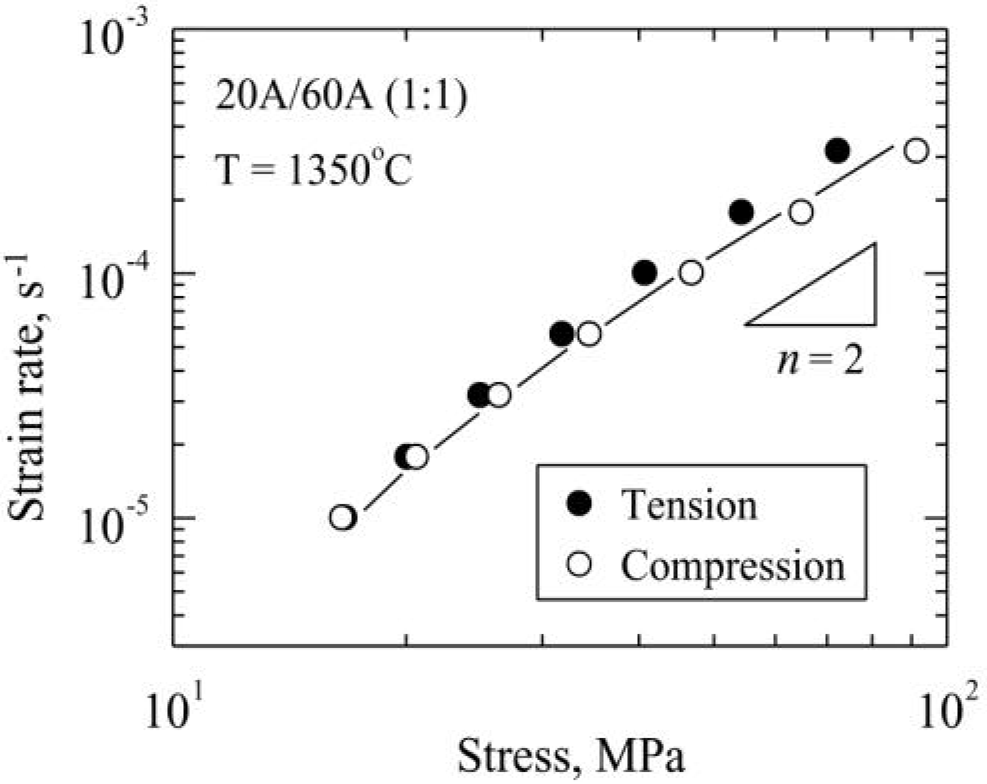
10^-3
10^-4
10^-5
Strain rate, s^-1
20A/60A (1:1)
T = 1350°C
n = 2
Tension
Compression
10^1
10^2
Stress, MPa

(b)

Figure 6.6

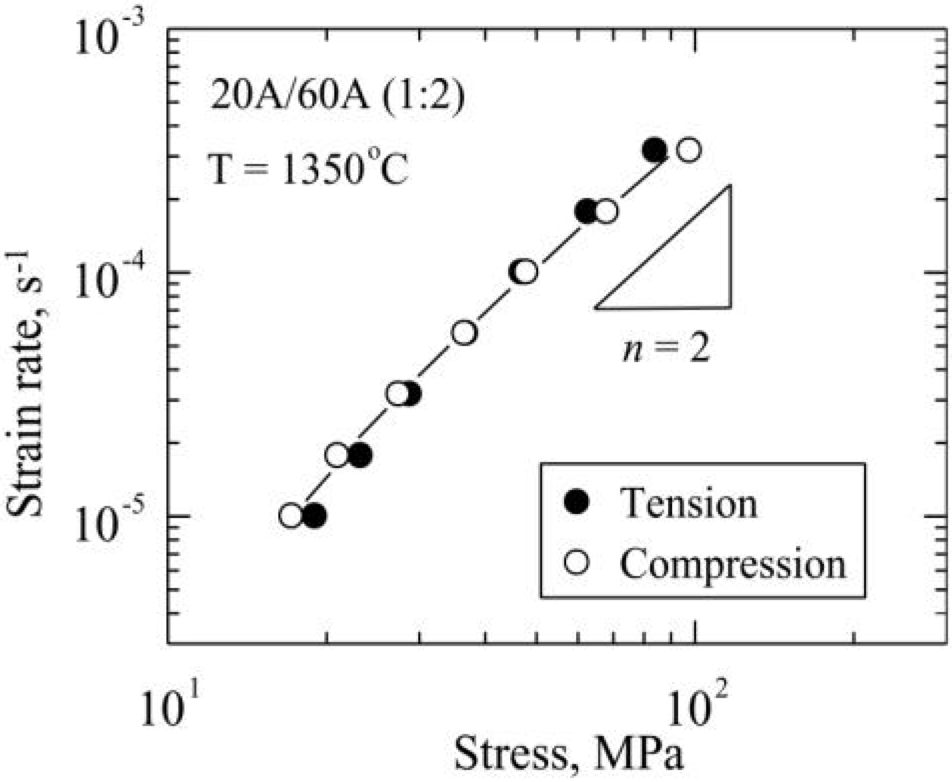

20A/60A (1:2)
T = 1350°C
n = 2
Tension
Compression
Strain rate, s-1
Stress, MPa
10-3
10-4
10-5
10¹
10²

(c)

Figure 6.6

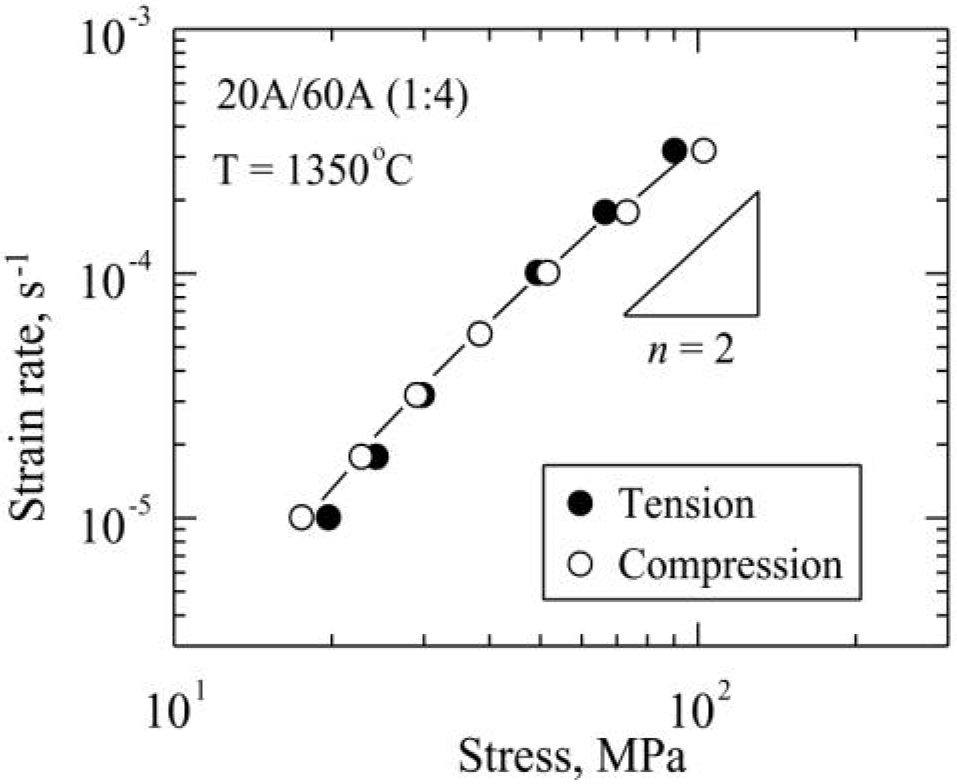
20A/60A (1:4)
T = 1350°C
$n = 2$
● Tension
○ Compression
Strain rate, s^{-1}
10^{-3}
10^{-4}
10^{-5}
10^{1}
10^{2}
Stress, MPa

(d)

Figure 6.6

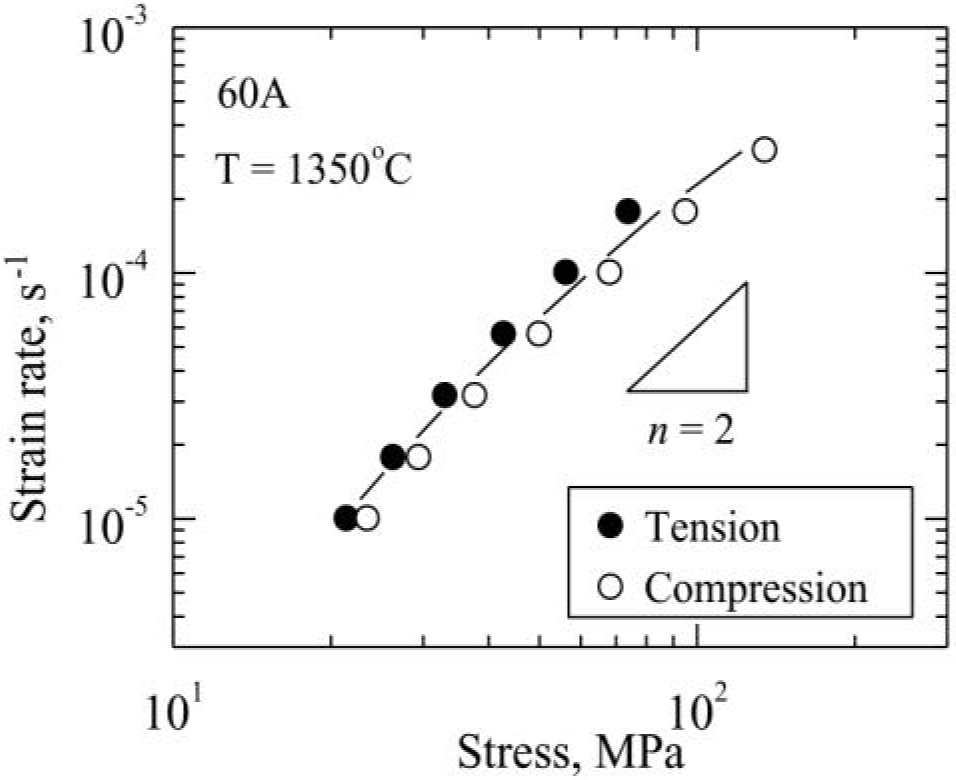

(e)

Figure 6.6 Comparisons between tensile and compression SRC tests: (a) 20A; (b) 20A/60A (1:1); (c) 20A/60A (1:2); (d) 20A/60A (1:4); (e) 60A.

Following SRC testing, elongation-to-failure tests were conducted on 20A, 20A/60A (1:1), and 20A/60A (1:2) specimens. The elongation-to-failures, e_f, of the 20A, 20A/60A (1:1), and 20A/60A (1:2), are 148%, 84%, and 59%, including both the strains from elongation-to-failure testing and SRC testing. If the engineering strain during the SRC testing is deducted, the corresponding elongation-to-failures of the 20A, 20A/60A (1:1), and 20A/60A (1:2), are about 132%, 68%, and 43%. The elongation-to-failure increases with the overall volume fraction of Y-TZP. Figure 6.7 illustrates the 20A/60A (1:1) specimen before and after elongation-to-failure testing. As can be seen, the gage section is uniform and no necking is observed after superplastic deformation.

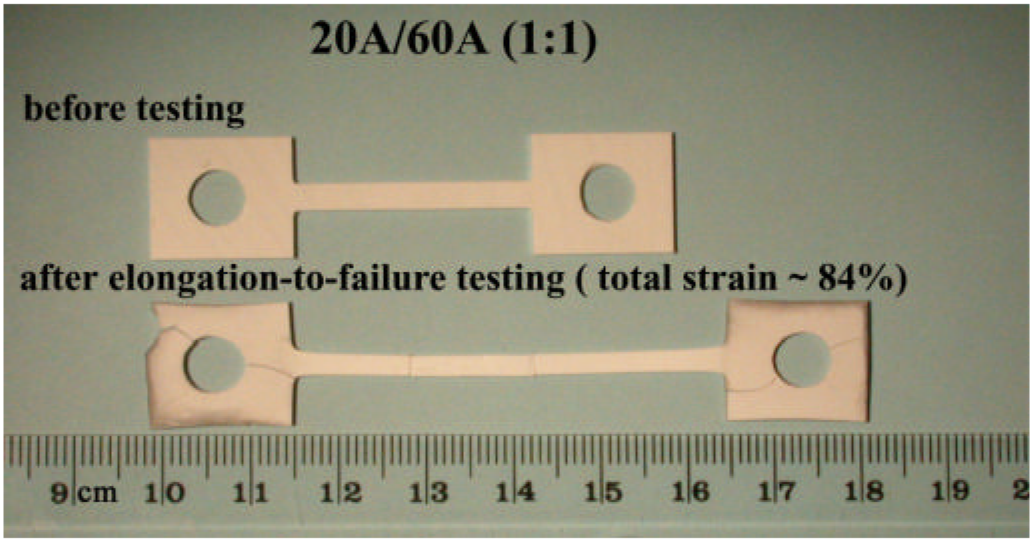

Figure 6.7 Illustration of 20A/60A (1:1) specimen before and after an elongation-to-failure testing. The elongation-to-failure is 84%.

Figure 6.8 shows a representative tensile SRC testing followed by an elongation-to-failure test for the 20A particulate composite. For the elongation-to-failure test, the true strain rate is 1.00 × 10^{-4} s^{-1}. An increase in flow stress is observed, indicating that strain hardening occurred during the elongation-to-failure testing.

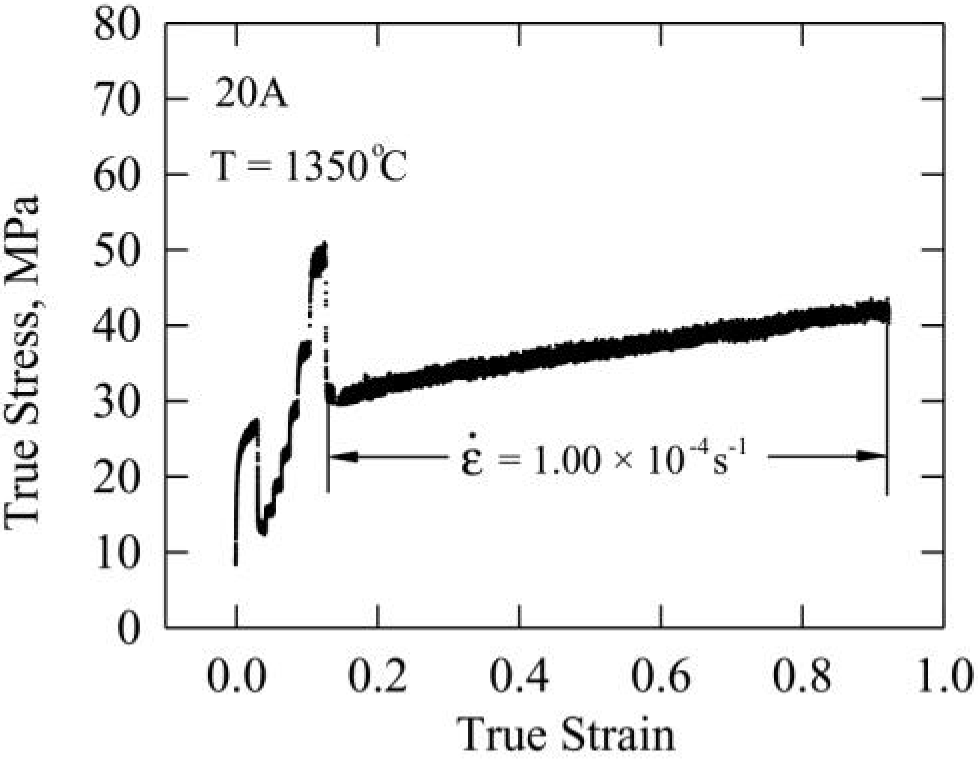

Figure 6.8 Tensile SRC test followed by elongation-to-failure test for 20A particulate composites. The true strain rate for the elongation-to-failure test is 1.00 × 10^{-4} s^{-1}.

6.3 DISCUSSION

6.3.1 High-Temperature Deformation

For Al_2O_3/Y-TZP particulate composites tested in tension and compression, most of previous studies have indicated that the stress exponents were about 2 over a large range of compositions (0 - 80 wt% Al_2O_3), strain rates (10^{-7} - 10^{-2} s^{-1}), and temperatures (1250 - 1650^{o}C) [8,11,20]. A previous result that indicated lower values of stress exponent (n ~ 1.2, at 1400^{o}C) in compression are likely due to the relatively high values and narrow range of strain rates at which those tests were conducted [9]. The current studies on Al_2O_3/Y-TZP particulate composites and particulate laminates conducted in tension consistently indicated that stress exponents were approximately equal to 2 at 1350^{o}C.

Owen *et al.* have reported that there was no significant difference in the stress necessary to deform 27.3 vol% Al_2O_3/Y-TZP particulate composites at a given strain rate in tension as compared to compression [65]. Similarly, the current study of both Al_2O_3/Y-TZP particulate composites and particulate laminates over a large range of compositions indicated very good agreement between the data in tension and in compression, as shown in Figure 6.6, suggesting that the deformation mechanisms are similar in tension and compression. One common thing between the current study and Owen *et al.* study is that very little concurrent grain growth and very little cavitation are observed during the tests. Therefore, stress state (*i.e.* compression or tension) does not affect the high-temperature deformation of Al_2O_3/Y-TZP particulate composites and particulate laminates when the microstructure is stable.

6.3.2 Superplastic Deformation

Previous studies have shown that hot-pressed Al_2O_3/Y-TZP particulate composites exhibit a large elongation-to-failure at 1450 - 1600°C, especially with high Y-TZP contents [20]. In our study, the samples were pressureless sintered which resulted in slightly more residual porosity than materials used in previous studies that were hot-pressed. Additionally, in our study, the elongation-to-failure testing was conducted at a lower temperature of 1350°C to minimize changes in microstructure during testing. Despite these differences which should reduce the elongation-to-failure, our results are similar to that obtained in previous studies. For example, Wakai *et al.* demonstrated that hot-pressed particulate composite, consisting of 27.3 vol% Al_2O_3 and the balance Y-TZP, had a superplastic elongation of 146% at 1450°C at an initial strain rate of 2.78×10^{-4}. In our study, 20A particulate shows a maximum elongation of ~ 148% after the elongation-to-failure testing at 1350°C at a true strain rate of 1.00×10^{-4} s^{-1}. The major reason that our specimens with lower density and temperature still exhibited high elongation-to-failure can be attributed to the much finer initial grain size used in the current study compared to that in Wakai *et al.* [20]. Previous studies showed that the tensile ductility of superplastic ceramics is limited by cavitation [38,51]. The cavities develop as a direct consequence of the applied stress so that higher stress levels lead to higher levels of internal cavitation [55]. Because flow stress increases with grain size, a critical grain size exists above which the cohesive strength of grain boundary is exceeded, resulting in cavitation and an eventual crack. Thus, superplasticity of ceramics increases with decreasing grain size. In the case of our specimens, the roles of fine grain size compensated the adverse effect of lower density so that similar superplasticity was observed for Al_2O_3/Y-TZP particulate composites.

In addition, superplastic behaviors of Al_2O_3/Y-TZP particulate laminates in the current study have been also compared to Al_2O_3/Y-TZP particulate composites in the previous studies. The current study showed that 20A/60A (1:2), with 46.7 vol% Al_2O_3, had an elongation-to-failure of 59% at 1350^{o}C at a true strain rate of 1.00×10^{-4} s^{-1}. For the Al_2O_3/Y-TZP particulate composites with similar composition, Wakai *et al.* showed an elongation-to-failure of ~ 100% at 1450^{o}C at an initial strain rate of 2.78×10^{-4} s^{-1} for 50 vol% Al_2O_3/Y-TZP particulate composite [20]. As discussed before, lower temperature and more residual porosity in the current study should not significantly reduce the elongation-to-failure of 20A/60A (1:2) laminate. The major reason that 20A/60A (1:2) particulate laminate has a lower elongation-to-failure than 50 vol% Al_2O_3/Y-TZP particulate composite may be attributed to constraint in the particulate laminates. As mentioned in Chapter 5, in the particulate laminates, the hard layer containing more Al_2O_3 imposed constraint on the deformation of the soft layer containing more Y-TZP. Thus, an in-plane tensile stress results in the hard layer and the total stress in the hard layer is equal to $s + \Delta s$, where Δs comes from constraint, as shown in Figure 6.9. As a result, in the hard layer, the increase in stress from constraint enhances cavitation, which limits the elongation-to-failure of particulate laminates.

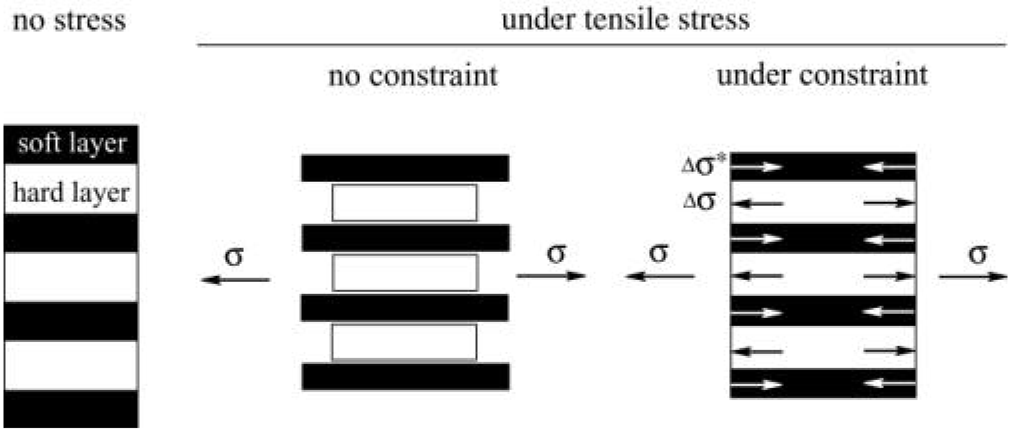

Figure 6.9 Illustration of the effect of constraint on the particulate laminates.

6.3.3 Cavitation and Grain Growth

Both cavitation and grain growth occurred during superplastic deformation. The former should cause strain softening (*i.e.* negative slope for the flow stress curves), while the latter should lead to strain hardening (*i.e.* positive slope for the flow stress curves). In a previous study, strain softening was observed in the 27.3 vol% Al_2O_3/Y-TZP particulate composite at 1350°C at an initial strain rate of 5.56 × 10^{-4} s^{-1} [8]. In the current study, for similar material, *i.e.* 20A particulate composite, strain hardening occurred at 1350°C at a true strain rate of 1.00 × 10^{-4} s^{-1}, as shown in Figure 6.8. The difference between the current study and previous study may result from the following two reasons. Firstly, the degree of strain softening decreased with the reduction of initial strain rate [8,20]. Secondly, a much finer initial grain size was used in the current study, which may accelerate grain growth during superplastic deformation.

Figure 6.10 shows the portion of the test corresponding to the SRC test for the 20A and indicates a 3 *MPa* strengthening at a total true strain of 0.14. This strengthening results from grain growth. Figure 6.11 shows that the flow stress exhibits a nearly linear increase with increasing strain during the portion of the test corresponding to the elongation-to-failure test for the 20A. Assuming that the linear relationship is satisfied over the whole range of strain, a strengthening of 17 *MPa* is expected during the portion of the test corresponding to elongation-to-failure testing. However, as shown in Figure 6.11, the observed strengthening of

12 *MPa* is lower than the calculated value of 17 *MPa*. The discrepancy is likely the result of cavitation.

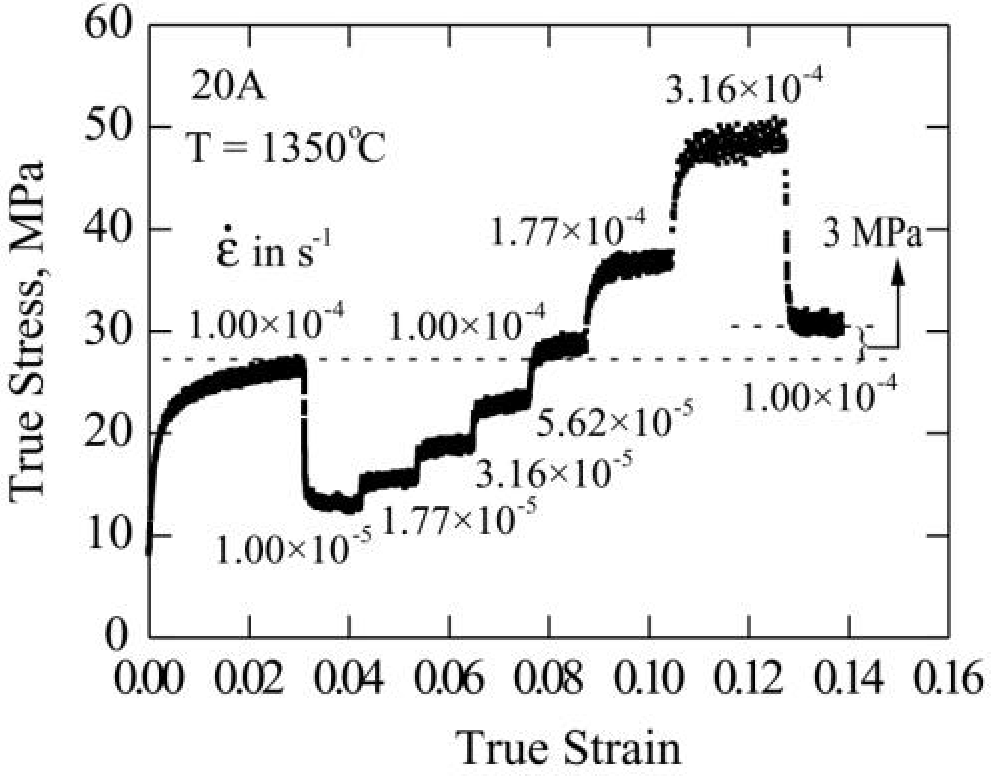

Figure 6.10 True stress versus true strain for 20A particulate composite during the portion of the test corresponding to tensile SRC testing.

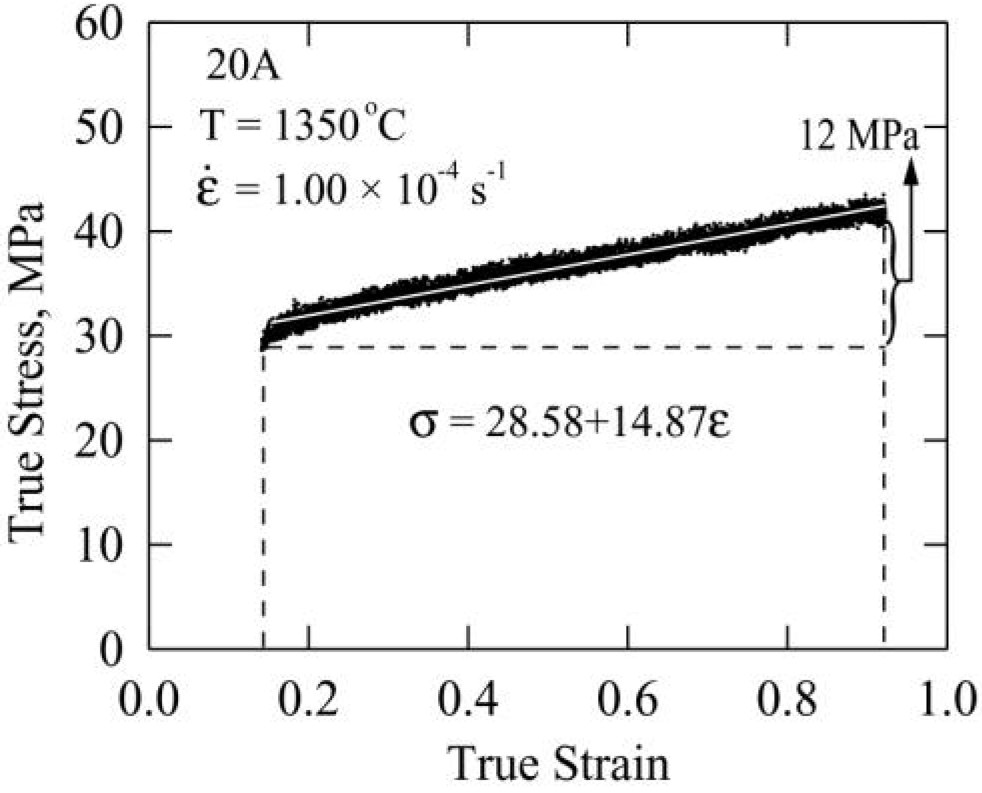

Figure 6.11 True stress versus true strain for 20A particulate composite during the portion of the test corresponding to elongation-to-failure testing.

6.3.3.1 Cavitation

Cavitation is a common phenomenon accompanying plastic deformation of ceramics at high temperature. The microstructure of 60A layer in the 20A/60A (1:2) particulate laminate after the elongation-to-failure testing at 1350^{o}C is shown in Figure 6.12, where the cavities are apparent. Cavities link and coalesce to form cracks that may finally lead to fracture.

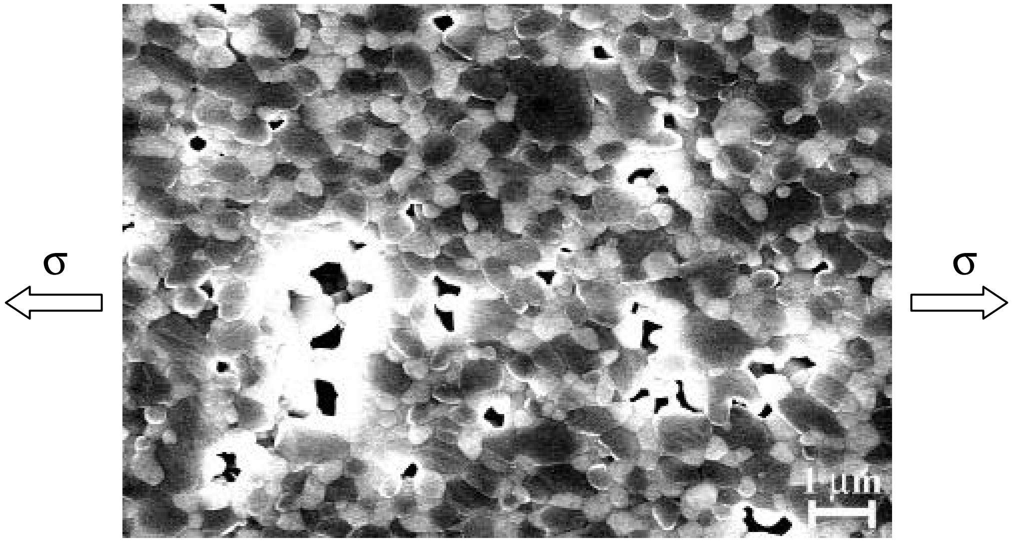

Figure 6.12 Microstructure of 60A layer in the 20A/60A (1:2) specimen after elongation-failure testing at 1350^{o}C with $\dot{e}$ = 1.00 × 10^{-4} s^{-1} and $e_f = 59\%$, showing the presence of cavities.

For the Al_2O_3/Y-TZP particulate composites and particulate laminates, the density loss during the tensile SRC testing and elongation-to-failure testing indicates that cavitation volume fraction increases with strain. In Figure 6.13, the cavitation volume fraction, C_v, is plotted against true strain. Assuming an exponential increase of cavitation volume fraction with true strain, the data are evaluated on the basis of the following equation:

$$C_v = A\exp(Be) \tag{6.1}$$

where e is the true strain, and A and B are constants [131]. Theoretically, the flow stress during testing should be corrected by considering the effect of cavitation, *i.e.*

$$s_{correct} = s \times \frac{A}{A(1-C_V)} \tag{6.2}$$

where A is the area of the specimen. Note, the cavitation volume fraction is assumed to be equal to the cavitation area fraction [132]. For the tensile SRC testing, $\frac{|s_{correct} - s|}{s} < 1\%$, since $C_v < 1\%$. Because the difference of less than 1% is very small in the log-log scale plots, the effect of the cavitation was neglected in Figure 6.6.

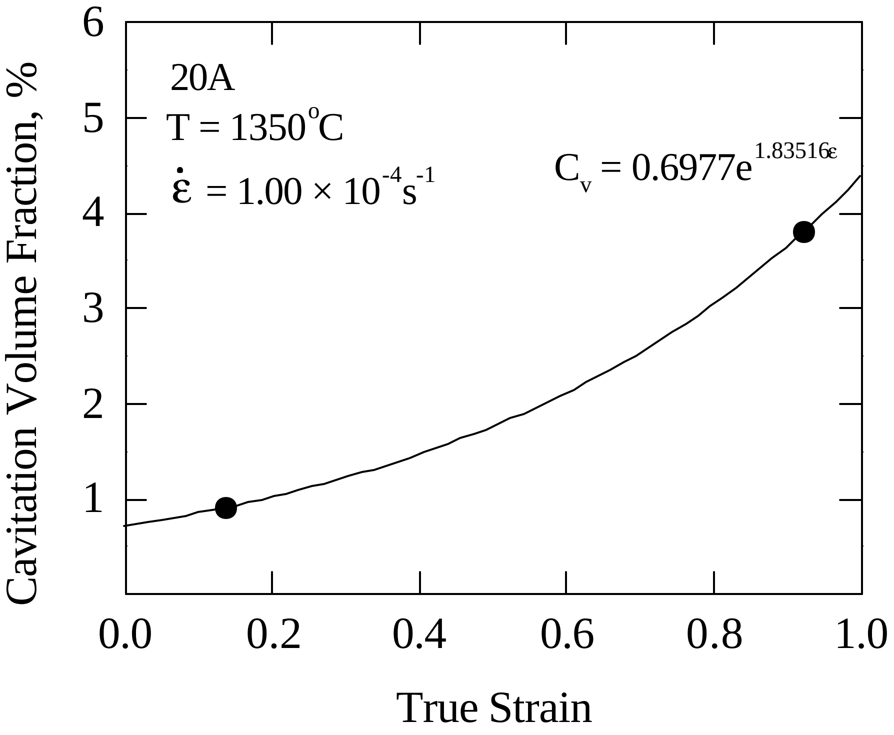

Figure 6.13 Increase in cavitation volume fraction with strain.

6.3.3.2 Grain size dependence

For Al_2O_3/Y-TZP particulate composites and laminates, significant grain growth occurred during the elongation-to-failure testing. The experimental data can be analyzed using the phenomenological equation [68]:

$$\dot{e} = A\left(\frac{s}{E}\right)^{n}\left(\frac{b}{d}\right)^{p}\exp\left(-\frac{Q_c}{RT}\right) \tag{6.3}$$

where s is the stress, E is the dynamic, unrelaxed Young's modulus, T is the absolute temperature, b is the magnitude of Burgers vector, d is the grain size, n is the stress exponent, p is the inverse grain size exponent, Q_c is the activation energy for creep, R is the gas constant, and A is a material constant. In the current study, for the portion of the test corresponding to elongation-to-failure test, true strain rate is constant (*i.e.* $\dot{e}$ = 1.00 × 10^{-4} s^{-1}). As discussed before, the stress exponents of Al_2O_3/Y-TZP particulate composites based on the SRC tests were approximately 2. Therefore, the flow stress is proportional to the grain size raised to the $^{p}\!/_{2}$ power, *i.e.*

$$s \propto d^{\,p/2} \tag{6.4}$$

To evaluate grain size dependence, Table 6.3 summarizes the flow stresses and grain sizes for the 20A at the beginning and the end of elongation-to-failure testing, corresponding to a true strain of $e = 0.14$ and $e = 0.92$, respectively (see

Figure 6.11). The flow stresses, $s_{correct}$, were calculated using Equation 6.2. The inverse grain size exponent, p, was then determined to be 3.1 using the relation

$$\frac{s_{correct[e=0.14]}}{s_{correct[e=0.92]}} = \left(\frac{\bar{d}_{Y-TZP\,[e=0.14]}}{\bar{d}_{Y-TZP\,[e=0.92]}} \right)^{p/2} \tag{6.5}$$

Because Y-TZP was the major phase in the 20A, only the grain sizes of Y-TZP were considered. This result, $p = 3.1$, together with $n = 2$, lead to $s \propto d^{1.5}$. Previously, Nieh *et al.* have studied the effect of grain size on the superplastic flow in 27.3 vol% Al_2O_3/Y-TZP. Their results indicated that the flow stress at a constant true strain rate and at a given strain was proportional to the grain size raised to a 0.75 power, *i.e.* $s \propto d^{0.75}$, with $p = 1.5$ [21,58]. By contrast, the 20A particulate composite in our study showed a stronger grain-size dependence. The following reasons may explain the difference between our study and Nieh *et al.* study. Firstly, Y-TZP has a stronger grain-size dependence than Al_2O_3/Y-TZP particulate composites ($s \propto d^2$ for Y-TZP versus $s \propto d^{0.75}$ for 27.3 vol% Al_2O_3/Y-TZP) [30]; the 20A used in our study contained more Y-TZP than the 27.3 vol% Al_2O_3/Y-TZP used in the Nieh *et al.* study. Secondly, the test technique was different. In our study, the grain size was constant and the influence of dynamic grain growth increased with strain was measured; in the Nieh *et al.* study, the true strain was held constant and the flow stress was measured in samples with different initial grain sizes. Thus, both dynamic grain growth and the change of the initial grain size should be considered to evaluate the exact value of p [57]. However, the effect of dynamic grain growth was not considered in the analyses of grain-size dependence for 27.3 vol% Al_2O_3/Y-TZP by Nieh *et al.* [58].

Table 6.3 Cavitation volume fractions, flow stresses, and grain sizes during the elongation-to-failure testing.

e	C_v (%)	s (MPa)	$s_{correct}$ (MPa)	$\bar{d}_{Y-TZP}$ (mm)
0.14	0.9	30	30.3	0.34
0.92	3.8	42	43.7	0.43

6.3.4 Models for Deformation Behavior

Previously, we found that the deformation behavior of Al_2O_3/Y-TZP particulate composites and particulate laminates in compression could be modeled using a constrained isostrain model, *i.e.*

$$s_c = (V_1K_1 + V_2K_2)\dot{e}_c^{1/2} \tag{6.6}$$

Since samples tested in tension and compression have similar flow behaviors, the constrained isostrain model can also predict the behaviors of particulate laminates in tension, as shown in Figure 6.14, where $K_1 = 2661.2$ and $K_2 = 5538.5$ for 20A and 60A, respectively. It can be seen that the isostress model did not fit the experiment data well.

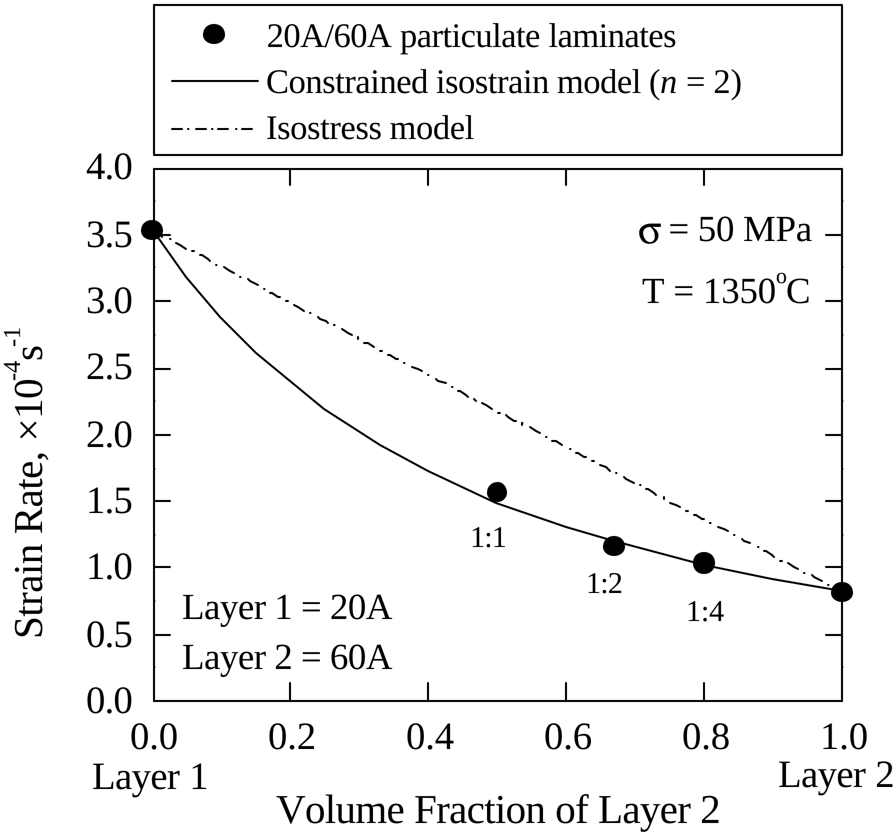

Figure 6.14 Comparison between the models and experimental data from 20A/60A particulate laminates during the tensile SRC test.

6.4 CONCLUSIONS

The high-temperature deformation behaviors of 20A, 60A particulate composites, and 20A/60A particulate laminates were fabricated by tapecasting, lamination and sintering. Tensile SRC tests were conducted at 1350^{o}C with very small changes in microstructure. The high-temperature deformation behaviors of Al_2O_3/Y-TZP particulate composites and laminates tested in tension were similar to that in compression, indicating there is a similar deformation mechanism in tension and compression. The stress exponents were measured to be approximately 2 for both Al_2O_3/Y-TZP particulate composites and particulate laminates tested in tension. Elongation-to-failure tests were also performed at 1350^{o}C. Both grain growth and cavitation occurred during testing. After correcting for cavitation, the flow stress at a constant true strain rate ($\dot{e}$ = 1.00 × 10^{-4}) was found to be proportional to the grain size raised to 1.5 power. Although our specimens had lower density and testing temperature than previous studies, good superplasticity was still observed due to the much finer grain size used. The elongation-to-failures of 20A, 20A/60A (1:1), and 20A/60A (1:2) were 148%, 84%, and 59% at 1350^{o}C at a true strain rate of 1.00 × 10^{-4} s^{-1}. The particulate laminates showed a lower elongation-to-failure than particulate composites with similar composition due to constraint. A constrained isostrain model with $n = 2$ provides a better prediction of the flow behavior for Al_2O_3/Y-TZP particulate laminates tested in tension.

Chapter 7

Conclusions

In the current study, Al_2O_3/Y-TZP particulate composites consisting of 20 to 80 vol% Al_2O_3 and Al_2O_3/Y-TZP particulate laminates with varying thickness ratios were fabricated by tapecasting, lamination, and sintering. Compression strain-rate-change (SRC) tests and tensile SRC tests were conducted. High-temperature behaviors of Al_2O_3/Y-TZP particulate composites and particulate laminates were systematically studied under conditions where changes in microstructure during testing were deliberately minimized. In addition, a limited number of elongation-to-failure tests were conducted, allowing superplastic behavior of Al_2O_3/Y-TZP particulate composites and laminates to be investigated. The microstructures of specimens before and after testing were characterized.

TEM micrographs indicated that the grain boundaries and triple junctions of the Al_2O_3/Y-TZP particulate composites examined in the current study were likely free of glass phase which has been observed in some previous studies and which can make interpretation of deformation mechanisms more difficult. SEM micrographs showed that fine-grained microstructures were maintained during compression SRC testing. The results of compression SRC tests showed that stress exponents of Al_2O_3/Y-TZP particulate composites were approximately 2 at high Al_2O_3 contents and high stresses and approximately 3 at low Al_2O_3 contents and low stresses. The flow stresses of particulate composites increased with grain size and volume fraction of Al_2O_3. Good qualitative agreement between the experimental data and a constrained isostrain model, for which the stress exponents of the constituent Al_2O_3 and Y-TZP phases were constrained to physically realistic values, *i.e.* $n = 2$, was observed. This model successfully predicts the difference in flow stress and strain rates with different compositions, but similar grain size.

The results of compression SRC tests showed that stress exponents of Al_2O_3/Y-TZP particulate laminates were also approximately 2 at high stress with a transition to higher values as strain rate was decreased, indicating there is a similar deformation mechanism between particulate composites and particulate laminates. The deformation behaviors of particulate laminates were influenced by the overall compositions and the constraint imposed by the hard layer on the soft layer. Particulate laminates were stronger than particulate composites with the same overall composition, especially when the compositions of the layers in the laminates were markedly different. The composition of the hard layer dominated the observed behaviors of the laminates during the high-temperature deformation. Laminates in the isostrain orientation were only slightly stronger than laminates in the isostress orientation because constraint dictates that the strains in each layer must be constant. As a result, a constrained isostrain model with $n = 2$ provides a good prediction of the flow behavior for particulate laminates tested in both the isostrain and isostress orientation.

SEM micrographs showed that there was no significant grain growth or cavitation during tensile SRC testing. The results of the tensile SRC tests showed that the stress exponents of both Al_2O_3/Y-TZP particulate composites and particulates laminates tested were approximately 2. There was little difference in high-temperature behavior between Al_2O_3/Y-TZP particulate composites (or particulate laminates) tested in tension and compression, indicating that the deformation mechanisms are similar in tension and compression. Both grain growth and cavitation occurred during the elongation-to-failure testing. The results of elongation-to-failure tests showed that flow stress had a strong grain-size dependence, *i.e.* $s \propto d^{1.5}$. The elongation-to-failures of 20A, 20/60A (1:1), and 20A/60A (1:2) were measured to be 148%, 84%, and 59% at 1350^{o}C at a true strain rate of 1.00×10^{-4} s^{-1}. The elongation-to-failure increased with volume fraction of Y-TZP. Comparing with previous studies, we can conclude that increasing density and decreasing initial grain size are effective methods for enhancing superplastic formability of ceramics. Particulate laminates had a lower elongation-to-failure than particulate composites with the similar composition due to the constraint. In addition, a constrained isostrain model with $n = 2$ provides a good prediction of the flow behavior for Al_2O_3/Y-TZP particulate laminates tested in tension.

Because stress exponents were approximately 2 for both Al_2O_3/Y-TZP particulate composites and particulate laminates tested in compression and tension; plus, the grain shapes remained equiaxed during the deformation, even after elongation-to-failure test. Thus, it is believed that grain-boundary sliding dominates the high-temperature deformation of Al_2O_3/Y-TZP particulate composites and particulate laminates.

Bibliography

[1] Lenoe EM. Recent Accomplishments and Recent Needs in Structural Ceramics, in *Ceramics for High-Performance Applications-III: Reliability*, ed. Lenoe EM, Katz RN, and Burke JL. Plenum Press, 3-18.

[2] Allor RL, and Jahanmir S. Current Problems and Future Directions for Ceramic Machining, *Am Ceram Soc Bull*, **75**, 1996, 40-43.

[3] Rice RW. Hot-Working of Oxides, in *High Temperature Oxides*, ed. Alper AM. Academic Press, New York, 1970, 235-80.

[4] Edington JW, Melton KN, and Cutler CP. Superplasticity, in *Progress in Materials Science*, Vol. 21, 1976, 61-170.

[5] Tsuzuku T, Takahashi A, and Sakamoto A. Application of Superplastic Forming For Aerospace Components, in *Superplasticity in Advanced Materials*, ed. Hori S, Tokizane M, and Furushiro N. The Japan Society for Research on Superplasticity, 1991, 611-20.

[6] Wakai F, Sakaguchi S, and Matsuno Y. Superplasticity of Yttria-Stablized Tetragonal ZrO_2 Polycrystals, *Adv Ceram Mater*, **1**, 1986, 259-63.

[7] Nieh TG, McNally CM, and Wadsworth J. Superplastic Properties of a Fine-Grained Yttria-Stabilized Tetragonal Polycrystal of Zirconia, *Scripta Metall*, **22**, 1988, 1297-300.

[8] Wakai F, and Kato H. Superplasticity of TZP/Al_2O_3 Composite, *Adv Ceram Mater*, **3**, 1988, 71-76.

[9] Wakai F, Kato H, Sakaguchi S, and Murayama N. Compressive Deformation of Y_2O_3-Stablized ZrO_2/Al_2O_3 Composite, *J Ceram Soc Jpn*, **94**, 1986, 1017-20.

[10] Nieh TG, and Oliver WC. Superplasticity of a Nickel Silicide, Ni_3Si, *Scripta Metall*, **23**, 1989, 851-54.

[11] Nieh TG, McNally CM, and Wadsworth J. Superplastic Behavior of a 20% Al_2O_3/YTZ Ceramic Composite, *Scripta Metall*, **23**, 1989, 457-60.

[12] Xue LA, and Raj R. Superplastic Deformation of Zinc-Sulfide Near Its Transformation Temperature (1020^{o}C), *J Am Ceram Soc*, **72**, 1989, 1792-96.

[13] Nieh TG, and Wadsworth J. Superplastic Behavior of a Fine-Grained, Yttria-Stabilized, Tetragonal Zirconia Polycrystal (Y-TZP), *Acta Metall Mater*, **38**, 1990, 1121-33.

[14] Wakai F, Kodama Y, Sakaguchi S, and Nonami T. Superplasticity of Hot Isostatically Pressed Hydroxyapatite, *J Am Ceram Soc*, **73**, 1990, 457-60.

[15] Wakai F, Kodama Y, Sakaguchi S, Murayama N, Izaki K, and Niihara K. A Superplastic Covalent Crystal Composite, *Nature*, **344**, 1990, 421-23.

[16] Nieh TG, Wadsworth J, and Sherby OD. Superplastic Behavior in Ceramics, Ceramic Composites, Metal Matrix Composites, and Intermetallics, in *Superplastic in Aerospace II*, ed. McNelley TR, Heikkenen CH. The Minerals, Metals and Materials Society, 1990, 19-32.

[17] Blandin JJ, Varloteaux A, and Suery M. Superplastic Behavior of Fine-grained Zirconia, in *Superplasticity in Advanced Materials*, ed. Hori S, Tokizane M, and Furushiro N. The Japan Society for Research on Superplasticity, 1991, 263-68.

[18] Gruffel P, Carry C, and Mocellin A. Effect of Testing Conditions on Superplastic Creep of Alumina Doped With Ti and Y, in *Science of Ceramics*, ed. Taylor D. The 14th International Conference on Science of Ceramics, 1987, 587-92.

[19] Wang JG, and Raj R. Mechanism of Superplastic Flow in a Fine-Grained Ceramic Containing Some Liquid-Phase, *J Am Ceram Soc*, **67**, 1984, 399-409.

[20] Wakai F, Kodama Y, Sakaguchi S, Murayama N, Kato H, and Nagano T. Superplastic Deformation of ZrO_2/Al_2O_3 Duplex Composites, in *Superplasticity*, ed. Kobayashi M and Wakai F. MRS International Meeting on Advanced Materials, Vol. 7, 259-66.

[21] Nieh TG, and Wadsworth J. Superplasticity in Fine-Grained 20% Al_2O_3/YTZ Composite, *Acta Metall Mater*, **39**, 1991, 3037-45.

[22] Okada K, Yoshizawa Y, and Sakuma T. High-Temperature Deformation in Al_2O_3-ZrO_2, in *Superplasticity in Advanced Materials*, ed. Hori S, Tokizane M, and Furushiro N. The Japan Society for Research on Superplasticity, 1991, 227-32.

[23] Sosa SS, and Langdon TG. Creep Behavior of a Superplastic Y-TZP/Al_2O_3 Composite: An Examination of the Possibility for Diffusion Creep, in *Superplasticity-Current Status and Future Potential*, ed. Berbon PB, Berbon MZ, Sakuma T, and Langdon TG. Materials Research Society Symposium Proceeding, Vol. 601, 2000, 111-16.

[24] Wakai F, Kodama Y, Sakaguchi S, Murayama N, Izaki K, and Niihara K. Superplasticity of Non-Oxide Ceramics, in *Superplasticity in Metals, Ceramics, and Intermetallics*, ed. Mayo MJ, Kobayashi M, and Wadsworth J. Materials Research Society Symposium Proceedings, Vol. 196, 1990, 349-58.

[25] Kajihara K, Yoshizawa Y, and Sakuma T. Superplasticity in SiO_2-Containing Tetragonal Zirconia Polycrystal, *Scripta Metall Mater*, **28**, 1993, 559-62.

[26] Kellett BJ, and Lange FF. Hot-Forging Characteristics of Fine-Grained ZrO_2 and Al_2O_3/ZrO_2 Ceramics, *J Am Ceram Soc*, **69**, 1986, C172-73.

[27] Kellett BJ, and Lange FF. Hot-Forging Characteristics of Transformation-Toughened Al_2O_3/ZrO_2 Composites, *J Mater Res*, **3**, 1988, 545-51.

[28] Carry C, and Mocellin A. Examples of Superplastic Forming-Grained Al_2O_3 and ZrO_2 Ceramics, in *High Tech Ceramics*, ed. Vincenzini P. Elsevier Science Publishers B. V., 1987, 1043-52.

[29] Xin W, and Chen IW. Superplastic Bulging of Fine-Grained Zirconia, *J Am Ceram Soc*, **73**, 1990, 746-49.

[30] Nieh TG, Wadsworth J, and Sherby OD. Superplasticity in Metals and Ceramics, Cambridge University Press, 1997.

[31] Nieh TG, Wadsworth J, and Wakai F. Recent Advances in Superplastic Ceramics and Ceramic Composites, *Int Mater Rev*, **36**, 1991, 146-61.

[32] Langdon TG. Superplastic Ceramic-An Overview, in *Superplastic in Aerospace II*, ed. McNelley TR, Heikkenen CH. The Minerals, Metals and Materials Society, 1990, 4-18.

[33] Chokshi AH, Schissler DJ, Nieh TG, and Wadsworth J. A Comparative Study of Superplastic Deformation and Cavitation Failure in a Yttria Stabilized Zirconia and a Zirconia Alumina Composite, in *Superplasticity in Metals, Ceramics, and Intermetallics*, ed. Mayo MJ, Kobayashi M, and Wadsworth J. Materials Research Society Symposium Proceedings, Vol. 196, 1990, 379-84.

[34] Nieh TG, and Wadsworth J. Superplastic Deformation Mechanisms in A Fine-grained, Yttria-Stabilized Tetragonal Zirconia Polycrystal (Y-TZP), in *Superplasticity in Metals, Ceramics, and Intermetallics*, ed. Mayo MJ, Kobayashi M, and Wadsworth J. Materials Research Society Symposium Proceedings, Vol. 196, 1990, 331-36.

[35] Nieh TG, Tomasello CM, and Wadsworth J. Dynamic Grain Growth in Superplastic Y-TZP and Al_2O_3/YTZ, in *Superplasticity in Metals,*

Ceramics, and Intermetallics, ed. Mayo MJ, Kobayashi M, and Wadsworth J. Materials Research Society Symposium Proceedings, Vol. 196, 1990, 343-47.

[36] Yoshizawa Y, and Sakuma T. The Strain-Enhanced Grain Growth in Tetragonal Zirconia Polycrystal During Superplastic Deformation, in *Superplasticity in Advanced Materials*, ed. Hori S, Tokizane M, and Furushiro N. The Japan Society for Research on Superplasticity, 1991, 251-56.

[37] Nieh TG, and Wadsworth J. Dynamic Grain Growth During Superplastic Deformation of Yttria-Stabilized Tetragonal Zirconia Polycrystals, *J Am Ceram Soc*, **72**, 1989, 1469-72.

[38] Schissler DJ, Chokshi AH, Nieh TG, and Wadsworth J. Microstructural Aspects of Superplastic Tensile Deformation and Cavitation Failure in a Fine-Grained Yttria Stabilized Tetragonal Zirconia, *Acta Metall Mater*, **39**, 1991, 3227-36.

[39] Duclos R, and Crampon J. High-Temperature Deformation of a Fine-Grained Zirconia, *J Mater Sci Lett*, **6**, 1987, 905-08.

[40] Duclos R, Crampon J, Bigay Y, Cales B, and Torre JP. High Temperature Deformation of Yttria Partially Satbilized Zriconia Polycrystals, in *Science of Ceramics*, ed. Taylor D. The 14th International Conference on Science of Ceramics, 1987, 581-86.

[41] Duclos R, Crampon J, and Amana B. Structural and Topological Study of Superplasticity in Zirconia Polycrystals, *Acta Metall*, **37**, 1989, 877-83.

[42] Raj R. Mechanisms of Superplastic Deformation in Ceramics, in *Superplasticity and Superplastic Forming*, ed. Hamilton CH and Paton NE. The Minerals, Metals and Materials Society, Warrendale, 1988, 583.

[43] Kottada RS, and Chokshi AH. The High Temperature Tensile and Compressive Deformation Characteristics of Magnesia Doped Alumina, *Acta Mater*, **48**, 2000, 3905-15.

[44] Nieh TG, Yaney DL, and Wadsworth J. Analysis of Grain Boundaries in a Fine-Grained, Superplastic, Yttria-Containing, Tetragonal Zirconia, *Scripta Metall*, **23**, 1989, 2007-11.

[45] Carry C. High Ductilities, Superplastic Behaviors and Associated Mechanisms in Fine Grained Ceramics, in *Superplasticity*, ed. Kobayashi M and Wakai F. MRS International Meeting on Advanced Materials, Vol. 7, 1989, 199-215.

[46] Chokshi AH. Superplasticity in Fine-Grained Ceramics and Ceramic Composites-Current Understanding and Future Prospects, *Mater Sci Eng*, **A166**, 1993, 119-33.

[47] Wang JG, and Raj R. Influence of Hydrostatic-Pressure and Humidity on Superplastic Ductility of 2 β-Spodumene Glass-Ceramics, *J Am Ceram Soc*, **67**, 1984, 385-90.

[48] Hermansson T, Swan H, and Dunlop G. The Role of the Intergranular Glassy Phase in the Superplastic Deformation of Y-TZP Zirconia, in *Euro-Ceramics, Vol. 3: Engineering Ceramics*, ed. With GD, Terpstra RA, and Metselaar R, 1989, 3.329-3.333.

[49] Hwang CMJ, and Chen IW. Effect of a Liquid Phase on Superplasticity of 2-mol%-Y_2O_3-Stabilized Tetragonal Zirconia Polycrystals, *J Am Ceram Soc*, **73**, 1990, 1626-32.

[50] Gust M, Goo G, Wolfenstine J, and Mecartney ML. Influence of Amorphous Grain Boundary Phases on the Superplastic Behavior of 3-mol%-Yttria-Stabilized Tetragonal Zirconia Polycrystals (3Y-TZP), *J Am Ceram Soc*, **76**, 1993, 1681-90.

[51] Chokshi AH, Nieh TG, and Wadsworth J. Role of Concurrent Cavitation in the Fracture of a Superplastic Zirconia Alumina Composite, *J Am Ceram Soc*, **74**, 1991, 869-73.

[52] Ma Y, and Langdon TG. An Investigation of the Mechanical Behavior of a Superplastic Yttria-Stabilized Zirconia, in *Superplasticity in Metals, Ceramics, and Intermetallics*, ed. Mayo MJ, Kobayashi M, and Wadsworth J. Materials Research Society Symposium Proceedings, Vol. 196, 1990, 325-30.

[53] Ma Y, and Langdon TG. A Critical Assessment of Flow and Cavity Formation in a Superplastic Yttria-Stabilized Zirconia, *Acta Metall Mater*, **42**, 1994, 2753-61.

[54] Tekeli S, and Davies TJ. Ductility Enhancement and Cavitation Behavior in Superplastic 3Y-TZP Tested at Changing Test Temperature, *J Mater Sci Lett*, **19**, 2000, 2007-10.

[55] Zhou M, Ma Y, and Langdon TG. A Quantitative Analysis of Cavity Formation in Superplastic Yttria-Stabilized Tetragonal Zirconia, in *Plastic Deformation of Ceramics*, ed. Bradt RC, Brookes CA, and Routbort JL. Plenum Press, 1995, 301-12.

[56] Chen IW, and Xue LA. Development of Superplastic Structural Ceramics, *J Am Ceram Soc*, **73**, 1990, 2585-609.

[57] Nieh TG, and Wadsworth J. Effect of Grain Size on Superplastic Behavior of Y-TZP, *Scripta Metall Mater*, **24**, 1990, 763-66.

[58] Nieh TG, and Wadsworth J. Effect of Grain Size on Superplastic Behavior of Al_2O_3-YTZ, *J Mater Res*, **5**, 1990, 2613-15.

[59] Xue LA, and Raj RS. Grain Growth in Superplastically Deformed Zinc-Sulfide Diamond Composites, *J Am Ceram Soc*, **74**, 1991, 1729-31.

[60] Yoon CK, and Chen IW. Superplastic Flow of Two-Phase Ceramics Containing Rigid Inclusions-Zirconia/Mullite Composites, *J Am Ceram Soc*, **73**, 1990, 1555-65.

[61] Venkatachari KR, and Raj R. Superplastic Flow in Fine-Grained Alumina, *J Am Ceram Soc*, **69**, 1986, 135-38.

[62] Xue LA, and Raj R. Effect of Diamond Dispersion on the Superplastic Rheology of Zinc-Sulfide, *J Am Ceram Soc*, **73**, 1990, 2213-16.

[63] Wakai F, Sakaguchi S, Kanayama K, Kato H, and Onishi H. Hot Work of Yttria-Stabilized Tetragonal ZrO_2 Polycrystals, in *Ceramic Materials and Components for Engines*, ed. Bunk W and Hausner H. Proceeding of the Second International Symposium, 1986, 315-22.

[64] Yoon KJ, Wiederhorn SM, and Luecke WE. Comparison of Tensile and Compressive Creep Behavior in Silicon Nitride, *J Am Ceram Soc*, **83**, 2000, 2017-22.

[65] Owen DM, and Chokshi AH. A Comparison of The Tensile and Compressive Creep Behavior of a Superplastic Yttria-Stablized Tetragonal Zirconia-20 wt% Alumina Composite, in *Superplasticity in Advanced Materials*, ed. Hori S, Tokizane M, and Furushiro N. The Japan Society for Research on Superplasticity, 1991, 215-20.

[66] Nauer M, and Carry C. Flow Behaviors at High Temperature of Yttria Doped Zirconia Polycrystals, in *Euro-Ceramics, Vol. 3: Engineering Ceramics*, ed. With GD, Tespstra RA, and Metselaar R, 1989, 3.323-3.328.

[67] Courtney TH. Mechanical Behavior Materials, McGraw-Hill, Inc., 1990.

[68] Sherby OD, and Burke PM. Mechanical Behavior of Crystalline Solids at Elevated Temperature, in *Progress in Materials Science*, Vol. 13, ed. Chalmers B and Hume-Rothery W. Pergamon Press, 1968, 325-90.

[69] Arzt E, Ashby MF, and Verrall RA. Interface Controlled Diffusional Creep, *Acta Metall*, **31**, 1983, 1977-89.

[70] Langdon TG. The Mechanical Properties of Superplastic Materials, *Metall Trans*, **A13**, 1982, 689-701.

[71] Charit I, and Chokshi AH. Experimental Evidence for Diffusion Creep in the Superplastic 3 mol% Yttria-Stabilized Tetragonal Zirconia, *Acta Mater*, **49**, 2001, 2239-49.

[72] Morita K, Hiraga K, and Sakka Y. Creep Deformation in a 3 mol% Y_2O_3-Stabilized Tetragonal Zirconia, in *Superplasticity-Current Status and Future Potential*, ed. Berbon PB, Berbon MZ, Sakuma T, and Langdon TG. Materials Research Society Symposium Proceeding, Vol. 601, 2000, 93-98.

[73] Chokshi AH. An Evaluation of the Grain-Boundary Sliding Contribution to Creep Deformation in Polycrystalline Alumina, *J Mater Sci*, **25**, 1990, 3221-28.

[74] Motohashi Y, Sekigami T, Sakuma T, and Ohmori M. On the Superplastic Deformation Modes of Y-TZP under Uniaxial Tension, in *Superplasticity in Advanced Materials*, ed. Hori S, Tokizane M, and Furushiro N. The Japan Society for Research on Superplasticity, 1991, 221-26.

[75] Furushiro N, Tanizawa T, Akashiro K, and Takeshita S. Grain Boundary Sliding during Superplastic Defromation in Ceramic Materials, in *Superplasticity in Advanced Materials*, ed. Hori S, Tokizane M, and Furushiro N. The Japan Society for Research on Superplasticity, 1991, 245-50.

[76] Arieli A, and Mukherjee AK. The Rate-Controlling Deformation Mechanisms in Superplasticity-a Critical Assessment, *Metall Trans*, **A13**, 1982, 717-32.

[77] Ball A, and Hutchison MM. Superplasticity in the Aluminum-Zinc Eutectoid, *Metal Sci J*, **3**, 1969, 1-7.

[78] Ashby MF, and Verrall RA. Diffusion-Accommodated Flow and Superplasticity, *Acta Metall*, **21**, 1973, 149-63.

[79] Tekeli S, and Davies TJ. A Comparative Study of Superplastic Deformation and Cavitation Behavior in 3 and 8 mol% Yttria-Stabilized Zirconia, *Mater Sci Eng*, **A297**, 2001, 168-75.

[80] Bravo-León A, Jiménez-Melendo M, Dominguez-Rodriguez A, and Chokshi AH. The Influence of Oxygen Partial Pressure on the Creep Characteristics of a Superplastic 4 mol% Yttria Partially-Stabilized Zirconia, *J Mater Sci Lett*, **13**, 1994, 1169-70.

[81] Wakai F, and Nagano T. Effects of Solute Ion and Grain Size on Superplasticity of ZrO_2 Polycrystals, *J Mater Sci*, **26**, 1991, 241-47.

[82] Owen DM, and Chokshi AH. The High Temperature Mechanical Characteristics of Superplastic 3 mol% Yttria Stabilized Zirconia, *Acta Mater*, **46**, 1998, 667-79.

[83] Jiménez-Melendo M, Dominguez-Rodriguez A, and Bravo-León A. Superplastic Flow of Fine-Grained Yttria-Stabilized Zirconia Polycrystals: Constitutive Equation and Deformation Mechanisms, *J Am Ceram Soc*, **81**, 1998, 2761-76.

[84] Owen DM, and Chokshi AH. Analysis of Deformation Mechanisms in Superplastic Yttria-Stabilized Tetragonal Zirconia, *Int J Plast*, **17**, 2001, 353-68.

[85] Hines JA, Ikuhara Y, Chokshi AH, and Sakuma T. The Influence of Trace Impurities on the Mechanical Characteristics of a Superplastic 2 mol% Yttria Stabilized Zirconia, *Acta Mater*, **46**, 1998, 5557-68.

[86] Bravo-León A, Jiménez-Melendo M, Dominguez-Rodriguez A, and Chokshi AH. The Role of a Threshold Stress in the Superplastic Deformation of Fine-Grained Yttria-Stabilized Zirconia Polycrystals, *Scripta Mater*, **34**, 1996, 1155-60.

[87] Dominguez-Rodriguez A, Bravo-León A, Ye JD, and Jiménez-Melendo M. Grain Size and Temperature Dependence of the Threshold Stress for Superplastic Deformation in Yttria-Stabilized Zirconia Polycrystals, *Mater Sci Eng*, **A247**, 1998, 97-101.

[88] Jiménez-Melendo M, and Dominguez-Rodriguez A. High Temperature Mechanical Characteristics of Superplastic Yttria-Stabilized Zirconia. An Examination of the Flow Process, *Acta Mater*, **48**, 2000, 3201-10.

[89] Dominguez-Rodriguez A, Gutierrez-Mora F, Jiménez-Melendo M, Routbort JL, and Chaim R. Current Understanding of Superplastic Deformation of Y-TZP and Its Application to Joining, *Mater Sci Eng*, **A302**, 2001, 154-61.

[90] Jiménez-Melendo M, and Dominguez-Rodriguez A. Like-Metal Superplasticity of Fine-Grained Y_2O_3-Stabilized Zirconia Ceramics, *Philos Mag*, **A79**, 1999, 1591-608.

[91] Jiménez-Melendo M, Dominguez-Rodriguez A, and Holgado-Salado M. Superplastic Characteristics of High Purity Yttria-Stabilized Zirconia Polycrystals, *Int J Plast*, **17**, 2001, 341-52.

[92] Berbon MZ, and Langdon TG. An Examination of the Flow Process in Superplastic Yttria-Stabilized Tetragonal Zirconia, *Acta Mater*, **47**, 1999, 2485-95.

[93] Berbon MZ, and Langdon TG. A Discussion of Flow Mechanisms in Superplastic Yttria-Stabilized Tetragonal Zirconia, in *Superplasticity-Current Status and Future Potential*, ed. Berbon PB, Berbon MZ, Sakuma T, and Langdon TG. Materials Research Society Symposium Proceeding, Vol. 601, 2000, 105-10.

[94] Chokshi AH. On the Emergence of New Surface Grains During Superplastic Deformation, *Scripta Mater*, **44**, 2001, 2611-15.

[95] Chokshi AH. Diffusion Creep in Oxide Ceramics, *J Euro Ceram Soc*, **22**, 2002, 2469-78.

[96] Chokshi AH. The Role of Diffusion Creep in the Superplastic Deformation of 3 mol% Yttria Stabilized Tetragonal Zirconia, *Scripta Mater*, **42**, 2000, 241-48.

[97] Wakai F, Kondo N, Ogawa H, Nagano T, and Tsurekawa S. Ceramics Superplasticity: Deformation Mechanisms and Microstructures, *Mater Charact*, **37**, 1996, 331-41.

[98] Wakai F, and Kondo N. Solution-Precipitation Creep Model For Superplastic Ceramics with Intergranular Liquid Film, in *Plastic Deformation of Ceramics*, ed. Bradt RC, Brookes CA, and Routbort JL. Plenum Press, 1995, 269-77.

[99] Langdon TG. The Characteristics of Superplastic-Like Flow in Ceramics, in *Plastic Deformation of Ceramics*, ed. Bradt RC, Brookes CA, and Routbort JL. Plenum Press, 1995, 251-68.

[100] Xue LA, Wu X, and Chen IW. Superplastic Alumina Ceramics with Grain Growth Inhibitors, *J Am Ceram Soc*, **74**, 1991, 842-45.

[101] French JD, Harmer MP, Chan HM, and Miller GA. Coarsening-Resistant Dual-Phase Interpenetrating Microstructures, *J Am Ceram Soc*, **73**, 1990, 2508-10.

[102] Lange FF, and Hirlinger MM. Grain-Growth in Two-Phase Ceramics: Al_2O_3 Inclusions in ZrO_2, *J Am Ceram Soc*, **70**, 1987, 827-30.

[103] Lange FF, Yamaguchi T, Davis BI, and Morgan PED. Effect of ZrO_2 Inclusions on the Sinterability of Al_2O_3, *J Am Ceram Soc*, **71**, 1988, 446-48.

[104] Cai PZ, Green DJ, and Messing GL. Constrained Densification of Alumina/Zirconia Hybrid Laminates, I: Experimental Observations of Processing Defects, *J Am Ceram Soc*, **80**, 1997, 1929-39.

[105] Exner HE. Analysis of Grain- and Particle-Size Distributions in Metallic Materials, *Inter Metall Rev*, **17**, 1972, 25-42.

[106] French JD, Zhao JH, Harmer MP, Chan HM, and Miller GA. Creep of Duplex Microstructures, *J Am Ceram Soc*, **77**, 1994, 2857-65.

[107] Cannon RM, Rhodes WH, and Heuer AH. Plastic Deformation of Fine-Grained Alumina (Al_2O_3): I, Interface-Controlled Diffusional Creep, *J. Am Ceram Soc*, **63**, 1980, 46-53.

[108] Wakai F, and Nagono T. The Role of Interface-Controlled Diffusion Creep on Superplasticity of Yttria-Stabilized Tetragonal ZrO_2 Polycrystals, *J Mater Sci Lett*, **7**, 1988, 607-09.

[109] Sudhir B, and Chokshi AH. Compression Creep Characteristics of 8-mol%-Yttria-Stabilized Cubic-Zirconia, *J Am Ceram Soc*, **84**, 2001, 2625-32.

[110] Oishi Y, Ando K, and Sakka Y. Lattice and Grain-Boundary Diffusion Coefficient of Cations in Stabilized Zirconias, in *Advance in Ceramics*, Westerville, Ohio, 1983, 208-19.

[111] Chien FR, and Heuer AH. Lattice Diffusion Kinetics in Y_2O_3-Stabilized Cubic ZrO_2 Single Crystals: A Dislocation Loop Annealing Study, *Philos Mag*, **A73**, 1996, 681-97.

[112] Lakki A, Herzog R, Weller M, Schubert H, Reetz C, Gorke O, Kilo M, and Borchardt G. Mechanical Loss, Creep, Diffusion and Ionic Conductivity of ZrO_2-8 mol% Y_2O_3 Polycrystals, *J Euro Ceram Soc*, **20**, 2000, 285-96.

[113] Xue LA, and Chen IW. Deformation and Grain Growth of Low-Temperature-Sintered High-Purity Alumina, *J Am Ceram Soc*, **73**, 1990, 3518-21.

[114] Wakai F. A Review of Superplasticity in ZrO_2-Toughed Ceramics, *Br Ceram Trans J*, **88**, 1989, 205-08.

[115] Wakai F, Nagano T, and Iga T. Hardening in Creep of Alumina by Zirconium Segregation at the Grain Boundary, *J Am Ceram Soc*, **80**, 1997, 2361-66.

[116] Yoshida H, Okada K, Ikuhara Y, and Sakuma T. Improvement of High-Temperature Creep Resistance in Fine-Grained Al_2O_3 by Zr^{4+} Segregation in Grain Boundaries, *Philos Mag Lett*, **76**, 1997, 9-14.

[117] Gutierrez-Mora F, Dominguez-Rodriguez A, Jiménez-Melendo M, Chaim R, Ravi GB, and Routbort JL. Superplasticity and Joining of Zirconia-Based Ceramics, in *Superplasticity-Current Status and Future Potential*, ed. Berbon PB, Berbon MZ, Sakuma T, and Langdon TG. Materials Research Society Symposium Proceeding, Vol. 601, 2000, 99-104.

[118] Marshall DB, Ratto JJ, and Lange FF. Enhanced Fracture-Toughness in Layered Microcomposites of Ce-ZrO_2 and Al_2O_3, *J Am Ceram Soc*, **74**, 1991, 2979-87.

[119] Marshall DB. Design of High-Toughness Laminar Zirconia Composites, *Am Ceram Soc Bull*, **71**, 1992, 969-73.

[120] Padture NP, Pender DC, Wuttiphan S, and Lawn BR. In-Situ Processing of Silicon Carbide Layer Structures, *J Am Ceram Soc*, **78**, 1995, 3160-62.

[121] Kuo DH, and Kriven WM. A Strong and Damage-Tolerant Oxide Laminate, *J Am Ceram Soc*, **80**, 1997, 2421-24.

[122] Moya JS. Layered Ceramics, *Adv Mater*, **7**, 1995, 185-89.

[123] Chan HM. Layered Ceramics: Processing and Mechanical Behavior, *Annu Rev Mater Sci*, **27**, 1997, 249-82.

[124] Becher PF, and Warwick WH. Fracture Strength Fracture-Resistance Response and Damage Resistance of Sintered Al_2O_3-ZrO_2 (12 mol% CeO_2) Composites, *J Am Ceram Soc*, **77**, 1994, 2689-92.

[125] Wang JG, Hsiung LM, and Nieh TG. Formation of Deformation Twins in a Crept Lamellar TiAl Alloy, *Scripta Mater*, **39**, 1998, 957-62.

[126] Snyder BC, Wadsworth J, and Sherby OD. Superplastic Behavior in Ferrous Laminated Composites, *Acta Metall*, **32**, 1984, 919-32.

[127] Jiménez-Melendo M, Clauss C, Dominguez-Rodriguez A, Sanchez Herencia AJ, and Moya JS. Microstructure and High-Temperature Mechanical Behavior of Alumina/Alumina-Yttria-Stabilized Tetragonal Zirconia Multilayer Composites, *J Am Ceram Soc*, **80**, 1997, 2126-30.

[128] Jiménez-Melendo M, Clauss C, Dominguez-Rodriguez A, De Portu G, Roncari E, and Pinasco P. High Temperature Plastic Deformation of Multilayered YTZP/ZTA Composites Obtained by Tape Casting, *Acta Mater*, **46**, 1998, 3995-4004.

[129] Jiménez-Melendo M, Gutierrez-Mora F, and Dominguez-Rodriguez A. Effect of Layer Interfaces on the High-Temperature Mechanical Properties of Alumina/Zirconia Laminate Composites, *Acta Mater*, **48**, 2000, 4715-20.

[130] Wang J, Kovar D, and Taleff EM. High-Temperature Deformation of Al_2O_3/Y-TZP Paticulate Composites, *Acta Mater*, **51**, 2003, 3571-83.

[131] Taleff EM, Ketcham RA, Reyes R, and Carlso WD. Nondestructive Evaluation of Cavitation in an Al-Mg Material Deformed under Creep Conditions, *J Mater Res*, **15**, 2000, 76-84.

[132] Russ JC. Practical Stereology, Plenum Press, New York, 1986.

Vita

Jue Wang was born in Hangzhou, China on April 30, 1976, the daughter of Yinkui Wang and Sendi Guo. After completing her study at No. 4 High School, Hangzhou, China, in 1994, she entered Zhejiang University, Hangzhou, China. She received the degree of Bachelor of Science from Zhejiang University in June 1998. She received the Master's Degree in Engineering from Zhejiang University in June 2000. In September 2000, she entered the Graduate School of the University of Texas at Austin.

Permanent address: 1632 W 6th St Apt J, Austin, TX 78703

This dissertation was typed by Jue Wang.